Sebastian Bär

Crystalline, Rare-Earth-doped Sesquioxide PLD-Films on -Alumina

Preparation and Characterization

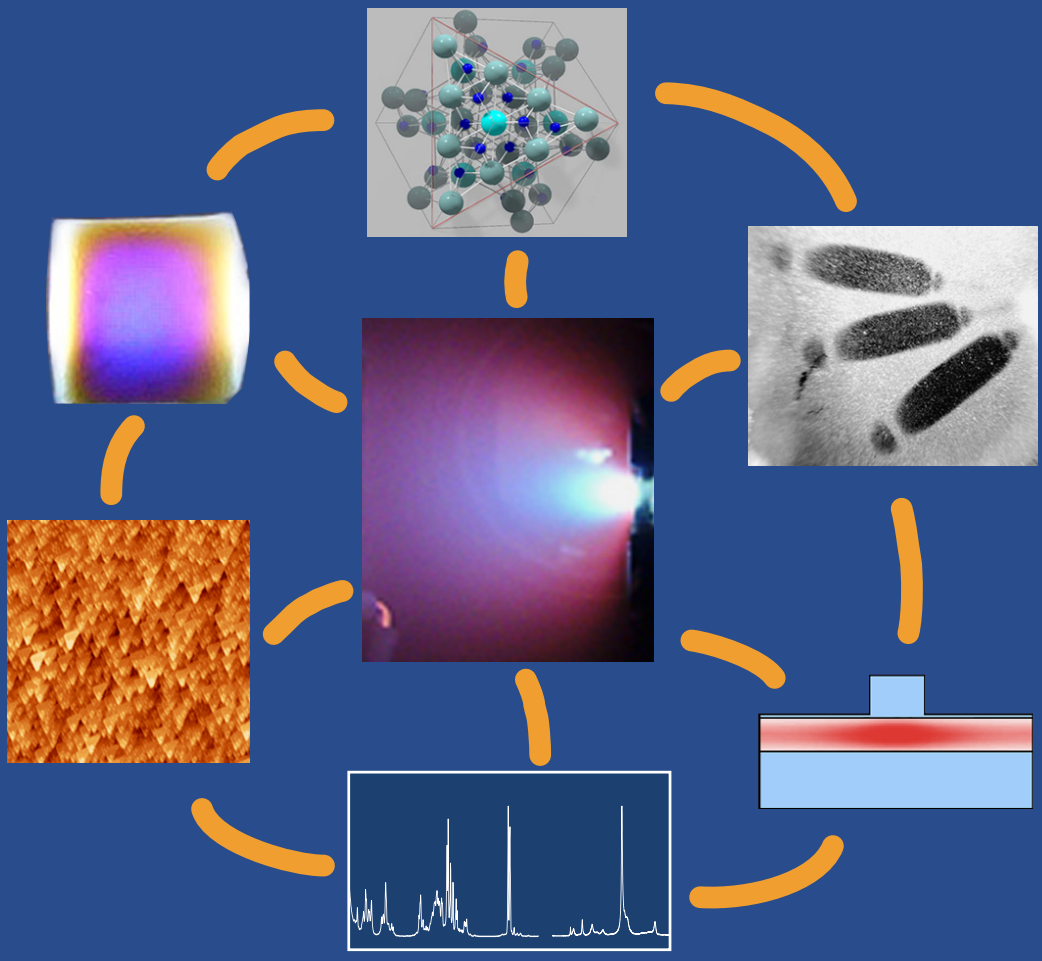

Crystalline Rare-Earth-doped Sesquioxide PLD-Films on α-Alumina

Preparation and characterization

Dissertation

zur Erlangung des Doktorgrades
des Fachbereichs Physik
der Universität Hamburg

vorgelegt von

Sebastian Bär

aus Berlin

Hamburg
2004

Bibliografische Information Der Deutschen Bibliothek
Die Deutsche Bibliothek verzeichnet diese Publikation in der Deutschen Nationalbibliografie; detaillierte bibliografische Daten sind im Internet über http://dnb.ddb.de abrufbar.
1. Aufl. - Göttingen : Cuvillier, 2004
Zugl.: Hamburg, Univ., Diss., 2004
ISBN 3-86537-149-3

Gutachter der Dissertation:	Prof. Dr. G. Huber
	Prof. Dr. D. Heitmann
Gutachter der Disputation:	Prof. Dr. G. Huber
	Prof. Dr. G. Zimmerer
Datum der Disputation:	11.05.2004
Dekan des Fachbereichs Physik Vorsitzender des Promotionsausschusses:	Prof. Dr. G. Huber Prof. Dr. R. Wiesendanger

Nonnenstieg 8, 37075 Göttingen
Telefon: 0551-54724-0
Telefax: 0551-54724-21
www.cuvillier.de

1. Auflage, 2004
Gedruckt auf säurefreiem Papier

ISBN 3-86537-149-3

Abstract

Sebastian Bär, *Crystalline rare-earth-doped sesquioxide PLD-films on α-alumina*

The development of integrated optical devices demands the fabrication of high-quality optically active thin films. This work focuses on thin sesquioxide films, which are promising because the sesquioxides are well-known hosts for rare-earth-ions, leading to luminescent materials and solid-state lasers with superior mechanical and thermal properties (e. g. low phonon energies, large thermal conductivity).

Optical quality crystalline thin films of rare-earth-doped sesquioxides (yttria, lutetia, and scandia) have been grown by the pulsed laser deposition (PLD) technique on single-crystal (0001) α-alumina substrates. Alumina substrates offer a lattice constant that matches that of cubic Y_2O_3 in the $\langle 111 \rangle$ direction very well. Using Lu_2O_3 and Sc_2O_3, the mismatch of 4.8% related to Y_2O_3 on alumina substrates can be considerably reduced leading to the production of films with less dislocations.

The crystal structure of these films (thicknesses from 1 nm to 500 nm) was determined by X-ray diffraction (XRD) and surface X-ray diffraction (SXRD) analysis. These measurements show that the films were textured along the $\langle 111 \rangle$ direction, however with a small polycrystalline component, which is negligible in thick films. Using Rutherford backscattering analysis (RBS), the correct stoichiometric composition of the films could be proved. At optimum growth conditions, epitaxial growth of Y_2O_3 along the $\langle 111 \rangle$ direction on the [0001] α-Al_2O_3 was experimentally verified by the observation of channelling in the RBS experiments.

The surface morphology of the thin films has been studied using atomic force microscopy (AFM). While amorphous films have no defined surface structure, crystalline films show a triangular surface morphology, which is attributed to the $\langle 111 \rangle$ growth direction. The same structure is observed along the $\{111\}$ cleavage of an yttria bulk crystal. Thin films with a mean thickness of 5 nm have no completely covered surface, but show island growth, where the shape of the single crystallites, having angles of 60° or 120°, indicates the $\langle 111 \rangle$ growth direction during the early stages of film growth.

To study the optical properties of the rare-earth-doped films, spectroscopic measurements in the (vacuum-) ultraviolet and visible spectral-range have been carried out. The emission and excitation spectra of the Eu^{3+}-doped films look similar to those of the corresponding crystalline bulk material down to a film thickness of 100 nm, i. e. the symmetry around the Eu^{3+}-ions is preserved, whereas films with a thickness $\leq$ 20 nm show a completely different emission behavior. This change can be explained by subplantation effects of high-energy plasma species hitting the substrate surface, leading to mixed compounds like $Y_3Al_5O_{12}$. In addition, surface effects due to a large surface-to-volume ratio of the observed islands have a significant impact on the 'film' properties.

For possible applications in integrated optics, waveguide experiments have been performed in the system Y_2O_3–Al_2O_3. Single-mode guiding of the fundamental mode was demonstrated in the 1 µm thick yttria layer.

Kurzfassung

Sebastian Bär, *Kristalline, Selten-Erd-dotierte Sesquioxid-PLD-Schichten auf α-Al_2O_3*

Die Entwicklung neuer Bauteile für die integrierte Optik erfordert in zunehmendem Maße die Herstellung von dünnen, optisch aktiven Schichten. Aufgrund ihrer mechanischen und thermischen Eigenschaften sind die Sesquioxide interessant für ein solches Aufgabengebiet, zumal sie mit Seltenen Erden (SE) dotiert in Leuchtstoffen oder Festkörperlasern bereits im Einsatz sind.

Mit der Technik der Pulsed Laser Deposition (PLD) konnten kristalline Schichten aus Selten-Erd-dotierten Sesquioxiden (Y_2O_3, Lu_2O_3 und Sc_2O_3) auf (0001)-Korundsubstraten in optischer Qualität hergestellt werden.

Die Kristallstruktur dieser Schichten mit Dicken zwischen 1 nm und 500 nm wurde mittels Röntgenbeugung (XRD) und Oberflächenröntgenbeugung (SXRD) bestimmt und ein bevorzugtes Wachstum in $\langle 111 \rangle$-Richtung festgestellt. Neben der korrekten Stöchiometrie lieferte die RBS-Analyse auch Hinweise auf epitaktisches Wachstum der Schichten (Channeling).

Die Oberflächenbeschaffenheit der Schichten wurde mit der Rasterkraftmikroskopie untersucht. Während bei amorphen Schichten keine definierte Struktur vorliegt, zeigen die Aufnahmen von kristallinen Schichten eine dreieckige Oberflächenstruktur, die der $\langle 111 \rangle$-Richtung zugeschrieben wird. Eine ähnliche Struktur wurde entlang einer $\{111\}$-Spaltfläche in einem Y_2O_3-Volumenkristall beobachtet. Bei sehr geringen Schichtdicken (≤ 5 nm) ist die Substratoberfläche dagegen nicht komplett von einem Y_2O_3-Film bedeckt. Stattdessen wurde kristallines Inselwachstum beobachtet, wobei die Form der einzelnen Kristallite scharfkantige Strukturen mit Winkeln von 60° oder 120° aufweist, was ebenfalls ein Hinweis auf die $\langle 111 \rangle$-Wachstumsrichtung in dieser frühen Phase der Filmbildung ist.

Die Emissions- und die Anregungsspektren der Eu-dotierten Schichten mit Dicken $\geq$ 100 nm entsprechen denen eines Volumenkristalls. Schichten mit einer Dicke $\leq$ 20 nm zeigen dagegen ein stark verändertes Emissionsverhalten. Diese Veränderungen ergeben sich durch die Subplantation von hochenergetischen Teilchen aus dem Plasma, so daß es zu einem Mischsystem $Al_2O_3 - Y_2O_3$ kommt, in dem sich dann $Y_3Al_5O_{12}$ bildet. Desweiteren hat das an der Oberfläche beobachtete Inselwachstum auch einen erheblichen Einfluß auf die optischen Eigenschaften. Denn durch ein vegrößertes Verhältnis von Oberfläche zu Volumen treten oberflächenbedingte Effekte deutlich stärker hervor.

Um möglichen Anwendungen im Bereich der integrierten Optik gerecht zu werden, wurden erste Wellenleiter-Experimente am Schichtsystem $Y_2O_3 - Al_2O_3$ durchgeführt. Dabei konnte in einer ein Mikrometer dicken Yttriumoxidschicht Single-Mode-Führung bei einer Wellenlänge von 632 nm bzw. 488 nm erzielt werden.

Contents

Abstract i
Kurzfassung ii

List of Symbols and Abbreviations **v**

1 Introduction **1**
1.1 Motivation 1
1.2 Structure of this Thesis 7

2 Materials **9**
2.1 Sesquioxides 9
2.2 Corundum 12
2.3 Rare-Earth Dopants 14
2.3.1 Energy Levels of Free Ions 15
2.3.2 Crystal Field Splitting 16
2.3.3 Selection Rules 17
2.3.4 Interconfigurational 4f-5d and Charge Transfer Transitions 18
2.3.5 Influence of the Phonons 20
2.3.6 Europium 22

3 Pulsed Laser Deposition **25**
3.1 Laser–Target Interactions 26
3.2 The Plasma Plume 31
3.3 Growth Mechanisms 36

4 Thin Film Preparation by Pulsed Laser Deposition **41**

5 Analytical Techniques and Thin Film Characterization **49**
5.1 X-Ray Diffraction 49
5.1.1 Bragg-Brentano Setup 52
5.1.2 500 nm Y_2O_3 films 52
5.1.3 Thin Y_2O_3 films 56
5.1.4 Surface X-ray Diffraction 58
5.2 Rutherford Backscattering 65
5.2.1 Channeling 66
5.2.2 Experimental 66
5.3 Atomic Force Microscopy 69

5.4 Optical Spectroscopy 75
5.4.1 500 nm Eu^{3+}:Y_2O_3 films 76
5.4.2 Thin Eu^{3+}:Y_2O_3 films 78
5.4.3 Thin Eu^{3+}:Lu_2O_3 Films 88
5.4.4 Thin Er^{3+}:Sc_2O_3 Films 90

6 Waveguides **93**
6.1 Theory of Waveguides 93
6.1.1 Three-Layer Asymmetric Slab Waveguide 95
6.2 Yttria Waveguide 96
6.2.1 Waveguide Preparation 96
6.2.2 Waveguide Experiments 97
6.2.3 Ridge Waveguide Simulations 99
6.3 Photonic Crystals 101

7 Conclusions **105**
7.1 Summary of Results 105
7.2 Résumé 108
7.3 Outlook and Future Work 108

A Energy Levels of Eu^{3+} in Y_2O_3 **111**

B List of Fabricated Films **113**

C X-ray Diffraction Peaks of Y_2O_3 films **115**

Bibliography **116**

List of Publications **131**

Acknowledgement **133**

Index **135**

List of Symbols and Abbreviations

Constants

ε_0	vacuum permittivity
a_B	Bohr radius
c_0	speed of light in vacuum
e	elementary charge
h	Planck constant
$\hbar$	$= h/2\pi$
k	Boltzmann constant
m_e	electron mass

Variables

$\alpha(\lambda)$	absorption coefficient
β	propagation constant
γ	adiabatic exponent
γ_f	surface energy of the growing film
γ_i	interface energy film–substrate
γ_m	multi-photon absorption coefficient
γ_s	surface energy of the substrate
ε_av	avalanche coefficient
θ	diffraction angle
θ_crit	critical angle of total reflection
λ	wavelength
ν	frequency
ϱ	charge density
τ	pulse duration
φ	wetting angle of a nucleus on the substrate

Φ	laser fluence
Φ_{thr}	threshold laser fluence
Ψ_0	wavefunction of a free ion in the central field approximation
χ_{opt}	optical electronegativity
ω	$= 2\pi\nu$ angular frequency
a	lattice constant
$\mathbf{a}$	primitive lattice vector
$\mathbf{B}$	magnetic field
c	speed of light in a medium
C_{v}	specific heat
d_{hkl}	inter planar spacing
D_{th}	thermal diffusivity
$\mathbf{D}$	electric displacement
E_0	energy eigenvalue of an ionic state
$\mathbf{E}$	electric field
$\mathbf{E}(\mathbf{r})$	electrostatic field of the ligands
g_0	statistical weight of a neutral atom
g_i	statistical weight of an electron–ion pair
$\mathbf{G}$	reciprocal lattice vector
$\mathcal{H}$	Hamiltonian for a free ion
$\mathcal{H}_0$	Hamiltonian for a free ion in the central field approximation
$\mathcal{H}_{ee}$	pertubation term for $\mathcal{H}_0$: non radial.symmetric part of the electron-electron interaction
$\mathcal{H}_{\mathrm{SO}}$	pertubation term for $\mathcal{H}_0$: spin-orbit coupling
$\mathcal{H}_{\mathrm{Stark}}$	pertubation term for $\mathcal{H}_0$: interaction of the 4f electrons of a lanthanide ion with the electrostatic field of the ligands
$\mathbf{H}$	magnetic flux density
ΔH_{v}	vaporization energy
I_{thr}	threshold power intensity
$\mathbf{j}$	current density
$\mathbf{j}_i$	angular momentum vector of the i^{th} electron
$\mathbf{J}$	total angular momentum quantum number
$\mathbf{k}$	$= 2\pi/\lambda$ wavevector
K	thermal conductivity
l_i	orbital angular momentum quantum number of the i^{th} electron

$\mathbf{l}_i$	orbital angular momentum vector of the i^{th} electron
L_{th}	thermal diffusion length
m_l	magnetic quantum number of an electron
m_s	spin quantum number
M	Mach number
n_0	density of neutral atoms
n_e	density of electrons
n_i	density of ions
n_i	principal quantum number of the i^{th} electron
$n_{\text{s/f/c}}$	refractive index of the substrate, film, and superstrate
n_{eff}	effective refractive index
N	number of electrons in an ion
N_e	electron density in the conduction band
p	mode number
$p(\text{O}_2)$	oxygen partial pressure
r_i	position of the i^{th} electron relative to the nucleus
r_{ij}	position of the electrons i and j relative to each other
$R(\lambda)$	reflectivity
R_{RMS}	surface roughness (root-mean-square)
$\mathbf{s}_i$	spin vector of the i^{th} electron
$\mathbf{S}$	total spin quantum number
T_0	initial temperature
$V(\mathbf{r})$	effective spherically potential in the central field approximation
w_0	beam radius
W_i	ionization potential
Z	atomic number

Abbreviations

AFM	atomic force microscope
AI	avalanche ionization
CTS	charge transfer state
EBV	electron beam evaporation
ED	electric dipole

ES	excitonic state
FWHM	full width at half maximum
LuAG	lutetium aluminum garnet ($Lu_3Al_5O_{12}$)
MD	magnetic dipole
MPA	multi-photon absorption
NA	numerical aperture
PLD	pulsed laser deposition
QCA	quantum confined atom
RBS	Rutherford backscattering
RE	rare earth
RHEED	reflection high energy electron diffraction
RMS	root-mean-square
SNOM	scanning near-field microscope
SXRD	surface X-ray diffraction
TE	transverse electric polarization
TEM	transmission electron microscope
TM	transverse magnetic polarization
XRD	X-ray diffraction
VUV	vacuum ultraviolet
YAG	yttrium aluminum garnet ($Y_3Al_5O_{12}$)

1 Introduction

1.1 Motivation

In recent years the data transfer created by computer-based business processes and internet applications has been growing exponentially. This development requires an increasing transmission capacity at lower cost, which can only be met by increased use of optical fibre and associated advanced photonic technologies. The operation of these new devices must be described in terms of optics as well as of electronics, giving birth to a mixed discipline called *(integrated) photonics*. The basic idea behind integrated photonics is the use of photons instead of electrons, creating integrated optical circuits similar to those in conventional electronics, i. e. the fabrication and integration of several photonic components on a common planar substrate.

The replacement of electronic by photonic devices is forced by fundamental physical reasons that limit the information transmission rate using purely electronic devices: as the frequency of an electrical signal propagating through a conductor increases, the impedance of the conductor also increases, thus the propagation characteristics of the electrical interconnection become less favorable. In contrast, optical signals propagate through nonconducting dielectric media, operating in the wavelength range where these materials are highly transparent. In general, this transparent window falls in the visible and near-infrared range of the electromagnetic spectrum, which corresponds to light frequencies around 300 THz, 10^6 times the frequency used in electrical transmission, which allows a very large bandwidth for transporting a huge amount of information.

The optical elements present in integrated photonic devices should include basic components for generating, focusing, splitting, junction, coupling, isolating, polarization controlling, switching, modulating, filtering and detecting of light. The key element of these devices are optical waveguides, that provide not only guiding, but also coupling, switching, splitting, multiplexing, and demultiplexing of optical signals.

Although nowadays a long list of integrated photonic devices has been proposed, modelled, and fabricated, and their number is quickly increasing, the basic components remain almost unchanged. All the optical components in integrated photonics are constructed from three building blocks. These are the straight waveguide, the bend waveguide and the power splitter (Y-branch). Using these building blocks, several basic components have been developed to perform basic optical functions. A good overview on the specific elements is given in [Lif03].

The basic technology for these waveguides is the fabrication of high quality thin films. The methods most widely used for the production of such thin films are diffusion techniques (e. g. titanium indiffusion in lithium niobate) and deposition techniques (such as chemical vapor deposition used for silica). The integration of multiple functions within a planar optical circuit requires structures with lateral dimensions of a few microns, which can be achieved by photolithographic processes [Hai01]. For the fabrication of functional devices different materials are used. Apart from semiconductors such as indium phosphide (InP), gallium arsenide (GaAs) – an example is depicted in figure 1.1 or even silicon (Si), also dielectrics such as polymers, glasses, silica on silicon (SiO_2/Si), or lithium niobate ($LiNbO_3$) are suitable for the use in integrated photonics.

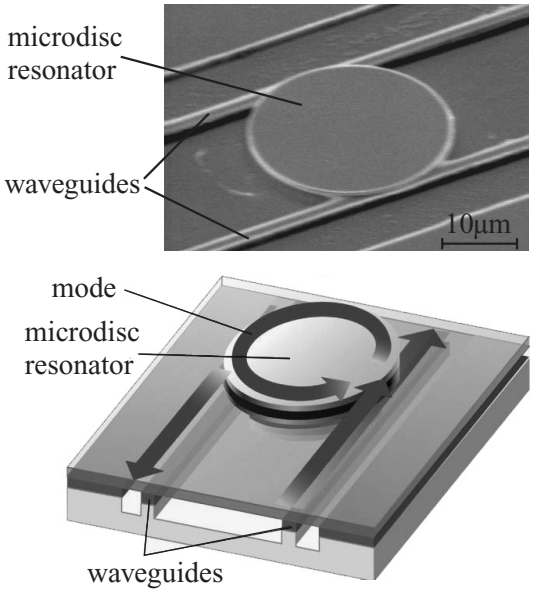

Figure 1.1: *InGasP ring resonator* [Tis99].

Photonic Crystals

Aside from this 'classical' way of realizing the necessary components for integrated optics, a new class of materials, termed *photonic crystals*, with optical properties that can be designed individually has been developed. In a photonic crystal, the periodic arrangement of refractive index variation controls how photons are able to move through the crystal. Similar to the periodic arrangement of ions in a lattice, which gives rise to the energy band structure e. g. in semiconductors, the refractive index contrast results in a photonic band structure characterized by a photonic band gap. Breaking the periodicity introduces new energy levels within the photonic band gap. This defect mode or microcavity formed by breaking the periodicity of the crystal amplifies only those wavelengths of light that are able to pass freely through the crystal. Photonic crystal microcavities are more efficient than conventional semiconductor diode lasers since there are few directions in the which the photons can escape. Two examples of photonic crystal structures are shown in below.

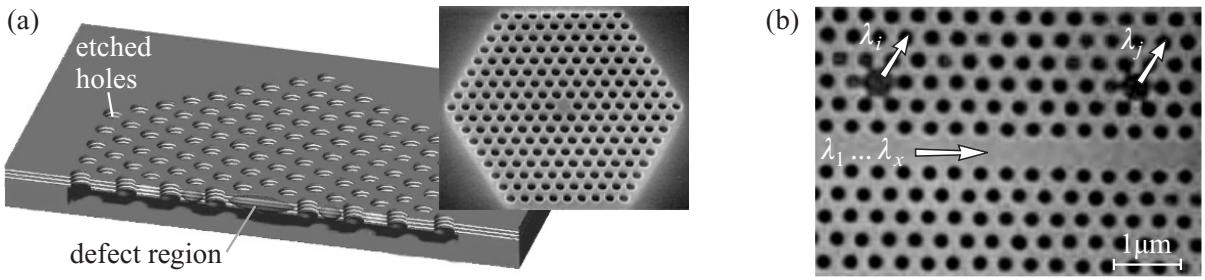

Figure 1.2: *Photonic crystal structures: (a) microcavity formed by a 'point defect'* [Vah03]*, (b) Add-drop filter* [Nod00]

Dielectric Oxides

The materials used for integrated optics are mainly compounds of semiconductors as they are the most promising materials for monolithic integration of the components.This means that the highest level of integration (whether serial or parallel) can be achieved, where all the optical elements including light sources, light control, electronics, and detectors are incorporated in a single substrate. In certain cases, the hybrid integration technology might be favorable. Hybrid technology means that different elements are built on different substrates and then directly attached to each other or interconnected by optical fibres.

Compared with the highly developed standard fabricating and structuring techniques for semiconductor devices, the techniques for structuring crystalline oxide dielectrics are not well known, even if the processes are basically the same. Since this class of materials offers a range of advantageous properties, however, the aim of this thesis is the preparation and characterization of thin sesquioxide films, i. e. yttria Y_2O_3, lutetia Lu_2O_3, and scandia Sc_2O_3.

An advantage of the dielectric oxides is their wide transparency range from the ultraviolet to the mid-infrared part of the electromagnetic spectrum. Due to the possibility of doping the oxides with rare-earth-ions, the optical properties can be influenced selectively. Compared with semiconductors, the refractive index of these oxides is moderate resulting in considerably reduced fresnel reflections at the endfaces designed for coupling light in and out of the device. This is an important point since these reflections determine the efficiency of the system. For example, at normal incidence of near-infrared light, the index difference between semiconductors and air is of the order of $\Delta n \approx 2.5$ resulting in a reflectivity of $\approx 30\%$. Under the same conditions, the reflectivity of dielectric oxides is less than 10% because the index difference is smaller ($\Delta n < 1$).

The growing interest in the fabrication and characterization of Y_2O_3 films over the last few years is related to the diverse range of potential applications that can be envisioned. Y_2O_3 is an important material for semiconductor applications as well as for optical applications such as phosphors or waveguide lasers because of its ability to be a host material for rare-earth atoms like europium or thulium [Pol97, Jon97, Hui00]. Especially in the semiconductor industry, the use of Y_2O_3 in metal–insulator–semiconductor (MIS) diodes, transistor gates, metal–oxide–semiconductor (MOS) capacitors, and dynamic random access memory (DRAM) gate dielectrics is favorable due to its large bandgap (5.8 eV) and large dielectric constant (14-18) [Jon97, Ras92, Zha98].

Eu-doped Y_2O_3 is a well-known red phosphor [Jon97] and still used – as a powder – in electroluminescent displays (ELDs), fluorescent lamps, and cathodoluminescent (CL) displays. However, thin film phosphors have several advantages over powders, such as higher lateral resolution from smaller grains, better thermal stability, reduced outgassing, and better adhesion to the solid surface [Hir97]. Seeing these advantages, there is a significant interest in the development of Eu:Y_2O_3 thin film phosphors for the use in field emission display (FED) technology replacing the Eu:Y_2O_2S system which is used in the traditional cathode ray tube (CRT).

Resulting from its high melting point of 2410℃, Y_2O_3 is also widely used for high temper-

ature corrosion protection. In combination with the efficient transmission of infrared (IR) radiation, this robustness makes yttria films a very promising material for protective and antireflective coatings for IR detectors, e. g. HgTe and HgCdTe photovoltaic IR detectors.

Although Y_2O_3 has a lot of beneficial properties as shown above, lutetia and scandia offer additional positive properties for thin film production. The lattice constants of Lu_2O_3 and Sc_2O_3 are 10.39 Å and 9.86 Å, respectively, and thus, these values match better the lattice constant of sapphire, a common substrate for yttria, leading to the production of films with fewer dislocations. Additionally, both materials have a higher refractive index than Y_2O_3, which might be interesting for waveguide applications and for the fabrication of photonic crystals, where a high index contrast is advantageous.

Up to now, however, only little attention has been paid to Lu_2O_3 and Sc_2O_3. Scandia, for example, might be suitable for reducing surface states on AlGaN/GaN high electron mobility transistors (HEMT) and, in addition, exhibit promise as gate dielectrics in GaN [Luo02]. Since Lu_2O_3 has the largest bandgap among the rare-earth oxides, it is also considered for high-dielectric constant (high-k) gate insulator applications [Ohm02]. Additionally, Lu_2O_3 can be used as an efficient scintillator material because of its high absorption coefficient for ionizing radiation. Because of the high Z-number an incoming gamma or X-ray particle can be preferentially stopped at a single position. Therefore, higher resolution images in medical diagnosis can be envisioned [Zyc02].

Another application for rare-earth-doped sesquioxide films is the fabrication of planar waveguide structures. These include passive elements as well as active waveguides (amplifiers and lasers), because these materials are well known bulk hosts for laser ions (e. g. Nd:Y_2O_3, Yb:Y_2O_3) [For99, For00]. One of the first steps towards these devices is to be able to produce planar optical waveguides in very good quality. There is no question about the predominant role of optical fibres in long distance data transmission, but for active processes crystalline optical waveguides offer substantial advantages: The larger emission and absorption cross sections available in crystalline matrices become accessible, and the confinement of light inside the waveguide generates a larger intensity-length product. Since nonlinear processes, like upconversion or frequency conversion, depend strongly on the intensity, the realization of these processes is much easier to achieve in waveguides. Additionally, the guiding of the pump mode as well as the signal mode leads to an excellent overlap of the modes resulting in lower laser thresholds.

Thus, lasing can be achieved on transitions that possess an impractically high lasing threshold in bulk materials [Han93]. Apart from waveguides of Nd:YAG [Bon00], Nd:GGG [And98, Bar01], and Ti:Al_2O_3 [And98], also first yttria waveguides have been fabricated, for example Er:Y_2O_3 [Hoe92, Kor01, Lec02].

Why Pulsed Laser Deposition?

There are many technologies existing for the fabrication of optical thin films and apart from the pulsed laser deposition technique, a variety of other physical and chemical methods have been used in the past to synthesize dielectric Y_2O_3 films, e. g. chemical vapor

deposition (CVD) [Sha93, McK00], RF magnetron sputtering [Gur87], ion-assisted evaporation [Cho99], anodization [Gol68], electron-beam evaporation (EBV) [Fuk89], sol-gel techniques [Rao96, Lou01], and reactive synthesis [And94].

In recent years, however, pulsed laser deposition (PLD) has proven to be a very attractive and practical method not only for the growth of high-quality doped [Cho98, Gao99] and undoped [Zha98] Y_2O_3 films (pure or doped Y_2O_3 sintered targets were used) but also for a variety of other materials. There are many reasons why this method has become that attractive for the fabrication of thin films, namely the possibility

- to generate films that match the stoichiometry of the target due to an extremely high heating rate of the target (10^8 K/s) leading to congruent evaporation (whereas conventional thermal evaporation or sputtering can lead to non-stoichiometric deposits).
- to use small targets (in contrast to the large targets required for sputtering)
- to deposit in reactive gas environments (in contrast to conventional evaporation, where hot filaments and/or crucibles could be oxidized).
- to benefit from high energies of the plasma species (often 5 to $\geq$100 eV) that can have beneficial effects on the film properties, e.g. good film adhesion at low substrate temperatures
- to benefit from a high ionization degree of the plasma flux (up to 80%), positively influencing the film properties
- to accurately control of the film thickness by controlling the number of laser pulses

A more detailed description of the PLD process will be given in chapter 3. Apart from sintered targets of Y_2O_3, there have also been attempts to use a pure metal ablation target [Kor00]. In combination with alternate-target PLD, it is possible to have a precise control of dopant concentration levels and in-depth separation [Ser99].

For crystalline film growth, an appropriate substrate material is very important, because epitaxial film growth depends strongly on the lattice matching between film and substrate. Besides crystallinity, the desired application determines the substrate. In fact, thin films of yttria have been grown on various substrates, e. g. Si, SiO_2, MgO, Al_2O_3, $LaAlO_3$ and yttrium-stabilized zirconia (YSZ) [Cho98, Cho00, Dik03, Fuk89, Gao99, Gab02]. Generally, these films were highly textured along the $\langle 111 \rangle$ or $\langle 100 \rangle$ crystallographic axis.

Nanostructures

The capability of PLD to produce 'films' with thicknesses smaller than a monolayer makes this technique interesting for structures in the sub-nanometer range, which is like "playing LEGO at the atomic scale" [Bla04].

In addition to possible applications already mentioned it is then also interesting to investigate fundamental aspects of interface and surface physics. For these nanostructures, the definition of a 'bulk' material property loses its relevance because a large fraction of the device actually constitutes the interfaces between film and substrate or between films of different materials. Due to the large surface-to-volume ratio, the probability for localized surface defects, such as unsaturated bonds and dislocations, is increased, leading to a considerably modified luminescence behavior.

Changes in structure, composition, and bonding that occur only a few atoms away from the interface can now have significant impact on the overall properties of the device. Additionally, defects, such as dislocations and grain boundaries, play a more important role because they can also be responsible for the failing of devices.

Of particular interest are quantum confinement effects and enhanced luminescence efficiency, when the particle dimensions become comparable to Bohr radii of the atomic wave functions. Since the density of states for photons as well as the polarizability of the medium surrounding the radiative source is changed in nanostructures, the coupling of the lanthanide ion to the modes of the radiation field can be modified. Thus, it is possible to change the decay rates by controlling the particle size, resulting in an enhancement of the luminescent properties with respect to the bulk crystal.

It is also interesting to consider the effect of a dielectric boundary on a rare-earth-ion embedded in a particle with dimensions much smaller than the transition wavelength. Having different refractive indices, interference effects can be observed which are related to the direction of propagation and the polarization. Using two parallel boundaries, which are designed to reflect light of the emitted wavelength, the linewidth of this transition can be reduced and the decay rates can be considerably modified. In these *microcavities* laser action without a threshold can be achieved.

The final step in miniaturization is the preparation of a single active ion in a crystalline matrix (in comparison to the ensemble in a bulk material and the investigations of single ions in traps), known as *quantum confined atom* (QCA). Barnes et al. observed for the first time the fluorescence of single rare-earth-ions in metal oxide nanoparticles, i. e. single Eu^{3+}-ions in Y_2O_3 nanoparticles with a size ranging from 5 nm to 15 nm. The single ion luminescence was detected by observing the phenomenon of 'on–off blinking', a characteristic feature of almost all single quantum systems that show luminescence behavior [Bar00]. Since multiple bright states in the luminescence behavior have been identified by 'blinking' on a variable time scale, the possibility for nanoscale optical logic applications can be envisioned using isolated nanoparticles as individually addressable information storage units.

1.2 Structure of this Thesis

This introduction is followed by a description of the crystallographic and physical properties of the sesquioxides and α-alumina, which serves as substrate material. Additionally, the electronic transitions and optical properties of the rare-earth-ions are summarized in chapter 2. These lanthanide ions are incorporated in the thin films as luminescent probes.

Chapter 3 describes the fundamental physical mechanisms involved in the PLD process as well as some experimental aspects of thin film fabrication by PLD. After these general remarks, chapter 4 covers the production of different sesquioxide films by PLD in more detail. This includes the target and substrate preparation, a description of the PLD setup and the parameters used during the ablation process.

The experimental characterization of the fabricated thin films is then described in chapter 5. Although films of all three sesquioxides – yttria, lutetia and scandia – have been prepared, the main emphasis is put on the Y_2O_3 films.

The analytical tools for examining the structure of the films are X-ray diffraction and surface X-ray diffraction (crystallinity), Rutherford backscattering (quantitative elemental analysis), and atomic force microscopy (surface morphology). These techniques and the results of their application are described in sections 5.1 - 5.3, while the results of the determination of the optical properties of the rare-earth-doped sesquioxide films, studied by fluorescence and excitation measurements (including VUV excitation measurements), are discussed in section 5.4.

One aspect of this thesis was the development of waveguide structures based on a RE_2O_3–Al_2O_3 system. After a short introduction to waveguide theory, the preparation and characterization of a planar yttria waveguide is presented in chapter 6.

Finally, chapter 7 presents the conclusion drawn from the experimental results and gives an outlook on possible improvements.

2 Materials

This chapter gives an overview about the materials used for thin film production by pulsed laser deposition. In the first part, the sesquioxides yttria, lutetia and scandia are described and their key properties relevant to this work are presented. Additional data can be found in the theses of E. Mix, L. Fornasiero, and V. Peters [For99, Mix99, Pet01]. Section 2.2 deals with the properties of corundum, which was chosen as substrate material for the thin sesquioxide films. In the third part of this chapter (section 2.3), an overview of the lanthanides and their optical properties is given. This includes a theoretical treatment of the position of their energy levels, intraconfigurational *4f-4f*, interconfigurational *4f-5d*, and charge transfer transitions (sections 2.3.1 to 2.3.4). Additionally, the influence of the host material phonons on the luminescence behavior is explained by the single configurational coordinate model (section 2.3.5). Finally, the europium ion, which was used as a probe ion in the sesquioxide matrices, is introduced (section 2.3.6).

2.1 Sesquioxides

The structural and optical properties of rare-earth sesquioxides (Ln_2O_3) have been extensively studied for several years, because these oxides are known to be excellent laser host materials due to a high thermal conductivity, a low phonon energy, and a high damage threshold [Mor82]. The term sesquioxide refers to the ratio between the anions and cations (lat. sesqui = one and a half).

Depending on the cation radius, the temperature, and pressure, the sesquioxides can be found in several crystallographic structures [Rot60, Hoe66]. At room temperature, the sesquioxides of yttrium (Y_2O_3), lutetium (Lu_2O_3), and scandium (Sc_2O_3) crystallize in the cubic C-type bixbyite structure with body centered space group $Ia3\,(T_h^7)$ [Wyc86]. This structure is stable up to the melting point except for yttria, which changes to a hexagonal high-temperature phase slightly below the melting point. Due to the lanthanide contraction, the lattice constants of the sesquioxides decrease slightly from Dy_2O_3 to Lu_2O_3. A typical scaling, however, is 10 Å depending on the type of cation.

The unit cell contains 16 formula units (80 atoms), and the oxygen atoms are arranged at six of the eight corners of a distorted cube around each metal ion. Thus, the 32 sixfold oxygen coordinated trivalent cations are accomodated in two different symmetry sites: 24 sites with point group symmetry C_2 (non-centrosymmetric), in the following labelled RE1, and 8 sites with C_{3i} symmetry (centrosymmetric), labelled RE2. The two-fold axes

of the C_2 sites are oriented parallel to the $\langle 100 \rangle$ directions, the three-fold axes of the C_{3i} sites are parallel to $\langle 111 \rangle$ (see figure 2.1).

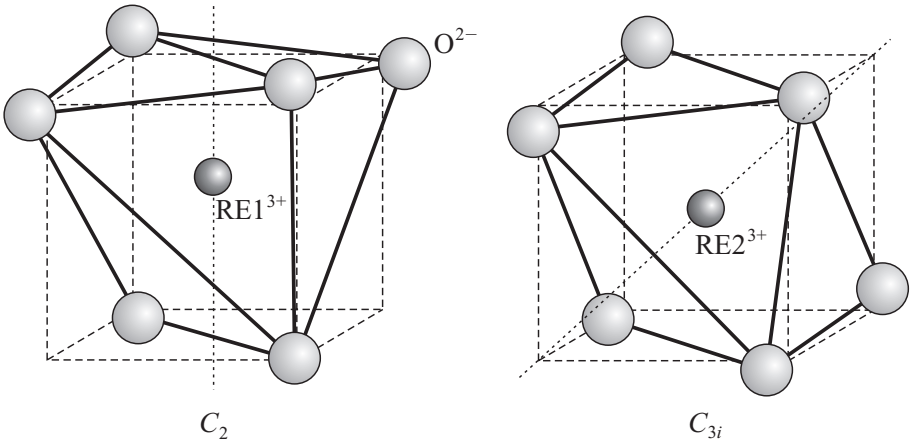

Figure 2.1: *The two different cation sites in the sesquioxide matrix.*

The bonding between the metal ions and the oxygen ions in sesquioxides is dominated by ionic bonding character with an admixing of covalent bonding. The bonding lengths between the metal ion and the oxygen ion for the two cation sites in the different sesquioxide matrices are given in table 2.1 (page 13). It should be noted that there are three different pairs of RE1–O bonds with varying distances, whereas all six RE2–O bonds have the same bonding length.

This geometric arrangement of the cation and its surrounding anions determines the electronic structure of the sesquioxides. However, up to now the interest in the electronic properties was mainly focused on crystalline yttria and only little attention has been paid to the sesquioxides lutetia and scandia.

Yttriumoxide

Y_2O_3 is an insulator with a bandgap energy of approximately 6.1 eV [Abr78]. Consequently, the absorption rises steeply at wavelengths $<$ 220 nm, and the fundamental absorption begins with a sharp maximum at 5.9 eV, which is considered as an excitonic state [Abr78, Tom86].

The binding energy of this exciton (0.1 eV) is considerablky low because the short-wavelength edge of the exciton band is superimposed by the interband absorption [Abr78].

Self-consistent band-structure calculations of Y_2O_3 by Xu et al. [Xu97] showed that the upper valence band is mainly formed by the *2p* orbitals of oxygen electrons and some admixing of the yttrium *4d* and *5p* orbitals, whereas the lower conduction band states are predominantly formed by Y *4d* and *5p* states.

From the observed values of the interelectronic repulsion parameters between the metal ion and the oxygen ligands, Jørgensen et al. predicted that a substantial degree of covalency is mixed with the predominant ionic bonding character between Y and O [Jør64]. This

prediction is based on the work of Ephraim and Bloch [Eph26], who found that the values of the interelectronic repulsion parameters separating the multiplet terms of $4f^q$ (*nephelauxetic effect*, see page 14) are smaller in more covalent compounds than in ionic compounds. The effective charges of Y1 and Y2 have been determined to +2.08 and +2.10, respectively, while the effective charge of the oxygen ions is −1.39 [Xu97].

Lutetiumoxide and Scandiumoxide

The sesquioxides Lu_2O_3 and Sc_2O_3 are isostructural to Y_2O_3, and all three crystals show a similar behavior in the spectra of their optical functions.

For Lu_2O_3, a steep decrease in the reflectivity related to interband transitions, is observed at an energy of 5.7 eV with a maximum at 6.1 eV, which is the bandgap energy. The sharp peak in the reflectivity spectrum at 5.8 eV indicates the excitonic state in Lu_2O_3 [Kir03, Kuz03].

The valence band energy levels in Y-based compounds are predominantly formed by oxygen *2p* orbitals. In Lu crystals, however, the top of the valence band is composed mainly by Lu *4f* orbitals [Moi97].

The band gap energy of Sc_2O_3 was determined by Abramov et al. to be 6.3 eV [Abr83]. Additionally, their calculations indicate for Sc_2O_3 a predominance of the ionic binding and a slightly greater contribution of covalency compared with Y_2O_3 ($q_{Sc} < q_Y$).

The most interesting difference between these three sesquioxides is the fact that in Y_2O_3 as well as in Lu_2O_3 an excitonic state can be observed, while for Sc_2O_3 no exciton was detected [Abr83].

As the described structural and electronic properties of the sesquioxides determine the crystal field, and thus, the energetic positions of the electronic states, they have important implications on the spectroscopic properties when activated with luminescent ions. In general, trivalent rare-earth-ions have been found to be distributed randomly in both sites in sesquioxide RE_2O_3 single crystals [Man63]. Due to these two different symmetry sites, the spectroscopic characteristics of $RE1^{3+}$ and $RE2^{3+}$ ions will differ from each other. While for centrosymmetric C_{3i} sites, the intraconfigurational *f-f* electric dipole transitions are forbidden and only magnetic dipole transitions can occur, the crystal field interaction with non-centrosymmetric C_2 sites introduces an opposite-parity part to the potential energy of the crystal levels, which makes electric dipole transitions also possible.

Compared to other oxide materials, i. e. $YAlO_3$ or $Y_3Al_5O_{12}$, the sesquioxides have a considerably smaller phonon energy, $E_{ph} = \hbar\omega_{eff}$. This property makes this class of materials interesting for optical upconversion processes, where non-radiative processes due to phonon relaxation should minimized.

2.2 Corundum

The sesquioxide films were grown on aluminum oxide substrates. Aluminum oxide crystallizes in many different structures. The form of aluminum oxide used as substrate in this thesis is the α form, α-Al_2O_3, termed corundum. Sometimes, the expression sapphire is used synonymously for this colorless crystal. In a more precise way, sapphire is Al_2O_3 doped with Fe^{2+} and Ti^{4+} resulting in blue colored crystals. Using Cr^{3+} as dopant, the crystal appears red and is commonly known as ruby.

α-Al_2O_3 crystallizes in a ditrigonal-scalenohedral structure with space group $R\bar{3}c$, in which the unit cell contains two Al_2O_3 units (see figure 2.2).

The oxygen ions form a hexagonal close-packed structure (hcp) where the Al^{3+} ions are located in the octahedrally coordinated interstices. Therefore, each aluminum ion is surrounded by six oxygen ligands having each three bonds lengths of 1.969 Å and 2.278 Å.

Underlying the hcp structure is a simple hexagonal Bravais lattice, given by stacking two-dimensional triangular nets directly on top each other. The direction of stacking is known as the c-axis of the crystal, whereas the lattice constants a and b generate the triangular lattice in the x-y-plane [Ash76].

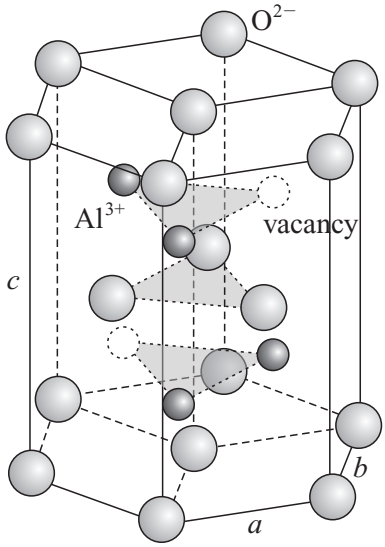

Figure 2.2: *Unit cell of α-alumina*

For the selection of a substrate for the growth of thin films with optical quality several requirements must be considered: good transmission in a wide range of wavelengths, a refractive index lower than that of the growing film, low cost, and a good thermal and lattice match with the chosen film. As all these conditions are widely fulfilled, sapphire is an attractive substrate candidate for the growth of Y_2O_3 films. The considerable small lattice mismatch, required for growing epitaxial films, compared to the crystal structure of yttria is the main reason for choosing alumina substrates. For $\langle 111 \rangle$ grown Y_2O_3 on (0001) α-Al_2O_3 this mismatch is 4.8%. The influence of lattice mismatch on film growth will be discussed in more detail in the context of thin film growth in section 3.3. Another advantage of an alumina substrate is the thermal conductivity which is of the same order as that of the sesquioxides.

The difference in the refractive indices between the sesquioxides and aluminumoxide is large enough to allow effective waveguiding in a sesquioxide layer. Additionally, the refractive indices of both materials are small enough to avoid significant losses due to fresnel reflections when coupling light in and out of the waveguide. The waveguiding mechanism in a system of $RE_2O_3 - Al_2O_3$ is discussed in chapter 6.

Alumina is also an insulator having a bandgap energy of 9.5 eV (130 nm), which is about 3.5 eV higher than that of yttria. A good overview of the electronic structure of aluminum oxide is given in [Bat82] and [Xu91].

Materials parameter

The most important parameters and properties of the substrate and the film materials are summarized in the table below.

	α-Al_2O_3	Y_2O_3	Lu_2O_3	Sc_2O_3
Crystal structure	hexagonal	cubic	cubic	cubic
Lattice constants (Å)	$a = 4.759$ $c = 12.989$	$a = 10.603$	$a = 10.391$	$a = 9.844$
Bond length RE1–O (Å)		2.331 2.274 2.243	2.183 2.239 2.282	2.163 2.093 2.079
Bond length RE2–O (Å)		2.284	2.247	2.122
Density ($\frac{\mathrm{g}}{\mathrm{cm}^3}$)	3.99	5.03	9.42	3.847
Density of cations ($10^{22}\,\mathrm{cm}^{-3}$)	4.70	2.69	2.85	3.35
Melting temperature (K)	2319	2703	≈ 2723	≈ 2703
Heat of melting ($\mathrm{J/cm}^3$)	4400	2220		
Evaporation temperature (K)	3253	4603	4258	
Heat of evaporation ($\mathrm{J/cm}^3$)	18 912	43 499		
Thermal Conductivity κ ($\frac{\mathrm{W}}{\mathrm{m\,K}}$) @ 300 K	0.46	> 12.8	> 12.2	> 15.5
Thermal Expansion α ($10^{-6}\,\mathrm{K}^{-1}$)	5.3 ($\parallel c$) 4.5 ($\perp c$)	8.6	7.9	9.6
Hardness (Mohs)	9	6.8	≈ 7	< 6.8
Young's Modulus E (GPa)	400	180	180	230
Poisson ratio	0.22	0.29	0.29	
Phonon energy $\hbar\omega_{\mathrm{eff}}$ (cm^{-1})	< 870	406	< 430	420
Transparency range (µm)	0.14 . . . 6.5	0.22 . . . 8	0.22 . . . ?	0.22 . . . 8
Refractive index n @ 1 µm	$n_{\mathrm{o}} = 1.7545$ $n_{\mathrm{e}} = 1.7460$	1.89	1.911	1.967
$\frac{\mathrm{d}n}{\mathrm{d}T}$ ($10^{-6}\,\mathrm{K}^{-1}$) @ 589 nm	13.6 (n_{o}) 14.7 (n_{e})	1.0		
Dielectric Constant	11.5 ($\parallel c$)	11 - 13	≈ 12	14

Table 2.1: *Material properties of α-Al_2O_3 and the sesquioxides Y_2O_3, Lu_2O_3, and Sc_2O_3* [Bár57, Ber74, Con69, For99, Mix99, Sam82, Web82, Zyc02].

2.3 Rare-Earth Dopants

In order to study the properties of thin films the lanthanide ions can be used as luminescent probes because their emission characteristics are sensitive to the crystallographic environment. Therefore, electronic transitions and characteristic optical properties of rare earth ions, which are required to interpret the optical data of the present systems, are summarized in this section. Of course, it is essential that the probe perturbs the investigated sample as little as possible when it is introduced by substitution of another non-luminescent unit, usually a metal ion.

The elements used for doping belong to the third main group of the periodic table, termed lanthanides or rare-earths, containing the elements lanthanum (atomic no. 57) to lutetium (atomic no. 71). With increasing atomic number, the lanthanides show a periodic behavior of some of their properties (density, melting and boiling points), while other properties (e. g. ionic radii) change aperiodically. This aperiodic phenomenon is called *lanthanide contraction*.

The electron configuration of rare-earth atoms, responsible for the similarity in their chemical properties, is $[\mathrm{Xe}](4f)^n(5d)^x(6s)^2$ with $x = 1$ in the case of lanthanum ($n = 0$), gadolinium ($n = 7$), and lutetium ($n = 14$) and $x = 0$ and $n = 2$ through $n = 14$ for cerium through ytterbium. In general, the incorporation of rare-earth ions into a crystal matrix uses the trivalent form with an electron configuration of $[\mathrm{Xe}](4f)^{n+x-1}$.

The spectroscopic properties of trivalent rare-earths are characterized by intraconfigurational *4f-4f* transitions and interconfigurational *4f-5d* transitions. Due to the completely filled *5s* and *5p* shells of the [Xe] configuration, the electrons of the *4f* shell are effectively shielded from influences of the chemical environment, e. g. the surrounding crystal field, leading to low variations of the *4f*-states in different local environments [Bur62, Ray63]. Consequently, this insensitive character to the surrounding offers the advantage that the energy levels can be easily formed from those of free ions, and the influence of the crystal field is added as a small perturbation. In case of the investigated *4f-4f* electric dipole transitions, this results in narrow transition line-widths compared to those observed in transition metals, divalent rare-earths, and between RE^{3+} *5d*-states [Hen89].

As a result of the influence of the matrix, a slight shift of peak positions of *4f-4f* transitions can be observed. This behavior is known as the *nephelauxetic effect* (greek: cloud expanding). As the energies of the excited levels are primarily determined by interelectronic repulsion and spin-orbit coupling (see following section), a shift of the peak positions towards lower energy with increasing covalency of the surrounding media is expected. This fact makes the rare-earths suitable as probe ions for the crystallographic properties of their lattice sites. A detailed discussion of the nephelauxetic effect can be found in [Sin66].

Aside from europium, which can be used as a probe ion or as a red light emitter in phorphors, there are other rare-earths that are very promising dopant-ions for the sesquioxides. Most notable here are neodymium in scandia for operation at 1486 nm (telecommunications industry) and erbium in lutetia which is promising for high power operation at 2.7 µm for medical applications [Pet01].

2.3.1 Energy Levels of Free Ions

To calculate the electron states and their energies, the Hamiltonian must be determined and the Schrödinger equation has to be solved. The Hamiltonian for a free ion with a nucleus of charge Ze and N electrons of mass m_e is

$$\mathcal{H} = \sum_{i=1}^{N} \left(-\frac{\hbar^2}{2m_e}\Delta_{r_i} - \frac{Ze^2}{4\pi\varepsilon_0 r_i} \right) + \sum_{i<j=1}^{N} \frac{e^2}{4\pi\varepsilon_0 r_{ij}} \, . \tag{2.1}$$

The first summation describes the kinetic energy of the electrons as well as their Coulomb interaction with the nucleus, where r_i denotes the distance between the electron i and the nucleus. The second summation represents the electrostatic repulsion between the electrons which are seperarated by the distance $r_{ij} = |\mathbf{r}_i - \mathbf{r}_j|$. Because of this two-particle-operator, a separation of the Schrödinger equation in N one-particle-problems is not possible and hence no analytical solution can be found.

Using the central field approximation, where each electron moves in an effective spherically symmetric potential $V(\mathbf{r})$ created by the nucleus and the remaining $(N-1)$ electrons, the Hamiltonian is given by

$$\mathcal{H}_0 = \sum_{i=1}^{N} \left(-\frac{\hbar^2}{2m_e}\Delta_{r_i} + V(\mathbf{r}_i) \right) \, . \tag{2.2}$$

The resulting energy eigenvalue equation

$$\mathcal{H}_0\Psi_0 = E_0\Psi_0 \tag{2.3}$$

is separable, and considering the Pauli exclusion principle, the solution is

$$\Psi_0 = \prod_{i=1}^{N} |n_i l_i m_l m_s\rangle \, , \tag{2.4}$$

where the wavefunction Ψ_0 is built up as a Slater determinant out of one-electron spin orbitals. The energy eigenvalues of these eigenstates only depend on the quantum numbers n and l and are degenerated with respect to m_l and m_s.

In the central field approximation, two corrections have to be made: The non-spheric and non-symmetric part of the Coulomb repulsion interaction between the electrons

$$\mathcal{H}_{ee} = \sum_{i<j=1}^{N} \frac{e^2}{4\pi\,\varepsilon_0\,r_{ij}} - \sum_{i=1}^{N} \left(\frac{Ze^2}{4\pi\,\varepsilon_0\,r_i} + V(\mathbf{r}_i) \right) \, , \tag{2.5}$$

results in a splitting of the *4f* states in ${}^{2S+1}L$ states. The correction due to the spin-orbit interaction is

$$\mathcal{H}_{\mathrm{SO}} = -\sum_{i=1}^{N} \frac{1}{2m_e^2c_0^2} \frac{1}{r_i} \frac{\mathrm{d}V(\mathbf{r}_i)}{\mathrm{d}r_i} \, (\mathbf{s}_i \cdot \mathbf{l}_i) \, , \tag{2.6}$$

with $\mathbf{s}_i$ and $\mathbf{l}_i$ being the spin-vector of the i^{th} electron and the orbital angular momentum vector of the i^{th} electron, respectively. c_0 is the speed of light in vacuum. The Hamiltonian for the free ion can now be written as

$$\mathcal{H} = \mathcal{H}_0 + \mathcal{H}_{ee} + \mathcal{H}_{\text{SO}} \; . \tag{2.7}$$

If $\mathcal{H}_{\text{SO}}$ is the dominating part, the spin and the orbital angular momentum of each electron couple to the angular momentum $\mathbf{j}_i = \mathbf{s}_i + \mathbf{l}_i$ resulting in the total angular momentum $\mathbf{J} = \sum_i \mathbf{j}_i$. This case is termed *jj*-coupling. In the opposite case, where $\mathcal{H}_{ee}$ is the dominating term, the individual spins couple to the total spin $\mathbf{S} = \sum_i \mathbf{s}_i$, and the individual orbital angular momentums couple to the total orbital angular momentum $\mathbf{L} = \sum_i \mathbf{l}_i$. This coupling mechanism is termed LS-coupling or Russel-Saunders-coupling.

In lanthanide ions both correction terms tend to be of about equal magnitude resulting in an intermediate coupling scheme. It is common to label the energy eigenstates following the Russler-Saunders approximation ($^{2S+1}L_J$).

Additional perturbations, like spin-spin interactions or orbit-orbit-interactions as well as hypersensitive interactions, can be neglected as they are several orders of magnitude smaller than the observed interactions. A more important effect on the positions of energy levels of rare earth ions arises from the influence of the crystal field, which will be discussed in the following section.

2.3.2 Crystal Field Splitting

In a chemical environment (crystal, glass, solution), the spherical symmetry of the free ion is destroyed by the interaction of the *4f*-electrons of a lanthanide ion with the electrostatic field of the ligands (Stark effect). The influence of the local electric field $\mathbf{E}$, represented by the Hamiltonian

$$\mathcal{H}_{\text{Stark}} = -e \sum_{k=1}^{N} \mathbf{E}(\mathbf{r}_k) \cdot \mathbf{r}_k \; , \tag{2.8}$$

results in a Stark splitting of the $^{2S+1}L_J$ terms of a free ion, and the degeneracy with respect to M_J is repealed. For lanthanide ions having an odd number of electrons, the theorem of Kramers asserts a splitting in $(2J+1)/2$ twofold degenerated Stark levels (Kramers degeneration). Rare-earth ions with an even number of electrons experience a $(2J+1)$-fold Stark splitting.

As the *4f*-electrons are shielded from the crystal field by the *5s* and *5p* electrons, the influence of the pertubation $\mathcal{H}_{\text{Stark}}$ is one order of magnitude smaller than the contributions of $\mathcal{H}_{\text{SO}}$ and $\mathcal{H}_{ee}$. However, the interaction with the ligand field or with vibrational states mixes electronic states of different parity into the *4f*-wavefunctions. Due to this admixing, electric dipole transitions within the *4f*-shell, normally forbidden, are now partially allowed (see section 2.3.3).

2.3.3 Selection Rules

An oscillating electromagnetic field of appropriate frequency can be used for the excitation of an ion via an electron transition from the ground state to a higher energy level. Transitions between two energy levels can have either electric dipole (ED) or magnetic dipole (MD) character. Higher order transitions such as electric or magnetic quadrupole processes can usually be neglected due to their reduced transition probabilities [Die68, Pea75]. Electric dipole transitions require a change of parity of the electron wavefunction. Thus, due to the Laporte selection rule[1] electric dipole transitions within the *4f*-shell are (parity) forbidden and only magnetic dipole transitions are expected [Hen89].

In crystal fields without inversion symmetry, however, a mixing of opposite-parity states into the $4f^n$ states can occur resulting in a retension of the Laporte selection rule. Even if the crystal field shows inversion symmetry, intraconfigurational *4f-4f* transitions are observed as forced electric dipole transitions if the rare-earth ions occupy acentric sites in the matrix. The selection rules for these forced electric dipole transitions between $4f^n$ states are [Hen89, Kam90]

$$\begin{array}{llll} 1. & \Delta l = \pm 1 & 3. & \Delta L = 2l = 6 \\ 2. & \Delta S = 0 & 4. & \Delta J = 2l = 6 \end{array}$$

Additionally, for rare-earth ions with an even number of electrons the following selection rules are valid:

- $J = 0 \leftrightarrow J' = 0$ forbidden
- $J = 0 \leftrightarrow J' = 2, 4, 6, \ldots$ strong
- $J = 0 \leftrightarrow J' = 1, 3, 5, \ldots$ weak

The effect of admixing of states with opposite parity to the *4f*-states has been investigated intensively by Judd and Ofelt [Jud62, Ofe62].

The matrix of the sesquioxides provides two different lattice sites with symmetry C_2 and symmetry C_{3i} (see section 2.1). As the C_{3i}-sites show inversion symmetry, the effect of admixing is considerably small as compared to the C_2-sites, because there is no center of symmetry. Thus, the Laporte selection rule is stronger for ions occupying the C_{3i}-site, resulting in a reduced transition probability compared with transitions of ions in the C_2-site.

[1] The electric field can be expressed in terms of a multipole expansion. The first terms of order n of this expansion are called monopole ($n = 0$), dipole ($n = 1$), quadrupole ($n = 3$), and octupole ($n = 4$). The Laporte selection rules for electric multipole transitions of order n in a symmetric central field are:

- For $n = 0, 2, 4, \ldots$ only transitions between states of the same parity are allowed.
- For $n = 1, 3, 5, \ldots$ only transitions between states of different parity are allowed.

2.3.4 Interconfigurational 4f-5d and Charge Transfer Transitions

Apart from the intraconfigurational, parity forbidden *4f-4f*-transitions (weak), lanthanide ions show parity allowed transitions (strong), which appear as broad bands in optical spectra. These parity allowed transitions are the interconfigurational $4f^n \rightarrow 4f^{n-1}5d$ and charge transfer (CT) transitions.

Interconfigurational 4f-5d Transitions and Ligand Field Theory

In contrast to the *4f*-levels, the shielding of an electron in a *5d*-orbital by filled *5s*- and *5p*-shells is relatively ineffective and therefore, its energy is very sensitive to the environment. The position of the energy levels and the splitting due to the crystal field with respect to the site symmetry can be explained by the *ligand-field theory* (LFT) [Sch98].

The basis of this model, valid for electrons in non completely filled shells, is an extension of the crystal-field-theory to allow covalent interactions, whereas the bonding in LFT is generally explained by molecular orbital theory [Bal62].

It is assumed that the motion of electrons occurs in the potential of the metal ion core as well as in the electrostatic potential of the ligands. As the ligands are regarded as point charges, the interaction among the electrons of the central ion and the electrons of the ligands can be neglected. Therefore, in LFT the energy splitting is explained as a consequence of this electrostatic interaction, which requires a purely ionic bonding between the metal ion and the ligands without any covalent admixture.

A splitting of energy levels occurs because the orientation of the *d*-orbital wavefunctions will increase the electron energy when the orbital is extended into a region of high electron density, and vice versa. The total energy splitting Δ, or alternatively 10 Dq, is termed the crystal field stabilization energy. Δ may be estimated from

$$\Delta \approx \frac{\langle r^4 \rangle}{R^5} \, ,$$

where r is the radius of the *d*-orbital and R is the metal-ligand internuclear distance. A large crystal field splitting energy is provided by ligands with high negative charge and small radius, and by metal cations with a large oxidation number.

A more illustrative description of the *4f5d*-transitions is given in section 2.3.5, where the single configurational coordinate model is introduced.

Charge Transfer Transitions

A charge transfer transition is an interconfigurational transition which involves the ligand-to-metal charge transfer (LMCT) transition and the reverse process, a metal-to-ligand charge transfer (MLCT) transition. In general, a charge transfer state (CTS) is defined as an electronic state where a large fraction of an electronic charge is transferred from one region of a molecular entity (electron donor) to another (electron acceptor) [McN97]. Due

to the displacement of electronic charge across a typical interatomic distance the center of charge between the central ion and the ligands is considerably shifted with respect to the ground state producing a large transition dipole moment and a concomitant large oscillator strength.

The ligand-to-metal charge transfer process is often described as the transfer of an electron from the ligands to the central metal ion ($M^{n+}L^{m-} \rightarrow M^{(n-1)+}L^{(m-1)-}$) [Pie01] resulting in an excitation of an electronic state, which is called charge transfer state. In this model, a charge transfer state is then described by a hole transferred from the RE^{3+}-ion to the ligands, moving around the RE^{2+}-core in a potential field that is due to the effective negative charge produced by the lattice [Hos77].

The energy of a charge transfer band, E_{CT}, depends on the ionization energy of the donor and on the electron affinity of the acceptor as well as on the extent of the charge displacement. As the CT band energy correlates well with the Pauling scale of electronegativities, Jørgensen developed the concept of optical electronegativity [Jør70]. Thus, the energy E_{CT} can be estimated from the optical electronegativity of the anion, $\chi_{opt}(L)$, and the optical electronegativity of the central metal ion, $\chi_{opt}(M)$,

$$E_{CT} = [\chi_{opt}(L) - \chi_{opt}(M)] \times 30\,000\,\mathrm{cm}^{-1} \; . \tag{2.9}$$

For the investigated Eu^{3+}-ion in an oxide host matrix, the corresponding values are $\chi_{opt}(Eu^{3+}) = 1.8$ and $\chi_{opt}(O^{2-}) = 3.2$, resulting in an average CT band position of $42\,000\,\mathrm{cm}^{-1}$ in oxides. The band position is inversely proportional to the Eu–O distance. With increasing bond length the band shifts to lower energies [Hoe75].

The charge transfer state can be involved in absorption as well as in emission processes. Luminescence from a charge transfer state, however, can only occur if this state is lower in energy than the lowest energy level of an excited $4f^{n-1}5d$ state. In addition, no $4f$ energy levels must be present at energies comparable to the charge transfer state, because this will result in fast intersystem crossing to the lower energy $4f^n$ states and in $4f^n \rightarrow 4f^n$ emission. This mechanism is shown for Eu^{3+}:Y_2O_3 in figure 2.3. In this case, UV radiation is efficiently absorbed by a transition to the charge transfer state of the Eu^{3+} ion. Due to relaxation to the lower $4f$ levels (^5D_J manifold), no emission from the charge transfer state is observed. Rather, luminescence occurs from the $^5D_0$ state of Eu^{3+} [Nak79].

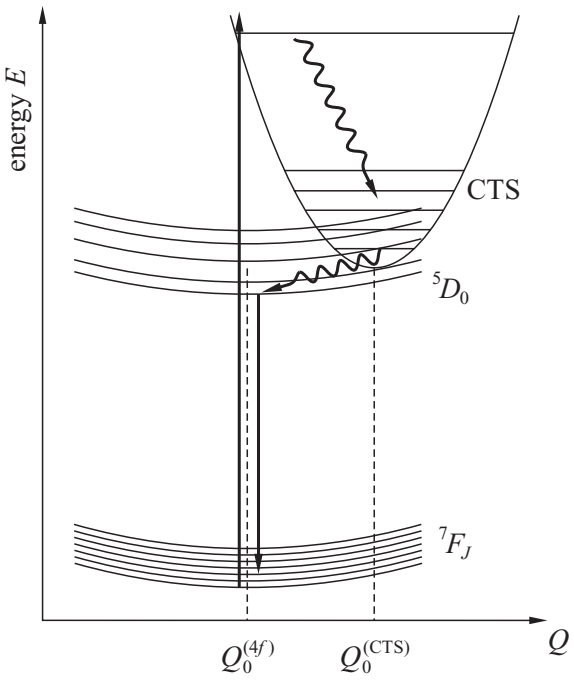

Figure 2.3: *CT excitation of Eu^{3+}:Y_2O_3.*

2.3.5 Influence of the Phonons

The vibrations of the host lattice have a significant influence on the optical transitions of the RE ions. An illustrative way to describe the electron-phonon coupling is given by the so-called *single configurational coordinate model* [Hen89]. This model is used to explain radiative and non-radiative transitions, the shape of an optical transition, i. e. narrow or broad lines, and the phenomenon of Stokes' Law.

The model is based on the *Born-Oppenheimer approximation* [Bor27], which states that the motion of the electrons can be separated from the motion of the nuclei (lattice vibrations). Thus, the eigenvalues $\phi(r_i, R_l)$ of the electron-phonon coupling can be written as

$$\phi(r_i, R_l) = \psi(r_i)\chi(R_l) \ , \tag{2.10}$$

where the electronic part $\psi(r_i)$ describes the eigenvalues of the Hamilton operator in a static lattice, whereas $\chi(R_l)$ describes the dynamics of the lattice (R_l is the position of the l^{th} ion). Additionally, all vibrational modes of the lattice (*phonons*) are represented by the so-called symmetrical stretching (or breathing) mode, which preserves the symmetry of the ligands around the metal ion.

The corresponding configurational coordinate diagram (see figure 2.4) shows the potential energy curves of a *4f* ground state, a *4f* excited state, and a *5d* excited state of a localized lanthanide ion as a function of the configurational coordinate Q. This coordinate describes the mean distance between the central ion and the ligands.

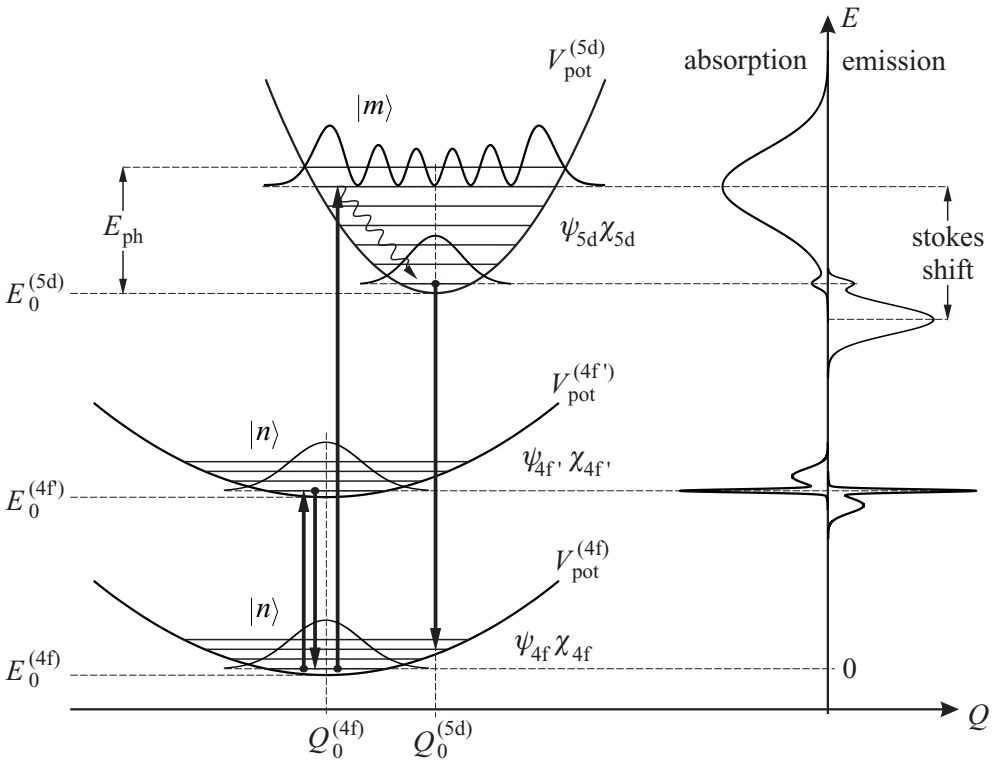

Figure 2.4: *Configurational coordinate diagram of the 4f and 5d states in a lanthanide ion.*

The curves in the configurational coordinate diagram are parabolic. This shape follows from the assumption that the vibrational motion is harmonic. In this case, the dependence of the potential energy V_{pot} on Q is quadratic,

$$V_{\mathrm{pot}} = \tfrac{1}{2}\, k\, (Q - Q_0)^2 \ . \tag{2.11}$$

The factor k represents the restoring force constant of the vibrational motion. The quantum mechanical solution of this equation yields discrete, vibrational levels of energy $E_m = (m + \frac{1}{2})\hbar\omega_m$, which are represented by horizontal lines.

The strength of the electron-phonon coupling is symbolized by the slope of the parabola: the wider the aperture of the parabola, the smaller the electron-phonon-coupling. This effect is illustrated in figure 2.4 for the *4f* and *5d* states in a lanthanide ion. As the *5d* states are more influenced by lattice vibrations, their restoring forces are larger than those of the *4f* states, i. e. $k(5d) > k(4f)$.

Due to different radial probability densities, each configuration of the active ion has a certain spatial extent resulting in a characteristic equilibrium configurational coordinate Q_0. Thus, the minimum of the excited state energy can change in position from that of the ground state energy.

Applying the Born-Oppenheimer approximation to transitions between electronic energy levels leads to the *Franck-Condon principle* [Con28], which states that electronic transitions occur much faster than nuclei can respond to their new equilibrium positions. The transition probability for a transition from the m^{th} into the n^{th} vibrational level of two different electronic states $|a\rangle$ and $|b\rangle$ is then given by

$$P_{|an\rangle \to |bm\rangle} = P^{\mathrm{el}}_{|a\rangle \to |b\rangle} |\langle m|n\rangle|^2 \ , \tag{2.12}$$

where P^{el} denotes the purely electronic transition probability. In the configurational coordinate diagram, the Franck-Condon-principle is considered by drawing radiative transitions as vertical lines, i. e. Q remains constant during the electronic transition.

Additionally, the broadening of the interconfigurational transitions and their huge Stokes shift compared to the intraconfigurational transitions can be illustrated in this diagram. As the parabolas involved in interconfigurational transitions are displaced against each other, the absorption from state $|n\rangle$ does not occur into the minimum, but into the side wing of parabola *5d*, occupying the vibrational state $|m\rangle$, which can relax non-radiatively into the minimum of parabola *5d* (see figure 2.4). In contrast, intraconfigurational transitions display very sharp absorption and emissions bands, because their equilibrium positions Q_0 are identical.

At temperatures $T > 0$, the vibrational states $|n\rangle$ and $|m\rangle$ are occupied thermally. Despite the broadening of the transition bands, of non-radiative transitions are possible. If a relaxed excited electronic state intersects the parabola of a less energetic excited electronic state or the electronic ground state, then a non-radiative transition via this intercrossing can occur. However, a non-radiative return to a less energetic excited state or the ground state is also possible due to the process of multi-phonon relaxation. To excite vibrations of the host via multi-phonon decay, the energy difference between two levels must not exceed more than five times the vibrational frequency of the host (effective phonon energy).

2.3.6 Europium

The Eu^{3+}-ion was chosen because of its high emission quantum yield, its relatively simple energy level scheme, and the possibility to use it as a structural probe for the sites occupied by the RE^{3+} in a given material [Bün89].

Although complex analytical tools are used for structural investigations of thin films, sometimes the local crystal structure can be determined more easily from the luminescence spectrum of a dopant or probe ion. In this context, the Eu^{3+}-ion is often used as a structural probe. The Eu^{3+}-spectrum consists of transitions between energy levels of the *4f*-electrons. As the ionic radii of Y^{3+} and Eu^{3+} are quite similar (0.92 Å and 0.98 Å, respectively), the influence of the dopant on the regular yttria lattice is negligible, and the Eu^{3+}-ions populate the two sites of different symmetry with equal probability [Heb70]. The positions and intensities of these transitions are strongly influenced by the surrounding crystal field.

In particular, the site symmetry of the dopant ion will be seen in the fluorescence spectrum. While the global electronic structure of Eu^{3+} is not affected by the host lattice, the symmetry of the local crystal field results in a splitting of the Eu^{3+} energy levels in a set of $(2J+1)$ sublevels (see section 2.3.2). The characteristic emission spectrum of the Eu^{3+}-ion can be analyzed easily because the most intense transitions originate from the excited $^5D_0$ state which is not split into sublevels due to the crystal field. The complete energy level scheme for Eu:Y_2O_3 is depicted in figure 2.5. The exact values for each Stark level can be found in appendix A.

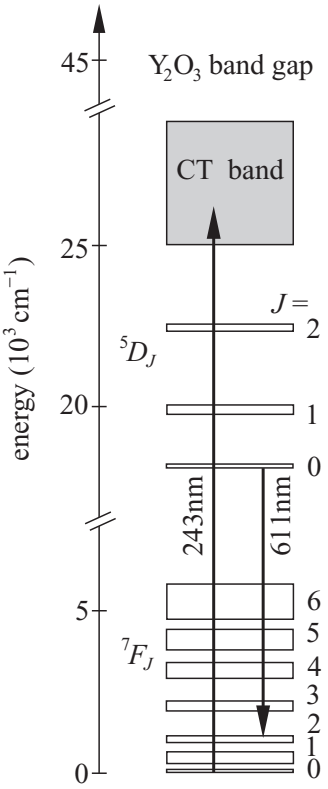

Figure 2.5: *Energy level scheme of Eu^{3+} in Y_2O_3.*

The excitation of the Eu^{3+}-ion into the charge transfer band around 243 nm results in the promotion of the electrons into the ^5D_J manifold due to non-radiative processes (see figure 2.5). The characteristic emission results from the $4f \rightarrow 4f$ electronic relaxation to the ^7F_J ground state manifold. Figure 2.6 shows a typical Eu^{3+} emission spectrum when Eu^{3+} is embedded in a crystalline Y_2O_3 matrix. It is characterized by an intense, narrow peak at 611 nm, arising from the hypersensitive $^5D_0 \rightarrow {}^7F_2$ transition of Eu^{3+} in the C_2 site. While the $^5D_0 \rightarrow {}^7F_1$ transition of Eu^{3+} occupying both the C_2 and C_{3i} sites is almost insensitive to the environment due to its purely magnetic dipole character, the intensities of the $^5D_1 \rightarrow {}^7F_{0,1,2}$ transitions are quite weak and respond very sensitively to the Eu-environment. Table 2.2 gives an overview of the $^5D_0 \rightarrow {}^7F_J$ transitions. The probability of a depopulation of the excited $^5D_0$ state by a non-radiative multiphonon process is very small as the energy gap between $^5D_0$ and $^7F_6$ is about 11 500 cm^{-1} large. Therefore, these processes would involve 30 phonons with an energy content of 400 cm^{-1} each. In contrast, non-radiative deexcitation of the $^5D_1$ state to the luminescent $^5D_0$ state requires only 4 phonons because the energy difference is only 1700 cm^{-1}.

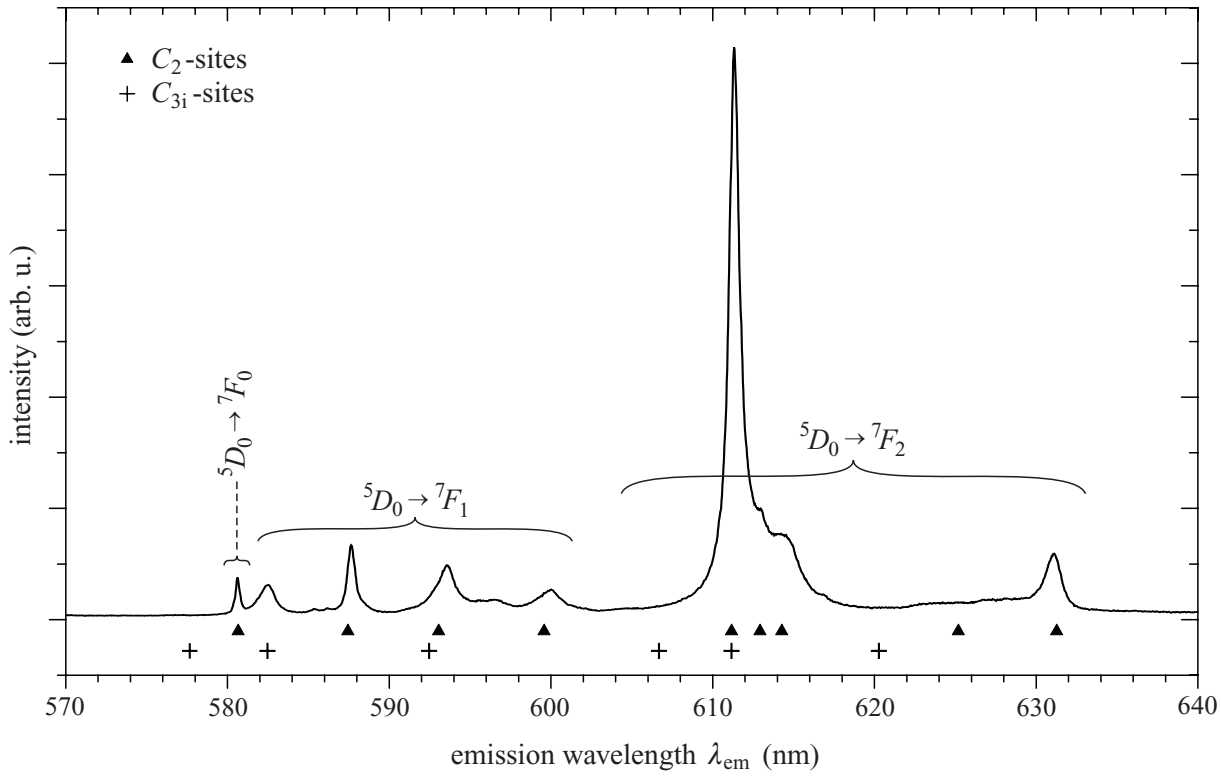

Figure 2.6: *Emission spectrum of Eu(1%):Y_2O_3 bulk crystal ($\lambda_{ex} = 243$ nm, spectral resolution 0.08 nm). The symbols indicate the emission from the two symmetry sites C_2(▲) and C_{3i}(+).*

transition	Di	range (nm)	I	comments
$^5D_0 \rightarrow {}^7F_0$	ED	577 - 581	vw	forbidden, nondegenerate; J-mixing gains intensity
$^5D_0 \rightarrow {}^7F_1$	MD	585 - 600	s	allowed; intensity independent from environment
$^5D_0 \rightarrow {}^7F_2$	ED	610 - 625	s-vs	hypersensitive ($\Delta J = 2$); absent on inversion center
$^5D_0 \rightarrow {}^7F_3$	ED	640 - 655	vw	forbidden; J-mixing adds allowed MD character
$^5D_0 \rightarrow {}^7F_4$	ED	680 - 710	m-s	sensitive to the Eu-environment ($\Delta J = 4$)
$^5D_0 \rightarrow {}^7F_5$	ED	740 - 770	vw	forbidden, seldom observed
$^5D_0 \rightarrow {}^7F_6$	ED	810 - 840	vw	seldom observed

Table 2.2: *Europium $^5D_0 \rightarrow {}^7F_J$ transitions;* Di *indicates the dipole character,* range *gives the approximately wavelength range of the transition, I gives the intensity of the transition, where* vw – *very weak,* m – *medium,* s – *strong,* vs – *very strong.*

3 Pulsed Laser Deposition

In 1962, Breech and Cross [Bre62] showed that material can be ablated by laser radiation. A few years later, Smith and Turner [Smi65] demonstrated the deposition of thin films by ablating material with a pulsed ruby laser for the first time. In this first pulsed laser deposition (PLD) experiment, they were able to produce 'optically satisfactory' films of, for example, Sb_2S_3, ZnTe, and $PbCl_2$. But it was not before 1987 that PLD became more attractive for growing films. Using this technique, Dijkamp et al. [Dij87] were able to fabricate thin films of the then new high-temperature superconductor $YBa_2Cu_3O_{4-\delta}$ (YBCO) with a degree of stoichiometric control superior to that achieved with evaporation or sputtering techniques. Nowadays, pulsed laser deposition is employed to produce crystalline thin films of epitaxial quality.

The technique of PLD is based on physical processes, arising from the impact of high-power pulsed laser radiation on solid targets and leading to the removal of partially ionized material (plasma) from the impact zone. This process takes place far away from equilibrium and involves a large number of complex physical and chemical mechanisms with a large number of variables.

This chapter will give a brief introduction to these mechanisms. There is a variety of articles and books published in which this technique is analyzed in more detail, e. g. [Bäu00, Chr94]. It is worth noticing the two review articles by K. L. Saenger [Sae93a, Sae93b] dealing with the processes involved in pulsed lased deposition. Saenger also gave a precise overview of the history of PLD as well as the physical mechanisms.

The PLD deposition process can be divided into the following four stages:

1. The laser radiation interaction with the target, which leads to ablation.
2. The following spatial expansion of the ablation products (plasma), including interaction and chemical reactions within the plasma.
3. The interaction of the ablation products with the substrate.
4. The nucleation and the growth of thin film on the substrate surface.

These four stages are shown in in the simplified scheme of figure 3.1. Since each stage influences the properties of the obtained films (crystallinity, stoichiometry, surface roughness), a short description of the different processes will be given in the following sections.

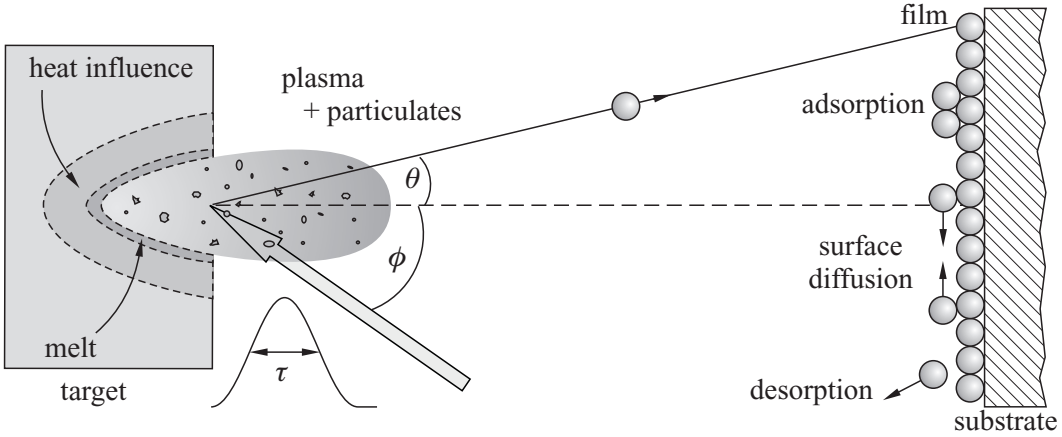

Figure 3.1: *Ablation and deposition processes* [Bäu00, Sae93a].

3.1 Laser–Target Interactions

The mechanisms of laser-induced material removal depend almost entirely on the target properties and the parameters of the used laser radiation (wavelength, power density, and pulse duration). In many cases, the material removal can be described as a thermal process where heat generated by the absorbed laser photons results in material vaporization. In some cases also non-thermal processes can take place. A possible non-thermal mechanism would be bond breaking due to photon excitation resulting in emission of atoms, molecules, and ions.

Laser-induced breakdown

The energy transfer from the laser radiation into a target of weakly absorbing material, e. g. a dielectric material, leading to its destruction is known as *laser-induced breakdown*. When laser-induced breakdown occurs, the electron density in the conduction band N_e is increased due to the laser irradiation [Blo74]. The consequence is a larger number of electron–phonon interactions and finally the material destruction if a critical value N_e^cr is exceeded. The duration of the energy transfer between the excited electron system and the lattice $\tau_{\mathrm{e-ph}}$ depends on the material and is in the order of 1 ps – 100ps.

The effect described above is based on 'free' electrons in the conduction band, which are present in dielectrics only in small numbers of $10^8\,\mathrm{cm}^{-3} - 10^{10}\,\mathrm{cm}^{-3}$ [Blo74]. There are, however, two possibilities how to create them when using high radiation intensities of $10^{11}\,\mathrm{W/cm}^2 - 10^{14}\,\mathrm{W/cm}^2$: either by non-linear multi-photon absorption (MPA) leading to ionization or by absorption of the laser radiation by electrons present in the conduction band (free-carrier-absorption) and subsequent avalanche ionization (AI). In the latter case, the few free electrons present are accelerated by the large electric field of the radiation. Surrounding atoms are ionized by collision with these high-energy electrons creating new free electrons which will also be accelerated. This results in an avalanche-like production of electrons.

The time dependence of the electron density N_e in the conduction band in the near-surface region during the presence of a laser pulse with intensity $I(t)$ can be described by the rate equation [Stu96]

$$\frac{dN_e}{dt} = \underbrace{\varepsilon_{av} I(t) N_e(t)}_{\text{AI}} + \underbrace{\gamma_m I^m(t)}_{\text{MPA}} . \tag{3.1}$$

In this equation, ε_{av} denotes the avalanche coefficient and γ_m the multi-photon absorption coefficient of order m (absorption of m photons), where m is the minimum number of photons required for a transition between the valence band and the conduction band.

The critical electron density N_e^{cr} is reached at a certain intensity, called threshold intensity I_{thr}, which is an important experimental parameter.

Defining the laser fluence Φ as the total energy per unit area per pulse,

$$\Phi = \int_0^\tau I(t)\, dt , \tag{3.2}$$

one can see from solving equation 3.1 that in case of having only the avalanche ionization the threshold fluence is independent of the pulse duration τ, e.g. $\Phi_{thr}(\tau) = \varepsilon_{av}^{-1} \ln(N_e^{cr}/N_0) = \text{const.}$. In the other limit, the case of pure m-photon absorption the threshold fluence scales with $\tau^{\frac{m-1}{m}}$, whereas a square-wave pulse is assumed. Thus, an experimental determination of Φ_{thr} can give a more detailed insight into the physical mechanisms leading to damage in dielectrics. In chapter 4, the experimental technique necessary for the determination of the threshold fluence as well as the result for a ceramic yttria target is presented.

If the interaction of the laser radiation with the target material persists for longer time periods (e. g. at pulse durations in the nanosecond regime) one has to consider the beginning of heating up the lattice during the duration of the pulse ($\tau \gg \tau_{e-ph}$). In this case, the expanding plasma can interact with the incoming laser beam (shielding effect) resulting in a reduced energy transfer into the target and changed plasma properties.

Heat-induced material removal

The energy deposited in the target leads to the heating up of the material due to electron–phonon coupling. It should be noted that this is true only for $\tau \gg \tau_{e-ph}$, i. e. ns-pulses, but not for ps- or fs-pulses. The volume of the heated region and the maximum temperature reached depend on the target optical properties (reflectivity $R(\lambda)$ and absorption coefficient $\alpha(\lambda)$) , and on the target thermal properties (specific heat C_v, the vaporization energy ΔH_v, and the thermal conductivity K).

An intuitive parameter for the characterization of the ablation mechanism is the thermal diffusion length L_{th} of the target which is related to the thermal diffusivity D_{th} by [Sae93b]

$$L_{th} = \sqrt{2 D_{th} \tau} = \sqrt{2 \frac{K}{\varrho\, C_v} \tau} . \tag{3.3}$$

L_{th} describes the spatial extension of the target zone influenced by. On this length the temperature is reduced by a factor of $e^{-1/2}$ with respect to the maximum value.

Considering the two limiting cases of very strong and very weak absorption shown in figure 3.2, it is possible to estimate the peak temperature that can be reached at the target surface. This temperature is responsible for evaporation and thus ablation of material.

In the first case, the optical penetration depth α^{-1} is small compared to the thermal diffusion length, i.e. $\alpha\sqrt{2D_{\mathrm{th}}\tau} \gg 1$. This condition is fulfilled for many materials deposited by PLD, because the laser wavelength for PLD is often chosen to coincide with strong target absorption. For most of these materials, this strong absorption occurs in the UV region so that excimer lasers at either 248 nm (KrF) or 193 nm (ArF) are favorable for the ablation process.

For the sesquioxides described in this thesis, the thermal diffusion length is in the order of $L_{\mathrm{th}} \approx 30\,\mu\mathrm{m}$ [1], and the optical penetration depth lies between 10 µm and 40 nm, i. e. $10\,\mu\mathrm{m} \gg \alpha^{-1} > 40\,\mathrm{nm}$, at the wavelength of the ArF-laser[2].

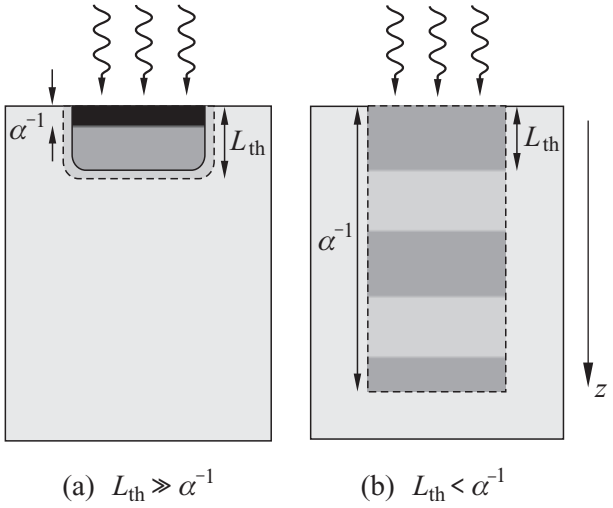

Figure 3.2: *Scheme of radiation absorption and target heating.*

Thus, for $L_{\mathrm{th}} \gg \alpha^{-1}$ the fluence absorbed during the laser pulse, $(1-R)I\tau$, is used to heat a layer of thickness L_{th}, and the final temperature in this volume is approximately given by [Sae93b]

$$\Delta T \simeq \frac{(1-R)I\tau}{\varrho C_{\mathrm{v}} L_{\mathrm{th}}} = \frac{(1-R)I\tau}{\varrho C_{\mathrm{v}}\sqrt{2D_{\mathrm{th}}\tau}} \,. \tag{3.4}$$

[1] Using the material parameters given in table 2.1 and a pulse duration of $\tau = 15\,\mathrm{ns}$, the thermal diffusion length can be calculated using equation 3.3:

$$L_{\mathrm{th}} = \sqrt{2K\varrho^{-1}C_{\mathrm{v}}^{-1}\tau} > \sqrt{2K\varrho^{-1}C_{\mathrm{p}}^{-1}\tau} \approx 30\,\mu\mathrm{m}\,.$$

In this case, C_{p} was used instead of C_{v} because no values where available for C_{p}. This is justified since $C_{\mathrm{p}} \geq C_{\mathrm{v}}$, where equality holds only for $T = 0$. Therefore a lower limit for L_{th} is obtained.

[2] The optical absorption depth α^{-1} is estimated from an absorption spectrum ($\alpha^{-1} \ll 10\,\mu\mathrm{m}$) [Mix99] and the values of n and k calculated by [Pal85]. The relation between α and k is given by [Bor75]

$$\alpha = 4\pi\lambda^{-1}k\,.$$

Application of this formula results in $\alpha^{-1} \approx 40\,\mathrm{nm}$ at $\lambda = 193\,\mathrm{nm}$ and $k = 0.427$.

In the second case, the optical absorption depth α^{-1} is larger than the thermal diffusion length, i.e. $\alpha\sqrt{2D_{\mathrm{th}}\tau} < 1$, and the absorption of radiation creates an exponential temperature profile along the depth z, i.e. [Sae93b]

$$\Delta T(z) = \frac{(1-R)\alpha I e^{-\alpha z}\tau}{\varrho C_{\mathrm{v}}} \ . \tag{3.5}$$

This means that heat is rapidly transported away from the ablation area leading to melting and, in some cases, evaporation of the target material. However, the desired congruent evaporation is usually prevented. Furthermore, at very high fluences, large absorption depths can result in superheating of a large volume. As a consequence of this heating process, the volume will be transformed into the melt phase and, due to rapid expansion, ejected from the surface resulting in molten droplets or particulates (see p. 30).

Nevertheless, if the absorbed energy per volume exceeds the energy density corresponding to the heat of vaporization $\varrho\Delta H_{\mathrm{v}}$, material removal is expected in both cases, i. e. very strong and very weak absorption. In the first case – important for PLD – this condition yields, that a threshold fluence

$$\Phi_{\mathrm{thr}} > \frac{\varrho\Delta H_{\mathrm{v}} L_{\mathrm{th}}}{(1-R)} \tag{3.6}$$

has to be reached before vaporization of material to a depth L_{th} can start. Due to the non-perfect target morphology the experimentally observed threshold values might be lower than the calculated values. In addition, non-homogeneous evaporation, e. g. ablation of clusters or particles, and multiple pulse effects have also an influence on the threshold intensity, and thus, cause a different experimentally observed value for I_{thr}.

From equations 3.3 and 3.6 it can be seen that the threshold fluence Φ_{thr} (see equation 3.2) for vaporization is proportional to $\sqrt{\tau}$, which is a direct consequence of one-dimensional heat flow for pulse durations $> \tau_{\mathrm{e-ph}}$. Regarding this relation, it is obvious that the use of very short pulse-length lasers (ps- instead of ns-pulses) should allow the same material vaporization at lower laser fluences or a higher vaporization rate for the same fluence. However, this does not imply that fs-lasers are more suitable for the ablation of material. As shown later, the interaction of the laser pulse with the developing plasma can have beneficial effects on the plume species.

Influence of Target Morphology

The surface of the target and its morphology can affect material removal in various ways. As it will be shown in section 3.2, the preferred direction of the expanding vapor plume is perpendicular to the target surface. If the surface is rough, the direction of the plume will change during the ablation process resulting in non-uniform films on the substrate. Another problem that can occur is the change of the morphology after irradiation with many laser pulses, due to recrystallization or to the development of macroscopic features such as craters. Structures like this can cause a bending of the plasma plume towards the incident laser beam, which again will lead to non-uniform material deposition [Bäu00].

Additionally, the thermal properties will influence the ablation, because the thermal diffusion length of a a sintered target may differ from that of a single crystal of the same material.

Usually, bulk materials (single crystals or amorphous materials) are used as targets to reduce the generation of particulates (see following section). However a compressed and sintered powder target may be preferred if the corresponding bulk material is transparent to the laser wavelength. In this case, absorption by the target will be enhanced by scattering effects [San85].

Stoichiometry of Removed Material

One great benefit of PLD is that the flux of material from the target usually matches the target stoichiometry, i. e. the vaporization is 'congruent'. This can be explained by the highly non-equilibrium process of pulsed laser heating. The pulsed ns-laser irradiation causes a very high heating rate (10^8 K/s) of the surface due to the large optical absorption coefficient and – in the case of sintered material – due to the poor thermal conductivity [Bec88] Thus, material removal occurs, before the individual components of the target material can segregate out into low and high vapor pressure components [Che88].

Particulate Generation

One of the major drawbacks of PLD is the deposition of particulates, which are produced together with the vapor during the ablation process. These particulates (their size ranges from several hundred nanometers to a few tens of micrometers) have an adverse effect on the growth of the subsequent layers resulting in a poor film quality. The reasons for the appearance of particulates vary: Particulates are generated due to a splashing effect, where a sub-surface layer of the target superheats above its vaporization temperature and blows off the molten overlayer resulting in liquid droplets [Rea63]. In contrast, Miotello and Kelly [Mio95] have shown that absorption (in combination with surface evaporation) does not lead to sub-surface layer superheating.

In the case of target outgassing, particles of the sintered target are ejected due to the expansion of the encapsulated gas. Fracto-emission describes the emission of particles from microcracks in the target. These effects can be minimized if single crystal targets are used instead of sintered ceramic targets.

Koren et al. [Kor89] found that the size and the content of the particulates also depends strongly on the wavelength used for ablating the material. The shorter the laser wavelength, the smaller the size of the particulates and the smaller their density. This wavelength-dependent effect can be explained by the reduced energy deposition depth, thus a thinner layer at the surface reaches the ablation threshold and a hotter plume with finer species develops.

To avoid problems associated with changes in the composition of the target surface [Auc88, Coh91] or with crater formation in the target, which results in a skewed plume direction

and a higher concentration of particulates [Bec88], it is necessary to irradiate a different part of the target surface with each laser shot. The most common to achieve this is to rotate the target, keeping the laser spot in a fixed position slightly displaced from the rotation axis resulting in ring-shaped ablation tracks.

No 'simple' correlation between film particulate content and target thermal properties [Dup89] could be found because of a variety of processes involved in particulate generation and because of the fact that these processes may be operative at the same time [Ugl77]. However, due to the fact that the velocities of particulates are one order of magnitude smaller than those of atoms and ions, it is possible to eliminate particulates by a high-speed velocity filter [Dup89, Bar69].

3.2 The Plasma Plume

As described in the previous section, the absorption of the incident laser radiation by the target leads to the evaporation of material. In this hot and dense vapor, which is initially confined to a very small volume near the target surface, many species may be present: atoms, molecules, ions, free electrons, and, in some cases, large particulates. If the content of charged particles exceeds a critical value, the vapor is called plasma, which is, in general, quasi-neutral (as many positive charges as negative charges).

In thermal equilibrium the degree of ionization, i. e. the ratio of the density of ions n_i to the density of neutral atoms n_0, can be derived from the Boltzmann distribution. The result is the so-called Eggert–Saha-equation [Egg19, Sah21]

$$\frac{n_i\, n_e}{n_0} = 2\,\frac{g_i}{g_0}\left(\frac{2\pi m_e kT}{h^2}\right)^{3/2} e^{-W_i/(kT)}\,, \tag{3.7}$$

where n_e denotes the electron density, m_e the electron mass, k is the Boltzmann constant, h is Planck's constant, and g_i and g_0 are the statistical weights of the electron–ion pair and the neutral atom, respectively. W_i is the ionization potential, i. e. the energy necessary to remove an electron from an atom.

There are limitations to the applicability of equation 3.7 because its derivation assumes isolated and non-interacting atoms, which is not true at high plasma densities. In this case, the overlap of the potentials of neighboring ions lowers the effective ionization energy, thus the degree of ionization is higher than predicted by the Saha–equation. In the limit of low densities it is possible that the condition of thermodynamic equilibrium is not be fulfilled.

In general, there is no sharp transition defined between the gas phase and the plasma phase (no thermodynamic transition), but it can bee seen from equation 3.7 that at temperatures of several 1000 K the degree of ionisation increases very quickly from nearly 0 to 1. For typical values ($W_i \approx 10\,\mathrm{eV}$, $T \approx 10\,000\,\mathrm{K}$) the plasma is initially characterized by neutral particle densities of the order of $10^{19}\,\mathrm{cm}^{-3} - 10^{20}\,\mathrm{cm}^{-3}$ and electron densities of the order of $10^{17}\,\mathrm{cm}^{-3} - 10^{20}\,\mathrm{cm}^{-3}$ [Sae93b].

Laser–Plume Interactions

At laser pulse durations of the order of nanoseconds one has to consider the interaction between the expanding plasma and the incoming radiation. On the one hand, as mentioned in section 3.1, the fraction of laser fluence reaching the target can be significantly attenuated by these laser–plume interactions. This has to be considered when using laser fluences highly above the threshold fluence. At fluences near the threshold value the size of the plasma plume is very small and the plasma is localized at the substrate surface. Increasing the fluence leads to a larger ablation volume and consequently resulting in an enlarged and denser plume, which interacts strongly with the incident laser radiation before reaching the target. Using sub-picosecond pulses these interactions can be ignored because plasma expansion velocities are $\lesssim 10^6$ cm/s [Bäu00].

On the other hand these interactions can have a positive influence on the deposition process by modifying the composition of the plume. Due to the absorption of one or more laser photons, the atoms and molecules in the plume can be dissociated, ionized and/or electronically excited thus the relative amount of ions increases with respect to neutral molecules and atoms. In addition, free electrons in the plume can be heated by *inverse bremsstrahlung* [3] whereby the electrons' kinetic energy is increased by the absorption of a laser photon in a collision process.

Plasma Expansion

The general dynamical behavior of plasma expansion has been compared to the dynamics of a free-jet adiabatic expansion [Kel92, Zhe89]. Both cases are characterized by a highly forward-peaked material flux and by an average particle speed that is many times higher than the mean random thermal speed.

One of the key parameters of film growth on the substrate is the kinetic energy of the arriving plume species. In thermodynamic gas theory this can be described by temperature. Assuming the adiabatic expansion of a high-pressure gas and the one-dimensional character of the expansion, the local temperature $T(z)$ and density $n(z)$ are related by [Nol94, Sae93b]

$$\frac{T(z)}{T_0} = \left[\frac{n(z)}{n_0}\right]^{\gamma-1} , \tag{3.8}$$

[3] In general, the term bremsstrahlung is used for radiation emitted by charged particles under deceleration when passing through the field of atomic nuclei. The energy emitted by an accelerated particle is proportional to $1/m^2$, where m is the rest mass of the particle, and therefore, bremsstrahlung plays an important role for light particles, like electrons. Thus, scattering of two electrons will lead to emission of radiation, i. e.

$$e^- + e^- \rightarrow e^- + e^- - \Delta E_{\mathrm{kin}} + h\nu$$

If intense radiation is used then the inverse process can occur (termed 'inverse bremsstrahlung'):

$$h\nu + e^- + e^- \rightarrow e^- + e^- + \Delta E_{\mathrm{kin}} .$$

In this case, a photon is absorbed and the kinetic energy of the electrons is increased correspondingly.

where T_0 and n_0 are the initial temperature and density, respectively, and $\gamma = C_V/C_p$ is the ratio of constant volume and constant pressure specific heats. In laser-produced plasmas with temperatures up to 10^5 K, γ is estimated to be around $1.2 - 1.3$ [Sin90, Sae93b]. During the spatial plasma expansion the temperature as well as the density of the plume will fall off. In a simplified spherical model the density falls of as the inverse cube of the distance from the target, i. e. $n(z)/n_0 \propto d^{-3}$ [Sin90].

This decreases the collision rate of the plume species and the random kinetic energy of the particles is converted to a directed motion away from the target. However, this behavior is valid only for supersonic sources, such as laser-produced plasmas, but nor for effusive sources, e. g in EBV processes.

Effects of the Background Gas

The considerations of the last section do not describe the expansion of the plume completely, because the expansion depends strongly on the presence of a background gas often used for deposition. In general, the plume transport and its appearance can be influenced considerably by any type of background gas. For example, scattering of the plume species can reduce the velocity and amount of material reaching the substrate, chemical reactions can change the initial composition of the plume resulting in changed optical emission characteristics and, due to physical confinement, the shape of the plume will be changed. In the case of reactive oxygen as background gas (this holds for all depositions presented in this thesis), one has to deal with the formation of Y^* and YO^* when growing Y_2O_3, where the asterisk indicates electronic excitation [Dye91]. The formation of YO^* is not an effect of the ablation process but is directly related to the exothermic $Y + O_2$ plasma–background gas reaction. These transformations will have an effect on the growth mechanism of the film on the substrate. If the deposition of oxides, like Y_2O_3, occurs at a very low oxygen pressure or in an inert atmosphere, the grown films are frequently not matching the correct stoichiometric composition, and the results are oxygen-deficient films.

After the successful introduction of plume-dynamics description using the similarity to adiabatic supersonic expansion of gaseous jets [Sae89], which gave an explanation of the plume angular distribution, Bulgakov and Bulgakova [Bul98] have developed a simplified model of the plume expansion in an ambient gas. This model is based on the theory of a supersonic jet formed when a high-pressure gas streams through a nozzle into a low-pressure gas (so-called underexpanded jet).

The gas-dynamic behavior of the plume can be divided into two physical regimes observed during the ablation process: on the one hand a nearly spherical plume expansion and on the other hand a mainly forward directed plume, which means that the flow of the ablated particles is aligned with the plume axis. Both expansion regimes are directly connected to the experimental conditions. In the case of short laser pulses ($\lesssim 20$ ns) and large spot radii of $\gtrsim 1$ mm (like in the experiments presented later in this thesis), one has to deal with the forward directed plasma. Under these conditions, the initial form of the plume is like a thin disc. Then, the expansion of the plasma can be sketched as follows (figure 3.3):

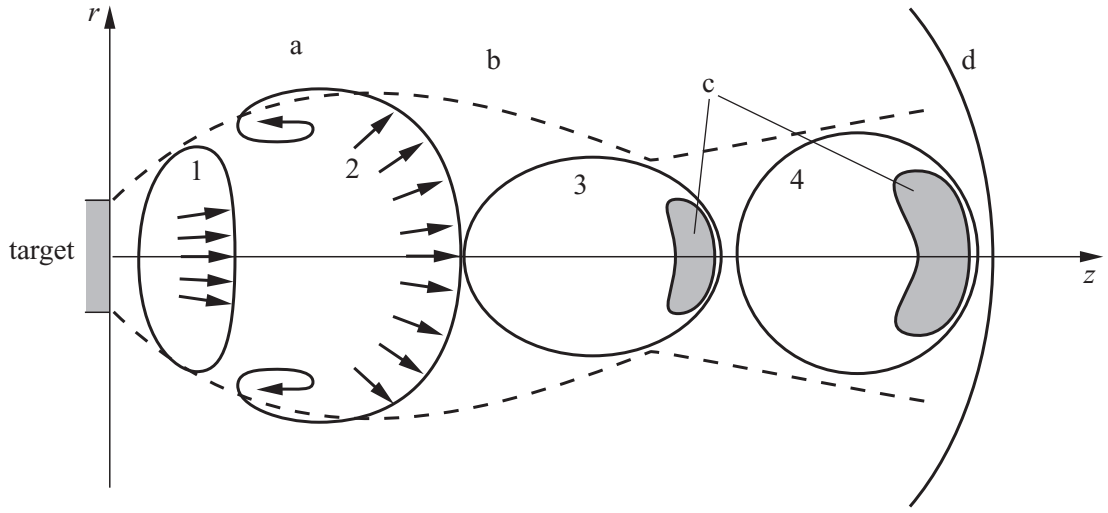

Figure 3.3: *Stages of plasma expansion in a background gas environment.(1)–(4) are the consecutive positions of the plume; (a) denotes the vortical motion arising at the plume periphery; broken line (b) shows the motion of the plume boundary point farthest from the plume axis z; (c) are the regions with the pressure increase in the front part of the plume and (d) is the shock wave ahead of the plume* [Bul98].

Moving away from the target, the disc-like cloud begins to broaden along the disc axis due to the velocity distribution of the particles and perpendicular to the disc axis due to the plume underexpansion (position 1 in figure 3.3). After passing the region where the cloud pressure equals the pressure of the background gas (position 2), the plasma plume slightly overexpands. This results in a decrease of the plume size (position 3), and the plasma passes the pressure equilibrium once more, thus its pressure exceeds the pressure of the background gas, and the plume expands again (position 4) with the same velocity as the background gas in the shock front (line (d) in figure 3.3). This shock front, generated by the rapid plume expansion at the beginning, can be described analogously to the *Mach disk* seen in supersonic[4] molecular beams. Finally, the plume will stop expanding due to the increasing interaction with the background gas. The maximum propagation length $R_{\max}$ of the plume from the target in a background gas of mass density ρ_b and at pressure p_b is given by [Bul95]

$$R_{\max} \sim \left(\frac{m_{\mathrm{abl}} E}{\pi \rho_b p_b} \right)^{1/6} ,$$

where m_{abl} is the ejected mass and E is the absorbed laser energy. If the final propagation length of the plume is shorter than the target–substrate distance, the deposition will proceed by diffusion resulting in low deposition rates.

During this expansion process the particle flow will be decelerated by the background gas leading to an increased pressure in the front part of the plume (regions (c) in figure 3.3). At this stage, mixing of the cloud material with the ambient gas takes place [Ani83].

[4]The ratio of the flow velocity u to the local speed of sound a is known as the Mach number $M \equiv \frac{u}{a} = u(\frac{\gamma kT}{m})^{-1/2}$. Expansions with $M > 1$ are termed *supersonic*.

The strong red YO^* chemiluminescence observed in experiments dealing with yttrium compounds [Fri93] is the result of this mixing.

Plume Angular Distribution

As depicted in the model of the plume expansion in an ambient gas the plume is usually oriented along the surface normal of the target. This is also valid for laser radiation incident non-normally because the irradiated surface of a perfectly planar, isotropic target has no 'memory' of the direction from which the absorbed photons came. In practice, plume tilting cannot be avoided because real targets are usually not perfectly planar. One has also to take into account that the laser beam intensity profile may be asymmetric or non-uniform. For example, a *hot spot* at the center of the laser beam profile may introduce asymmetries in target irradiance due to the shadowing effects of the denser plasma above the corresponding hot spot on the target [Sae93b].

Apart from these experimental deviations of the plume direction one can relate different contributions of the plasma distribution to distinct physical origins. The source of the evaporation, i. e. the irradiated spot on the target, can be treated as a small-area effusive source, which is defined by the ratio $d/h \ll 1$ where d is the diameter of the source (approximately the laser spot size) and h is the target–substrate distance. The emission distribution of such a source can be described by a $\cos\theta$ law [Mai83].

This single cosine fit only holds for the broad structure observed in the plume angular distribution while the enhanced forward peaking of the plume is commonly approximated by a $\cos^n\theta$ function, where values for the exponent n range from one to more than 200. As a result, the angular distribution is fitted by a superposition of a cosine and a $\cos^n$ function in the form

$$a\cos\theta + b\cos^n\theta \ .$$

In general, this two-component structure can be applied to all species, neutral atoms and ions, in the plasma plume. However, A. Thum-Jäger and K. Rohr [Thu99] found that the angular profiles depend on the degree of ionization and that for ions with a charge $q \geq 2e$ the emission can already be well described by a $\cos^n$ fit alone.

In addition, the shape of the distribution varies for species of different mass whereas a relative enrichment of the lower mass elements near $\theta = 0$ is observed.

On the one hand the narrow angular distribution of the ejected plume towards the substrate can lead to high deposition rates and prevents extensive chamber contamination. On the other hand, however, (and this is a major drawback of PLD) this can result in nonuniform film thickness and inhomogeneous stoichiometries over large deposition areas.

3.3 Growth Mechanisms

In general, thin-film formation can be described as a kinetic adsorption and diffusion process of the plume species on the substrate surface. This process can be divided in the states of nucleation, coalescence, and subsequent thickness growth, where all stages can be influenced by deposition parameters. This section summarizes the mechanisms underlying nucleation and film growth. A more detailed description can be found in [Kai02, Met94].

In PLD, the vapor responsible for the film growth on the substrate is characterized by an extremely high degree of supersaturation (10^5 J/mole), i. e. far away from the thermodynamical equilibrium, a high degree of ionization, and high kinetic energies of the species. Depending on the laser parameters employed and the background gas these kinetic energies can range between 10 and several 10^4 eV. Hitting the surface these high-energy species can influence the film growth positively as well as negatively, i. e. they can improve or deteriorate the overall morphology, stoichiometry, and microstructure of the growing film. In the worst case, the impact of high-energy species can result in bond breaking, generating subsurface vacancies and displacement or removal of surface atoms. However, at energies usually achieved during the the deposition process, the kinetic energy of the species enhances the surface diffusion of adsorbed atoms, i. e. the adatom will diffuse through several atomic distances on the substrate before sticking to a stable position within the newly forming film. The different atomic processes that can occur during film growth are presented in figure 3.4. These interactions determine the morphology of the growing film.

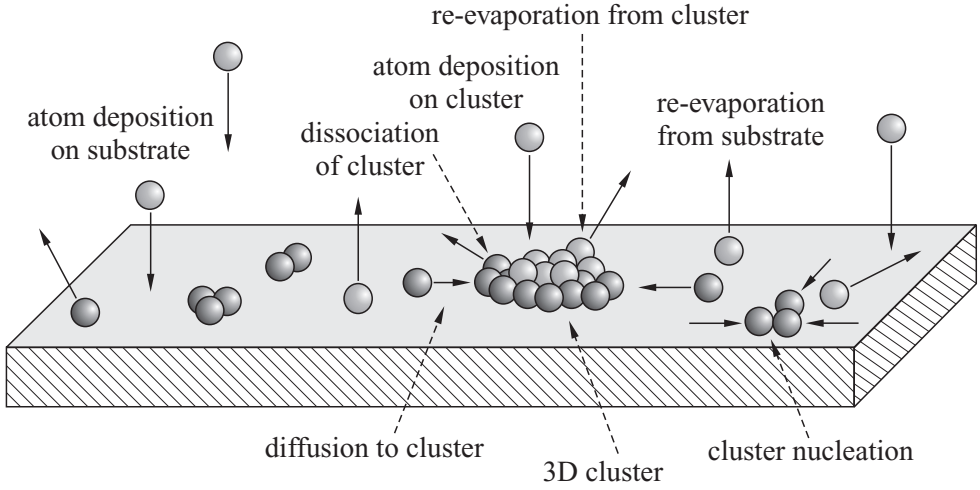

Figure 3.4: *Possible mechanisms during film growth.*

With a background gas present, the plume species will undergo not only collisions within the plasma but also with the ambient gas. These collisions reduce both the ion fraction and the kinetic energy of the evaporated target material. When reaching the substrate, the energy of the species can be reduced to thermal levels, and the adatoms do no longer possess sufficient mobility to migrate to the correct lattice site. To obtain the right crystalline structure nevertheless, substrate heating is required to increase the adatom mobility at the surface.

Depending on the ratio of the substrate temperature T_{sub} to the melting temperature of the material T_{m}, different basic processes can be expected to dominate at different ranges of $T_{\mathrm{sub}}/T_{\mathrm{m}}$. This concept has been extented to the so-called *structure zone model*, after which the real structure is made up of three zones [Kai02]. The first zone is characterized by lower substrate temperatures, i. e. $T_{\mathrm{sub}}/T_{\mathrm{m}} < 0.3$. Consequently, the adatoms have a low mobility and stick to the substrate where they impact on the surface. The result is a fine-grained porous structure. The temperature region $0.3 < T_{\mathrm{sub}}/T_{\mathrm{m}} < 0.5$ corresponds to activation energies of $0.1\,\mathrm{eV} - 0.3\,\mathrm{eV}$, which leads to surface diffusion, and a columnar structure is obtained. At high substrate temperatures $T_{\mathrm{sub}}/T_{\mathrm{m}} > 0.5$, the growth of large crystalline grains is facilitated by bulk diffusion. Additionally, the process of recrystallization (a complete change of the crystal orientation) or a phase transition can occur at high temperatures T_{sub} and large film thicknesses.

In general, higher substrate temperatures lead to better crystal structures until a point is reached where re-evaporation of the more volatile elements in the film will lead to nonstoichiometric growth. The formation of the nuclei and their growth depends not only on the substrate temperature but mainly on the interaction energies of substrate atoms and film atoms. Since flat surfaces without defects do not exist in nature, defects, e. g. dislocations, kinks, vacancies, and ledges, act as favored nucleation sites [Ven00]. Thus, the strength of the adatom bonding to the substrate compared to the bond strength of its surrounding neighbors determines the initial stage of film growth. The relation between the surface energy of the substrate γ_{s} and the surface energy of the growing film γ_{f} is given by Young's equation,

$$\gamma_{\mathrm{s}} = \gamma_{\mathrm{i}} + \gamma_{\mathrm{f}} \cos\varphi \,, \tag{3.9}$$

where γ_{i} is the interface energy film–substrate and φ is the wetting angle of a nucleus on the substrate. Depending on these interaction energies one can distinguish three modes of film formation [Bau58]:

a) **Layer-by-Layer growth**: In this case the interaction between substrate and film atoms is greater than between adjacent film atoms ($\gamma_{\mathrm{s}} > \gamma_{\mathrm{f}} + \gamma_{\mathrm{i}}$), and the layers grow one on top of the other (so called two-dimensional Frank-van-der-Merwe mode).

b) **Island growth**: Separate three-dimensional islands are formed on the substrate if the interaction between film atoms is greater than between adjacent film and substrate atoms ($\gamma_{\mathrm{s}} < \gamma_{\mathrm{f}} + \gamma_{\mathrm{i}}$). This growth mechnism is termed Volmer-Weber mode.

c) **Layer-plus-Island**: In the Stranski-Krastanov mode (a hybrid form of the two growth modes described above), one or two monolayers form first followed by individual islands because the interface energy increases with film thickness; typically the layer on top of the substrate is strained to fit the substrates' lattice constant.

In recent years, intensive research in the field of active opto-electronic elements that consist of island films has been carried out. As an example of optically active molecules, the Stranski-Krastanov layer-plus-island growth of Ge-islands upon Si-substrates for the production of self-assembled quantum dots may be mentioned [Vin00].

Lattice Matching

An important type of thin film growth is the epitaxial growth, in which the grown film has a crystallographic correlation with that of the substrate. If the deposit consists of the same material as the substrate this process is called homoepitaxy, otherwise heteroepitaxy. The quality of epitaxially grown films is strongly influenced by the substrate, and in general, single-crystalline growth is only possible on substrates with a similar lattice spacing. The lattice mismatch f between film and substrate is defined as

$$f := \frac{a_{0,\mathrm{f}} - a_{0,\mathrm{s}}}{a_{0,\mathrm{f}}} \,, \tag{3.10}$$

where a_0 is the lattice spacing and subscripts 'f' and 's' refer to film and substrate, respectively. In the case of homoepitaxy, the crystal lattice of the substrate is continued in the growing film, and no dislocations and stress due to lattice mismatch are expected. Especially for the production of waveguides, a low rate of growth errors at the interface is neccessary, thus homoepitaxy should be favorable. However, the disadvantage of homoepitaxy for waveguides is the small difference in the refractive indices because this difference is only achieved by the dopant. This change is of the order of $\Delta n = 3 \times 10^{-4}$ per percent of doping [Iva75].

A higher index-of-refraction difference can be obtained by heteroepitaxy. Frank and van der Merwe [Fra59] have shown that epitaxy between materials with different chemical characters and different lattice constants is possible. In this case, the lattice parameters of the growing film fit the substrate lattice constant by elastic deformations in the potential field of the substrate surface. This growth process is termed pseudomorph. Depending on the lattice constant of the deposit compared to that of the substrate, compressive stress ($a_{0,\mathrm{f}} > a_{0,\mathrm{s}}$) or tensile stress ($a_{0,\mathrm{f}} < a_{0,\mathrm{s}}$) can be distinguished.

In general, elastic deformation occurs for small lattice mismatch and small film thickness. Lattice mismatches of up to 7% can be accommodated by strain in thin films of a few monolayers. With increasing mismatch or film thickness, the formation of point defects and dislocations to relax strain is energetically favorable. The result is a plastic deformation, i. e. irreversible deformation. This process leads to the Stranski-Krastanov growth mode, resulting in polycrystalline growth or growth of small 'micro-crystallites' [Tan98].

In some systems, the orientation of the substrate for the growth of a certain crystalline phase is not that important. Providing enough adatom mobility, polycrystalline growth [Che01] or even single crystalline growth [Hu96] can be possible on completely amorphous substrates. This growth mode occurs if a certain growth direction is energetically favorable compared to elastic and plastic deformation. This effect has been observed in yttria films on silica [Pon02, Seo02, Zha98]. Thus, there is no general rule based solely on the value of the lattice mismatch to predict the film growth behavior, because the lattice parameters and the deposition temperature as well as the mechanical properties of the substrate and film material and the formation energies of the different defects play an important role.

This work focuses on crystalline rare-earth-doped sesquioxide films. As these films are optically active, the number of defects that have a negative influence on the luminescence (unsaturated bonds, color centers, dislocations, symmetry and coordination defects)

should be minimized. The investigated films have a cubic structure whereas the substrate consists of a hexagonal matrix. In this case, lattice matching is achieved due to different crystallographic orientations. The hexagonal sapphire structure offers a lattice constant of $a_{Al_2O_3} = 4.759\,\text{Å}$. As it can be seen from figure 3.5, the cubic lattice of the sesquioxides offers a hexagonal arrangement of the ions in the cubic {111} planes. For the investigated $Al_2O_3 - Y_2O_3$ system one gets the relation

$$3 \times a_{Al_2O_3} \approx \sqrt{2} a_{Y_2O_3} \ . \tag{3.11}$$

Using definition 3.10, the lattice mismatch for Y_2O_3 on sapphire is 4.8%. In case of the sesquioxides Lu_2O_3 and Sc_2O_3, the mismatch is only 2.8% and -2.5%, respectively.

To obtain 'perfect' lattice matching, the lattice constant can be customized by mixing the sesquioxides, e. g. $(Lu_xSc_{1-x})_2O_3$. These mixed crystals can be described as solid solutions, where the substituents are distributed completely disordered in the matrix, but occupying the correct lattice site. As the sesquioxides behave chemically and physically identical, most of their properties are not changed in a mixed system. In binary solutions, like $(Lu_xSc_{1-x})_2O_3$, the lattice constant is a linear function of x, and thus the new lattice constant a' can be calculated easily by the following equation, termed Vegard's law,

$$a' = x\,a_1 + (1 - x)\,a_2 \ , \tag{3.12}$$

where a_1 and a_2 are the lattice constants of the pure single crystals [Veg21]. Applying this equation to the system $(Lu_xSc_{1-x})_2O_3$ on α-alumina one gets the value $x = 0.459$, e. g. the composition for lattice matching is $(Lu_{0.459}Sc_{0.541})_2O_3$ (or $Lu_{0.918}Sc_{1.082}O_3$). It is also possible to obtain lattice matching with $(Y_xSc_{1-x})_2O_3$, where $x = 0.331$. Since these solid solutions are easy to prepare and a stoichiometric transfer from the target to the substrate is ensured, films of $YScO_3$ have been prepared. Since only a $YScO_3$ single-crystal ($x = 0.5$) was available as target, the lattice mismatch in these films is 1.25% with respect to the substrate.

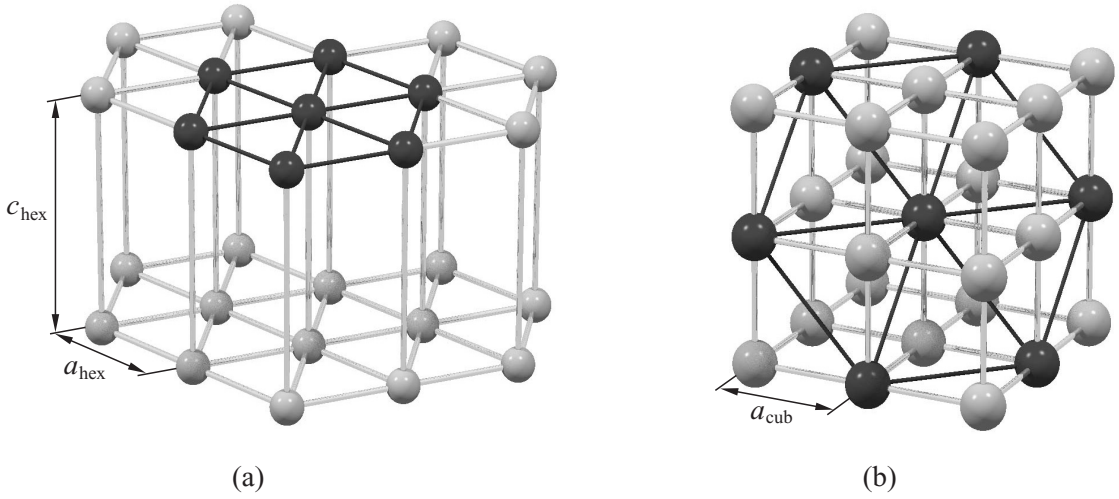

Figure 3.5: *Hexagonal structure (a) and cubic structure (b). In order to visualize characteristic planes, some atoms are displayed in a different color.*

4 Thin Film Preparation by Pulsed Laser Deposition

This chapter gives a detailed description of the preparation of thin sesquioxide films using the technique of pulsed laser deposition (PLD). The films presented in this thesis have been grown at the Instituto de Óptica, Consejo Superior de Investigaciones Científicas (CSIC), Madrid (Spain).

As discussed in the previous chapter thin film preparation by pulsed laser deposition involves different physical and chemical processes. Thus, the quality and the characteristics of the films depend on a variety of parameters. The most important parameters are listed below, including a comment on typical values in the used setup:

- laser wavelength (193 nm, fixed)
- laser pulse energy (energy density on the target)
- pulse duration ($\tau = 15\,\mathrm{ns}$, fixed) and pulse form (fixed)
- laser repetition rate ($\nu_{\mathrm{rep}} = 10\,\mathrm{Hz}$, but variable)
- type of background gas (N_2, O_2)
- background gas pressure ($10^{-6}\,\mathrm{mbar} < p < 1\,\mathrm{mbar}$)
- target density and target morphology
- target–substrate distance (3.5 cm, fixed)
- substrate temperature ($T_{\mathrm{sub}} = 20 \ldots 700°\mathrm{C}$)

The targets used for ablation were either sintered sesquioxide powders or sesquioxide single crystals. The sintered targets were prepared as follows: Rare-earth-doped sesquioxide powders (purity $\geq 99.99\%$) were cold-pressed into a pellet of 2.54 cm in diameter. The density after applying a pressure of 276 bar was around $2.66\,\mathrm{g/cm^3}$ which is 53% of the density of a single crystal of Y_2O_3. To increase the density, the pellets were sintered for 72 h in air at a temperature of 1700°C and then slowly cooled down to room temperature (0.8°C/min). The estimated density of these pellets (diameter after cooling 2 cm) was around $4.53\,\mathrm{g/cm^3}$ which is 90% of the single-crystal density. In general, a higher density should result in improved laser evaporation characteristics which results in films with superior properties [Sin92]. Additionally, targets of single-crystal sesquioxides have been used for comparison. These crystals (Nd:Lu_2O_3, Er:Sc_2O_3, Yb:$YScO_3$) were grown at either by the Czochralski method or the heat-exchanger method [For99, Mix99, Pet01].

All targets were cleaned prior to deposition by ablation with 300-500 pulses under the deposition atmosphere to ensure a homogeneous surface morphology. During the deposition process, the targets were continuously rotated to reduce the influence of crater formation on the target surface and to avoid stoichiometric changes in the target material (see section 3.1, p. 29).

The substrates of c-cut α-Al_2O_3, provided by CrysTec Kristalltechnologie (Berlin, Germany), had a size of 10 mm × 10 mm × 0.5 mm and were polished on both sides with an RMS-roughness of < 0.4 nm. Prior to deposition, they were ultrasonically cleaned in a sequence of trichlorethylene, acetone, and alcohol. The substrates were placed at a fixed distance of 3.5 cm in front of the target holder, where up to four targets could be attached. This construction has the advantage that multi-layered systems can be prepared without opening the vacuum chamber.

In figure 4.1, the setup of the pulsed-laser-deposition system used for thin film production is shown. The main component is the stainless steel vacuum chamber containing the target and substrate holders. The ArF excimer laser (Lambda Physics LPX 210i fluorine) operating at a wavelength of $\lambda_{\mathrm{ArF}} = 193$ nm and a pulse duration of $\tau_{\mathrm{ArF}} = 15$ ns (FWHM) was computer-controlled via a frequency generator. The duration of an ablation sequence was regulated by the number of laser pulses (control of the film thickness) and the repetition rate, which was set to $\nu_{\mathrm{rep}} = 10$ Hz for all film depositions.

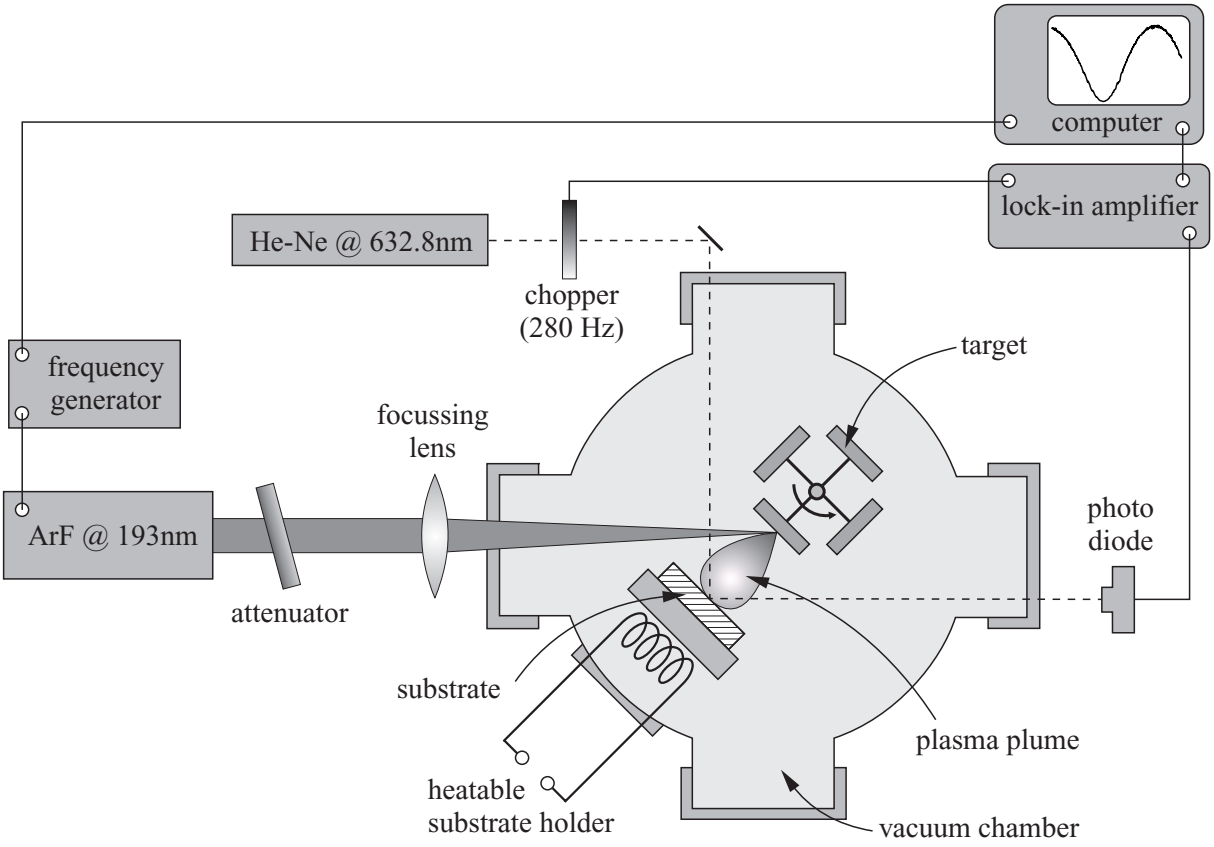

Figure 4.1: *Schematic setup for the pulsed laser deposition.*

Prior to ablation, the chamber was evacuated with a turbo molecular pump (Pfeiffer-Balzers TSU 512) down to a base pressure of $p_{\text{base}} = 2.1 \times 10^{-6}$ mbar. Using a rotary pump (Leybold Trivac D8B), the chamber was refilled with oxygen. It was found that the optimum partial pressure of oxygen for the deposition process of Y_2O_3 was around $p(O_2) = 5 \times 10^{-2}$ mbar.

The energy of the laser pulses at the target position were measured with a Molectron JMAX 43 detector. By an additional measurement of the ablation spot size ($A_{\text{spot}} = 0.01\,\text{cm}^2$) the laser fluence Φ (see section 3.1, p. 27) could be determined. To ensure a homogeneous mode intensity distribution the laser energy was set to the maximum value of 350 mJ and then reduced to the desired value by an attenuator. Y_2O_3 targets were irradiated with an energy of 21 mJ resulting in a laser fluence of $\Phi = 2.1\,\text{J/cm}^2$. Since Lu_2O_3 and Sc_2O_3 have higher ablation thresholds with respect to Y_2O_3 a fluence of $\Phi = 4.15\,\text{J/cm}^2$ was used to obtain identical growth rates. The approximate growth rates of Y_2O_3, Lu_2O_3, and Sc_2O_3 were 0.12 Å/pulse, 0.15 Å/pulse, and 0.15 Å/pulse, respectively.

Film thickness and growth rate were determined by in-situ reflectometry via lock-in technique using a He-Ne-laser ($\lambda_{\text{HeNe}} = 632.8\,\text{nm}$). For this purpose, the films were grown at room temperature on silicon substrates because the refractive index difference in the $\text{Si} - \text{RE}_2\text{O}_3$-system is larger than in the $\text{Al}_2\text{O}_3 - \text{RE}_2\text{O}_3$-system, leading to a better contrast in the reflectivity (see figure 4.2). Neither the change of substrate (Si instead of Al_2O_3) nor the change of temperature nor the change of substrate temperature have a significant influence on the growth rate. Therefore, the results can be applied to the $\text{Al}_2\text{O}_3 - \text{RE}_2\text{O}_3$-system.

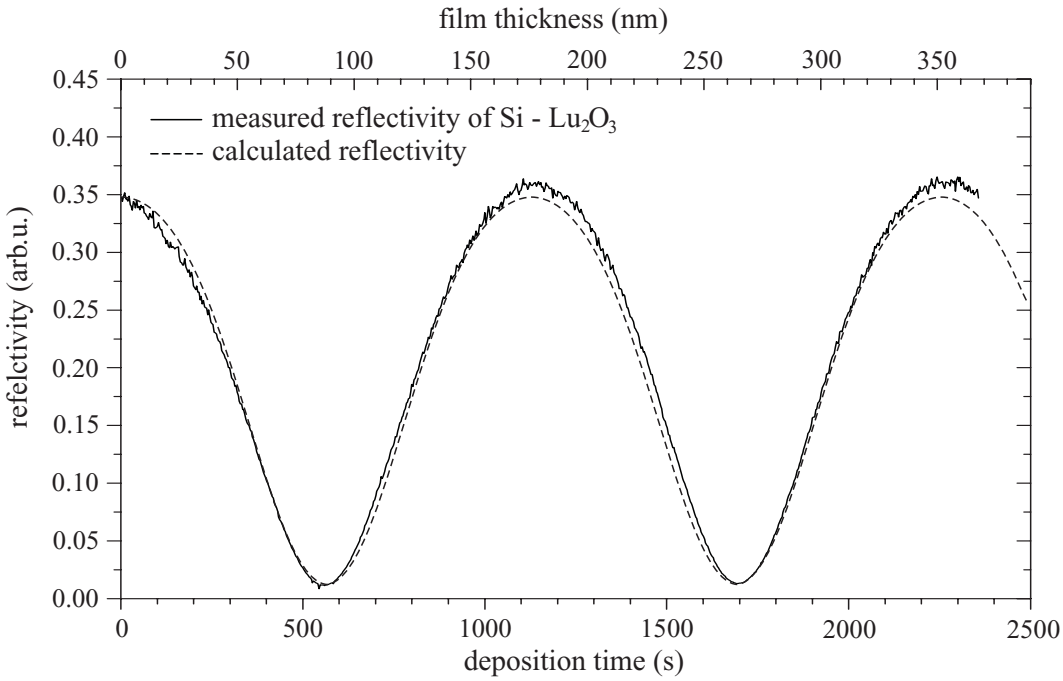

Figure 4.2: *Simulated and measured reflection behavior of a growing Lu_2O_3 film on silicon. The growth rate was determined to be 0.15 Å per pulse at a laser fluence of $\Phi = 4.15\,J/cm^2$.*

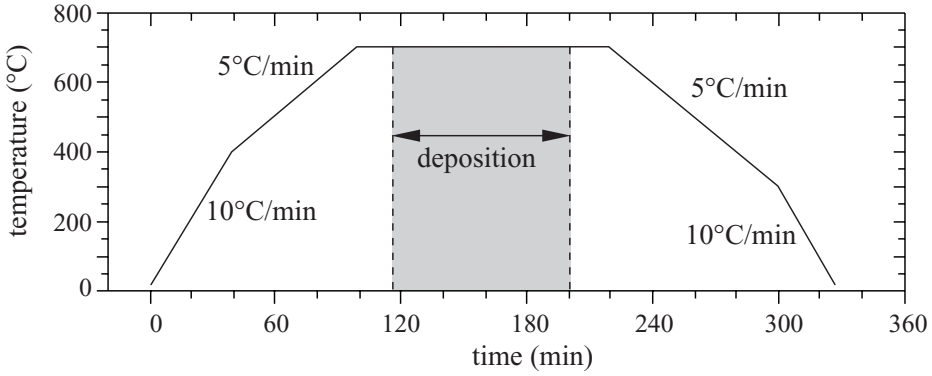

Figure 4.3: *Substrate heating cycle.*

The substrates were heated by a boron nitride heating element ($I_{max} = 3.5\,A$, $U_{max} = 32\,V$) up to 700℃ before starting the deposition process. To ensure a good heat transfer, the substrates were directly attached to the boron nitride element by a stainless steel substrate holder. The temperature was measured inside the substrate holder, approximately 1 mm away from the target, using a thermocouple. To avoid thermal problems in the substrate and in the grown films, the temperature was increased and decreased with different rates in different temperature regimes. This process, which is shown in figure 4.3, was managed by a programmable EUROTHERM control unit. Up to a temperature of 400℃, a fast heating rate of 10℃/min was used. Then, the ramp was set to 5℃/min to avoid thermal stress in the substrate. During the deposition, the temperature was kept constant at 700℃. Due to the different thermal expansion coefficients of the sesquioxides and the alumina substrates (p. 13), which might result in thermally induced damage, the cooling process started slowly with a cooling rate of 5℃/min and was later set to 10℃/min. Neither cracks in the films nor partly flaked-off films have been observed. Therefore,it can be concluded that the different thermal behavior has no macroscopic influence on the films.

As mentioned in section 3.2, the PLD process is characterized by a plume angular distribution, which can lead to non-uniform deposition. This effect is stronger the closer the substrate is placed in front of the target. In the used PLD setup, this distance was only 3.5 cm, resulting in a non-uniform film thickness. Figure 4.4 shows an optical micrograph of a 500 nm thick Y_2O_3 film grown on a silicon substrate. One can clearly see Newton fringes caused by film-thickness variations. For yttria films grown on sapphire by PLD with a target–substrate distance of 10 cm no fringes were observed indicating more uniform film growth [Bur02]. The production of films with a homogeneous and uniform thickness is important for possible applications, especially for the envisaged waveguide technology.

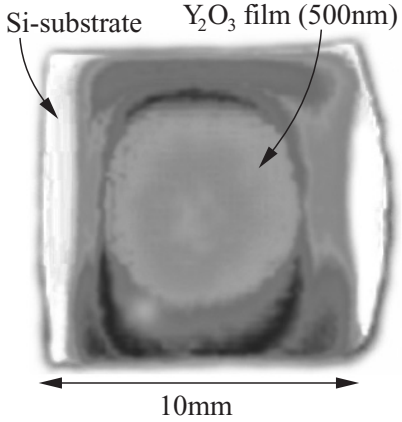

Figure 4.4: *Optical micrograph of a non-uniform PLD-film.*

A list of all sesquioxide films fabricated by PLD can be found in appendix B, table B.1 (including the experimental parameters).

Threshold Laser Fluence Determination

The fluence Φ (energy per unit area) of any temporal and spatial intensity profile I of a laser pulse is obtained by

$$\Phi(x,y) = \int_{-\infty}^{\infty} I(x,y,t)\mathrm{d}t \; . \tag{4.1}$$

The laser pulse energy is

$$E_{\mathrm{pulse}} = \int_{-\infty}^{\infty}\int_{-\infty}^{\infty} \Phi(x,y)\mathrm{d}x\mathrm{d}y \, . \tag{4.2}$$

In general, a direct measurement of the fluence is not possible because the fluence on the target surface depends strongly on the focussing. Thus, a number of techniques have been developed to obtain the fluence from the pulse energy E_{pulse}, for example the moving-knife-edge method or imaging with a CCD camera. Since these methods require a very high experimental precision (laser stability, positioning), an alternative method based on target modifications due to pulsed laser radiation is used for fluence determination [Liu82]. This method will be introduced in the next paragraph:

Considering a single pulse of a radially symmetric Gaussian beam with a $1/e^2$-radius w_0 and a maximum fluence Φ_0, the fluence distribution can be written as

$$\Phi_{\mathrm{Gauss}} = \Phi_0 \exp\left[-2\left(\frac{r}{w_0}\right)^2\right] \; . \tag{4.3}$$

Applying equation 4.2 results in

$$\Phi_0 = \frac{2E_{\mathrm{pulse}}}{\pi w_0^2} \, , \tag{4.4}$$

i. e. the maximum fluence depends linearly on the pulse energy.

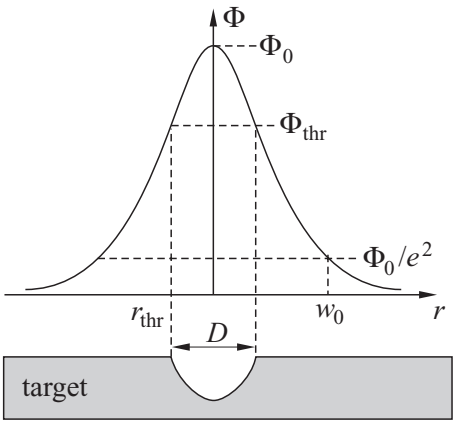

Figure 4.5: *Ablation using a gaussian beam profile.*

The beam radius can be obtained by analyzing the damaged area on the target (see figure 4.5). Since surface damage can only occur in the region where the threshold fluence is exceeded, an analytical relation between the diameter of the damaged area and the maximum fluence Φ_0 can be found. Due to ablation, a crater of diameter D and maximum depth h is formed. The threshold fluence $\Phi_{\mathrm{Gauss}}(r_{\mathrm{thr}}) = \Phi_{\mathrm{thr}}$ is reached at the edge of the damaged zone. Thus, one gets

$$D^2 = 2w_0^2 \ln\left(\frac{\Phi_0}{\Phi_{\mathrm{thr}}}\right) \tag{4.5}$$

Now, equations 4.4 and 4.5 can be used to determine the threshold fluence Φ_{thr}.

Apart from the ablation threshold, other modifications visible on the target surface and their thresholds can be detected, e. g. oxidization, amorphization or re-crystallization. In addition, these effects can be investigated not only by energy variation but also by applying different numbers of laser pulses at the same spot. Thus, multiple-pulse experiments allow the investigation of accumulative and incubation effects. For example, the ablation threshold fluence of InP for fs-pulses decreases with the number of laser pulses per spot [Bon00].

In the present case, single pulse damage on the target surface is hardly visible. Therefore, the number N of laser pulses was set to $N = 3$. However, the model presented cannot be applied straightaway because the beam profile of the ArF excimer laser is not Gaussian, but has a rectangular shape. Therefore, the profile was first fitted in the x and y direction with a 'Super Gauss' (SG) function [Sie86]. In analogy to equations 4.3 and 4.4 one gets the laser fluence Φ_{SG},

$$\Phi_{\mathrm{SG}} = \Phi_0 \times \exp\left[-2\left(\frac{x}{w_{0x}}\right)^4\right] \exp\left[-2\left(\frac{y}{w_{0y}}\right)^4\right] , \tag{4.6}$$

and the laser pulse energy (following equation 4.2)

$$E_{\mathrm{pulse}} = \Phi_0 \int_{-\infty}^{\infty} \exp\left[-2\left(\frac{x}{w_{0x}}\right)^4\right] \exp\left[-2\left(\frac{y}{w_{0y}}\right)^4\right] \mathrm{d}x\mathrm{d}y = 2.32 \times \Phi_0\, w_{0x}\, w_{0y} . \tag{4.7}$$

The dimensions of the resulting ablation crater can then described similar to equation 4.5:

$$D_x^4 = 8w_{0x}^4 \ln\left(\frac{\Phi_0}{\Phi_{\mathrm{thr}}}\right) = 8w_{0x}^4 \ln\Phi_0 - 8w_{0x}^4 \ln\Phi_{\mathrm{thr}} \tag{4.8}$$

$$D_y^4 = 8w_{0y}^4 \ln\left(\frac{\Phi_0}{\Phi_{\mathrm{thr}}}\right) = 8w_{0y}^4 \ln\Phi_0 - 8w_{0y}^4 \ln\Phi_{\mathrm{thr}} . \tag{4.9}$$

In figure 4.6, three ablation spots due to irradiation with three laser pulses each are presented. The energy of these pulses was decreased from spot (I) to spot (III). Beside the main spot (a), two smaller craters (b) close to the main spot are created by the laser pulses. This effect is the stronger the higher the laser fluence on the target and can be explained by the non-uniform intensity profile of the laser beam, which has a shape similar to a diffraction pattern with 0^{th} order and 1^{st} order. Thus, at low energies the threshold fluence is not reached in the '1^{st} order' maxima and no ablation takes place. However, at higher energies the threshold fluence is exceeded also in these smaller intensity peaks, resulting in visible ablation spots.

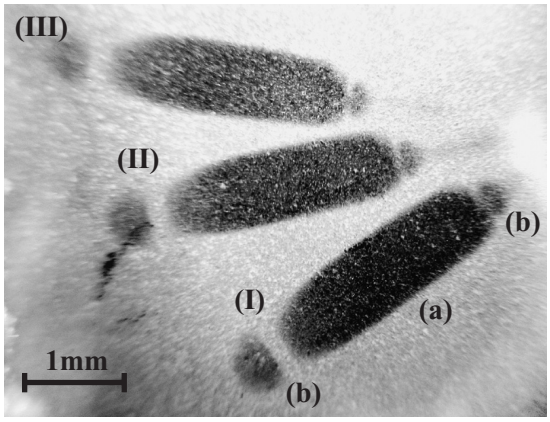

Figure 4.6: *Ablation spots of the ArF excimer laser on a single crystal Y_2O_3-target.*

Now the threshold fluence can be determined as follows: The fourth power of the measured crater dimensions (limited to the spot size of (a)), i. e. $D^4_{x/y}$, is plotted semi-logarithmically versus the corresponding pulse energy E_{pulse} to obtain the beam radius $w_{0y/0y}$. Using equation 4.7, for every pulse energy the corresponding fluence is calculated. Then, from the $(D^4_{x/y} - \ln \Phi_0)$-graph (see figure 4.7), the threshold fluence can be determined by fitting the experimental data according to equations 4.8 and 4.9, respectively. From the intersection of this graph with the $(D^4_{x/y} = 0)$-line, the threshold fluence can be calculated.

Since the energy density necessary for ablation is a material parameter, the values of Φ_{thr} should be the same for the x and the y direction. However, in this case, the target was a sintered Y_2O_3 pellet and the threshold fluences were determined to be $\Phi_{\mathrm{thr},x} = 0.5\,\mathrm{J/cm^2}$ and $\Phi_{\mathrm{thr},y} = 0.2\,\mathrm{J/cm^2}$ (see figure 4.7). This difference in threshold fluences is mainly caused by deviations of the laser beam profile from the 'Super Gauss' form, which was used for fitting the data. In addition, the influence of the small ablation spots close to the 'main' spot has been neglected.

However, both values are of the same order of magnitude. Therefore, the following relation can be assumed for the upper and lower limit of the threshold fluence of yttria upon nanosecond laser irradiation at 193 nm:

$$0.2\,\mathrm{J/cm^2} < \Phi_{\mathrm{thr}}(Y_2O_3) < 0.5\,\mathrm{J/cm^2}\ . \tag{4.10}$$

Thus, the fluence used in ablation experiments for thin film deposition (see p. 43) was more than 3.4× higher than the threshold value.

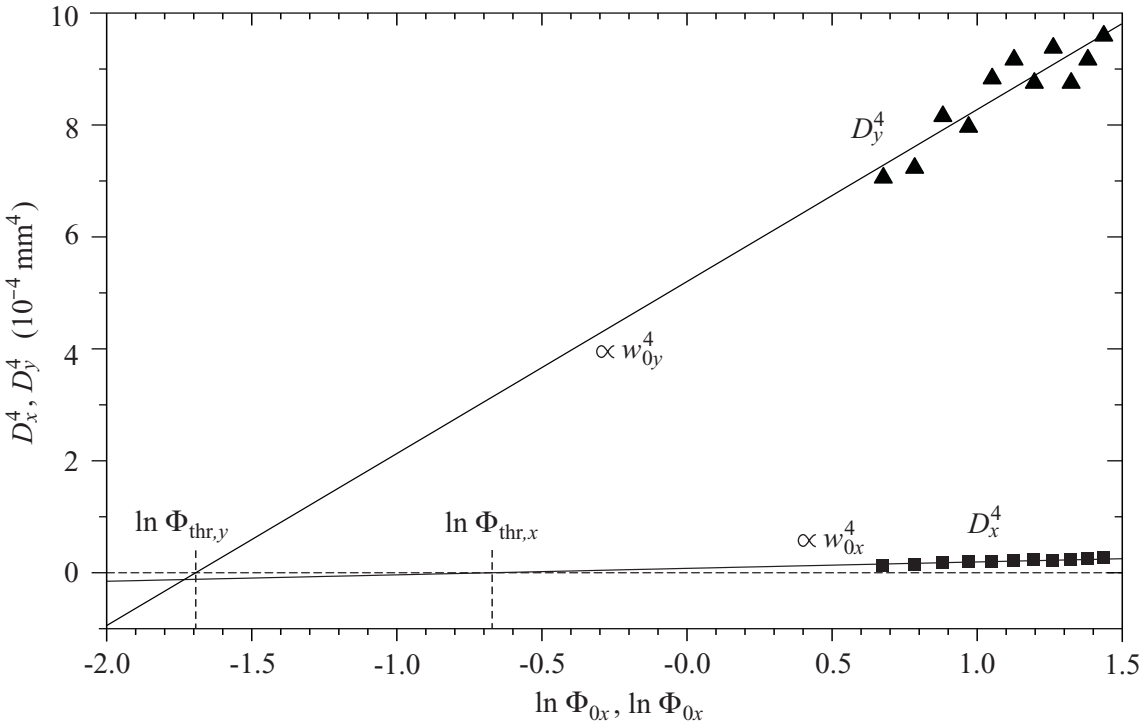

Figure 4.7: *Experimental determination of the laser fluence ablation threshold* Φ_{thr}.

5 Analytical Techniques and Thin Film Characterization

Modern materials technology is mainly based on the modification of the surface and the interface regions of solids. As thin film deposition, especially in semiconductor physics, has reached an advanced level where control on the monolayer scale can be achieved, it is necessary to define the desirable qualities of the deposited films and the according analytical tools to examine these parameters. For example, an efficient planar waveguide laser should have the same chemical composition as the equivalent bulk crystal and reach a high degree of crystallinity, as the crystallinity directly influences the optical and thermal properties [Bar01]. The characterization process to obtain the required information about the films can be split into two parts, namely

- structural characterization (crystallinity, stoichiometry, surface morphology)
- optical characterization of the dopant (luminescence, lifetimes).

The analytical tools for examining the structure of the films are X-ray diffraction and surface X-ray diffraction (crystallinity), Rutherford backscattering (quantitative elemental composition analysis), and atomic force microscopy (surface morphology). These techniques and their application are described in sections 5.1 - 5.3.

To study the optical properties of the rare-earth-doped sesquioxide films, fluorescence and excitation measurements (including VUV excitation measurements) have been performed. These experiments and their results are presented in section 5.4.

5.1 X-Ray Diffraction

The method of X-ray diffraction (XRD) is a non-destructive technique for examining the degree of crystallinity, the texture, the lattice constants, and the phase of a crystal, To do this a monochromatic X-ray beam of wavelength λ is directed onto a crystalline material at different angles θ.

A crystal lattice is a regular three-dimensional spatial distribution (cubic, rhombic, etc.) of atoms. These are arranged periodically to form a series of parallel planes separated from each other by a distance d.

When X-rays pass through a crystal, the intensity of the scattered rays shows a pattern that is the result of the interference of the individual waves scattered by each atom, i. e. at the inner shell electrons of the atoms (Thomson scattering). If the sample is a single crystal or polycrystalline, the X-rays will be scattered from successive planes of atoms. Generally, the scattering from these planes will be out of phase. To interfere constructively, resulting in a reflected beam of maximum intensity, the X-rays must have a difference in path length that is equal to the wavelength λ or an integer number of wavelengths (see figure 5.1). These conditions are summarized in the Bragg diffraction law [Ash76]

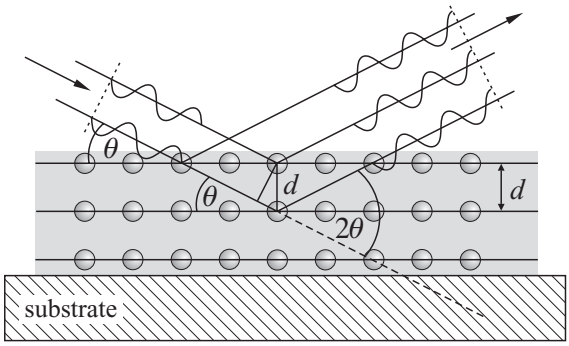

Figure 5.1: *X-ray diffraction.*

$$2d \sin\theta = N\lambda \tag{5.1}$$

where d is the inter planar spacing, λ the X-ray wavelength, and N the order of diffraction. Using the Miller indices[1], the Bragg condition 5.1 can be re-written as $2d_{hkl} \sin\theta = \lambda$. For cubic crystals with lattice constant a (like the investigated sesquioxides) the distance d of the atomic planes is given by

$$d = \frac{a}{\sqrt{h^2 + k^2 + l^2}} \,. \tag{5.2}$$

From the two equations 5.1 and 5.2, the first order diffraction scattering angle of a plane (hkl) can be calculated:

$$\sin\theta = \frac{\lambda}{2a}\sqrt{h^2 + k^2 + l^2} \,. \tag{5.3}$$

The intensity of the diffraction peaks contains information about the texture. In general, the term texture is used as a synonym for the non-random or preferred crystallographic orientation in a polycrystalline material. The higher the intensity the more crystallites are oriented in the same direction. The texture of a film can be determined by comparison with the intensities of the corresponding powder diffraction pattern However, the intensity $I(h,k,l)$ of a diffraction peak is determined by the distribution of the electrons in the unit cell and thus it is proportional to the squared absolute value of the structure factor $F(h,k,l)$

$$I(h,k,l) \propto |F(h,k,l)|^2 = \sum\nolimits_r f_r \, e^{2\pi i(hu_r + kv_r + lw_r)} \tag{5.4}$$

where f_r is the atomic form factor, which represents the Fourier transform of the charge density of the r^{th} atom, and u_r, v_r, and w_r are the coordinates of the r^{th} atom of the basis.

[1]Miller indices are a symbolic vector representation of the orientation of an atomic plane in a crystal lattice. They are defined as the reciprocals of the fractional intercepts which the plane makes with the crystallographic axes. The result is a set of three integer numbers h, k, and l. The indices are used in four different vector notations: (hkl) crystal plane, $\{hkl\}$ equivalent planes, $[hkl]$ crystal direction, and $\langle hkl \rangle$ equivalent directions.

Additional information about the structure is provided by the width of the diffraction peaks. Due to various effects (strain, defects, finite size effects, instrumental resolution), the observed diffraction peaks are broadened. The width of the peaks $\Delta 2\theta$ is defined as the full width at half maximum (FWHM). Assuming that the grown films show no stress, the finite size of the crystallites B ($B \gg \lambda$) can be estimated by the Scherrer equation[Cul78]

$$B = \frac{0.89\,\lambda}{(\Delta 2\vartheta)\,\cos\theta}\,. \tag{5.5}$$

Here, the expression $\Delta 2\vartheta = \Delta 2\theta - \Delta 2\theta_{\mathrm{ref}}$ is the corrected linewidth, where $\Delta 2\theta$ is the observed linewidth and $\Delta 2\theta_{\mathrm{ref}}$ is a reference linewidth of an 'infinite' extented single crystal. The broadening of the single crystal diffraction peaks is then limited only by the resolution of the apparatus [Cul78].

An alternative description of this scattering process uses the reciprocal lattice. The incoming and reflected X-rays are described by the corresponding wavevectors $\mathbf{k}$ and $\mathbf{k}'$, respectively. Because of the elastic scattering of the X-rays, the magnitude of the wavevectors does not change, i. e. $|\mathbf{k}| = |\mathbf{k}'| = k = 2\pi/\lambda$. Constructive interference can be observed if the change of the wavevector $\Delta\mathbf{k}$ is equal to a vector of the reciprocal lattice $\mathbf{G}$. This scattering mechanism can be illustrated by a simple geometrical construction, called Ewald construction or Ewald sphere, as it can be seen in figure 5.2. Considering a simple cubic lattice, the reciprocal lattice is also cubic with a lattice constant $a^* = 2\pi/a$. As described above, intensity is observed if $|\Delta\mathbf{k}|$ equals the interplanar distance $a^*\sqrt{h^2+k^2+l^2}$. This leads to the condition

$$|\Delta\mathbf{k}| = 2k\sin\theta = \frac{4\pi}{\lambda}\,\sin\theta = \frac{2\pi}{a}\,\sqrt{h^2+k^2+l^2} \tag{5.6}$$

which is equivalent to equation 5.3 derived from the Bragg diffraction law 5.1.

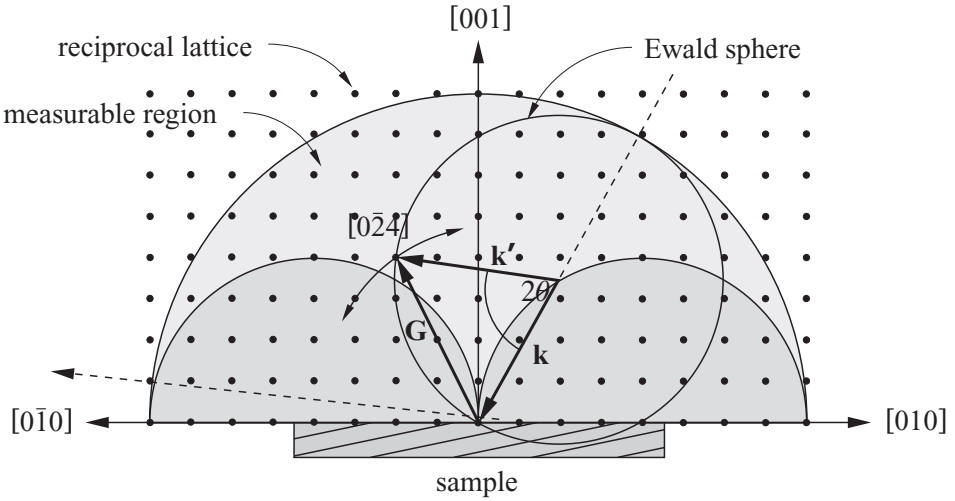

Figure 5.2: *Construction of the Ewald sphere and the geometrical interpretation of a rocking curve to get information about the distribution of planes which are not parallel to the sample surface.*

5.1.1 Bragg-Brentano Setup

The most simple arrangement of X-ray tube, sample, and detector is the setup in Bragg-Brentano geometry as shown in figure 5.3. The X-ray source at one arm of a goniometer stage emits X-rays which hit the sample at an angle θ with respect to the sample surface, and which are diffracted towards the detector situated in the other goniometer arm at 2θ from the direction of the incident beam. By varying the angle θ, Bragg's law is fulfilled for different d-spacings in polycrystalline material. In the experiments, the XRD stage PHILIPS X'PERT has been used in the Bragg-Brentano geometry. The X-ray source was Cu-Kα_1 radiation with a wavelength of $\lambda = 1.5406\,\text{Å}$. The spot on the film had a rectangular shape with the dimension $8\,\text{mm} \times 5\,\text{mm}$ at $\theta = 30°$. A step size of $\Delta 2\theta = 0.02°$ and a detector integration time of $\Delta t = 0.5\,\text{s}$ have been used during the measurements.

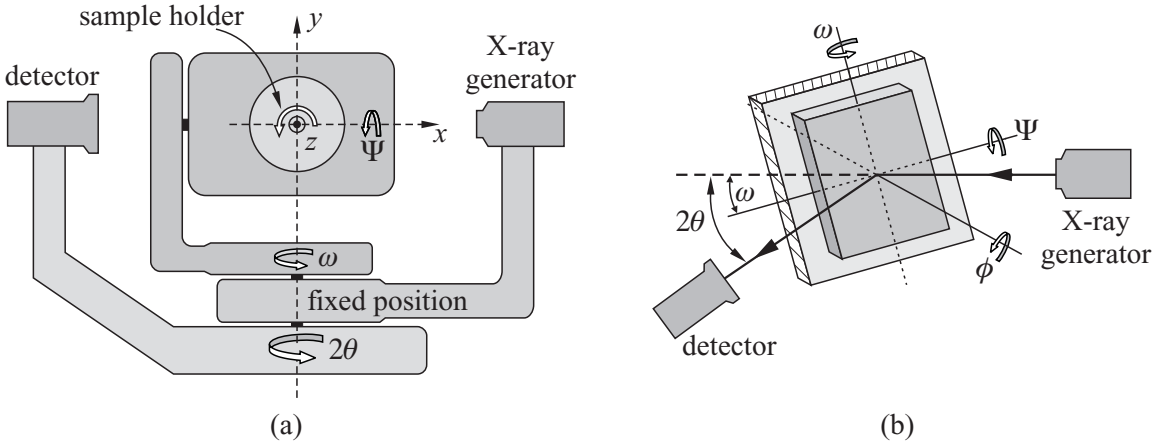

Figure 5.3: *(a) Schematic setup of the XRD aparatus, (b) angle definitions.*

If the sample is polycrystalline without preferred orientation, the X-ray diffraction maxima can be detected merely by moving the equipment to the necessary θ-2θ position. It should be noted that with these θ-2θ measurements it is only possible to observe the diffraction of planes which are parallel to the sample surface. If the sample is a single crystal or polycrystalline, but textured, then the maxima may be out of the plane defined by X-ray source, sample and detector. To examine the population of planes as a function of orientation, the direction of the lattice vector $\mathbf{G}$ has to be varied (see figure 5.2). These measurements are referred to as rocking scans or rocking curves because typically the sample is rocked through the angle ω on the diffractometer while the detector is held in a fixed position 2θ (see figure 5.3 (b), angle definitions). Then it is possible to observe planes which are not parallel to the sample surface.

5.1.2 500 nm Y_2O_3 Films

For optical applications it is advantageous to have films with perfectly orientated grains or crystallites, because disoriented grain boundaries may have a strong effect on the optical properties (scattering losses). Thus, one has to find the optimum growth conditions for crystalline film formation. To investigate the grade of crystallinity for different growth

conditions, XRD measurements have been performed on films grown at different substrate temperatures and oxygen pressures. As described in chapter 3, the film growth can be influenced by a variety of parameters, but these have been found to be the most important. The influence of the substrate temperature at a constant oxygen pressure of $p(O_2) = 5 \times 10^{-2}$ mbar on the structural behavior is presented in figure 5.4. For a 500 nm thick film grown from a sintered Y_2O_3 target at room temperature (20℃), no Y_2O_3 diffraction peaks are visible – the film is completely amorphous. In this spectrum (figure 5.4 (a)), only the (0006) reflection of the α-alumina substrate at 41.7° with a peak width of 0.1° (FWHM) can be seen. At a substrate temperature of 300℃ (figure 5.4 (b)), the yttria {222} reflection peak appears at 29.1° (a list of possible Y_2O_3 reflection peaks and the corresponding intensities in a powder sample can be found in appendix C). At 60.26°, a higher order of this reflection, the {444} peak, arise. Additionally, the {400}, the {440}, and the {622} reflection peaks can be seen. These peaks have less intensity than the {222} and {444} peaks, indicating a preferred growth of yttria in the ⟨111⟩ direction. This effect becomes stronger at a substrate temperature of 700℃ (figure 5.4 (c)). In this case, the {222} peak at 29.19° dominates the spectrum and is even stronger than the α-Al_2O_3 peak. The {400} peak is also visible, but nearly four orders of magnitude smaller. Neither the

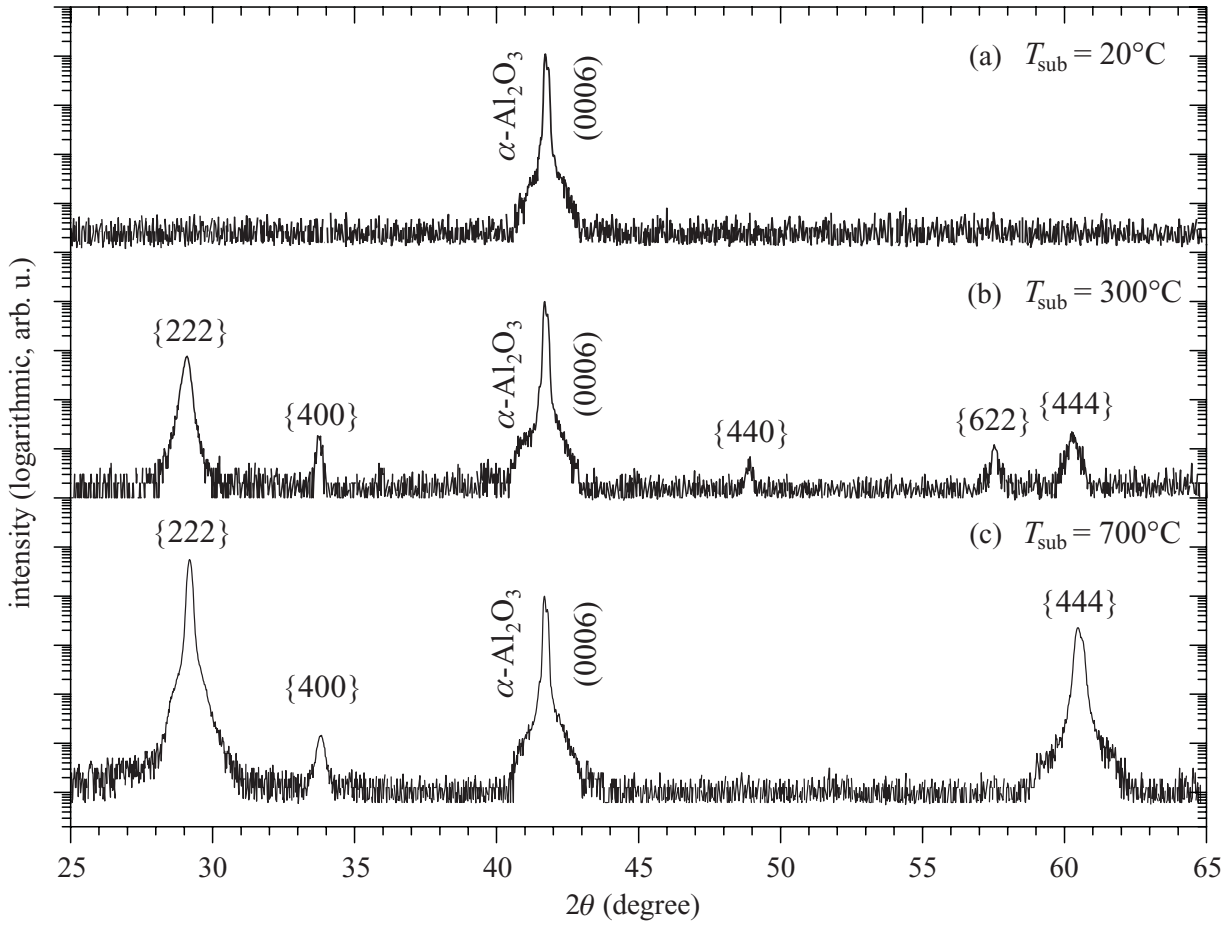

Figure 5.4: *X-ray diffraction patterns of yttria films grown at different substrate temperatures ($p = 0.05$ mbar).*

{440} peak nor the {622} peak can be observed in this spectrum. Their disappearance indicates an increase of the ⟨111⟩ texture in the polycrystalline film at higher substrate temperature. Also this film has to be termed polycrystalline because there is no evidence of laterally connected crystallites forming the film (in section 5.3 it is shown that the film growth starts with single islands).

From these measurements it can be seen that the 500 nm thick films grown at substrate temperatures > 300℃ are uniaxially textured along the ⟨111⟩ direction, because the X-ray diffraction patterns reveal mainly the {222} oriented diffraction line.

The same effect (preferred growth in ⟨111⟩ direction) is observed when the oxygen partial pressure is varied (4×10^{-3} mbar $\leq p \leq 5 \times 10^{-1}$ mbar) at constant temperature. The dependence of the crystallinity on the oxygen pressure is shown in figure 5.5. In this graph, the FWHM of the {222} reflection peak, which was the strongest in all cases, is shown as a function of the oxygen pressure. If the pressure increases from 4×10^{-3} mbar the FWHM decreases till it reaches a minimum of 0.163° at 5×10^{-2} mbar. Further increase of the pressure results in a strong increase of the FWHM. Additionally, it was observed that the {400} peak becomes stronger at higher oxygen content. Zhang et al. attributed the shift of the diffraction peak from ⟨111⟩ to ⟨100⟩ orientation with increasing O_2 gas pressure to a change in oxygen vacancies, which results in beneficial growth of Y_2O_3-films along ⟨100⟩ direction [Zha98].

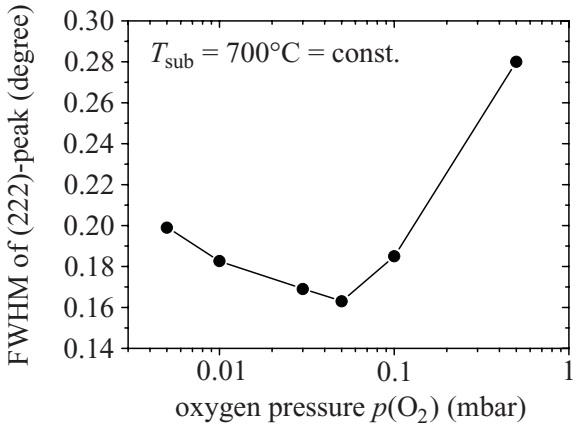

Figure 5.5: *FWHM of the Y_2O_3 (222) peak for films grown at different oxygen pressures.*

The observed preferred ⟨111⟩ orientation can be explained by a minimization of the surface free energy G, which is given by an extension of Young's equation 3.9, i. e.

$$G = (\gamma_f - \gamma_s) + \gamma_i - \gamma_e \,, \tag{5.7}$$

where γ_f, γ_s, and γ_i, and are the free surface energies of the film–air, the substrate–air, and the film–substrate interfaces, respectively. γ_e is the epitaxial energy gain. The film growth occurs in the orientation which minimizes G. In the cubic phase, the denser planes are the {111} ones, therefore, they have the lower surface free energy γ_f. If γ_f is the dominant term, the films tend to be ⟨111⟩ oriented. However, the substrate lattice can impose another orientation if there is a low lattice mismatch, as it is the case for yttrium-stabilized zirconia (YSZ) or $LaAlO_3$. The γ_e term becomes dominant then. In the case of amorphous substrates, e. g. amorphous SiO_2 [Pon02], there is no lattice mismatch influence, and the γ_e term is negligible, which explains the ⟨111⟩ orientation.

Using the Scherrer equation 5.5, the FWHM of 0.163° of the {222} peak presented in figure 5.4 (c) gives an out-of-plane diffracting domain size of $B_\perp = 130$ nm. The in-plane grain size at the surface was measured by AFM and is of the same order ($B \approx 140$ nm,

see section 5.3). Compared with other values available in the literature this is a large domain size indicating a relatively undistorted and well-ordered growth of the crystallites in the out-of-plane direction (e. g. Kim Anh et al. [Kim03] reported a 90 nm out-of-plane domain size in a 480 nm thick Y_2O_3 film grown by PLD).

In addition to the θ-2θ-scans, the out-of-plane orientation of the crystallites, corresponding to planes which are not parallel to the surface, was investigated by rocking-curve measurements (ω-scan). Using the optimum growth conditions, the $\langle 111 \rangle$ crystal axes of the 500 nm thick films are aligned along the film normal direction within 0.74° of FWHM (see figure 5.6). For comparison, the width of the substrate peak is 0.3°.

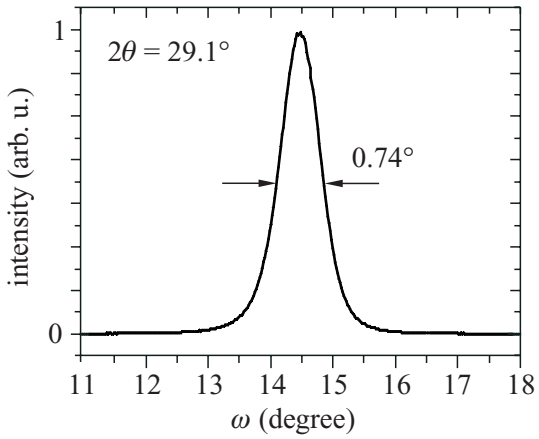

Figure 5.6: *Rocking curve of {222} reflection peak.*

As it can be seen from equation 5.3, the lattice constant a can be retrieved from the position of the diffraction lines. Lattice constants derived from the XRD measurements are labelled $a_\perp$ whereas lattice constants obtained by SXRD are labelled $a_\parallel$. In the following, $a_\perp$ was calculated only from the strong {222} peak position. For the films grown at $T_{\mathrm{sub}} = 300$℃ this results in a lattice constant of $a_\perp = 10.62$ Å. The deviation from the bulk value $a_{\mathrm{bulk}} = 10.603$ Å is explained by stress. Thus, a measure of the evolving strain in the film growth direction ($\varepsilon_\perp$) is given by

$$\varepsilon_\perp = \frac{a_\perp - a_{\mathrm{bulk}}}{a_{\mathrm{bulk}}} \; . \tag{5.8}$$

The influence of the substrate temperature on the lattice constant is comparably small. The resulting variations of $a_\perp$ in films grown at substrate temperature ≤ 500℃ indicate tensile stress of only $\varepsilon_\perp = 1.6 \times 10^{-3}$. The lattice constants of various yttria films grown at $T = 700$℃ ($100\,\mathrm{nm} \leq d_{\mathrm{film}} \leq 750\,\mathrm{nm}$) show only small deviations from the bulk value ($a_\perp = 10.602$ Å) resulting in an overall compressive strain of only $\varepsilon_\perp = -10^{-4}$.

In general, independent of the growth method, stresses are induced in the deposited films and their effects can be deleterious for the film properties. In particular, residual stress in yttria films could alter the optical properties and cause the appearance of birefringence, by deforming the unit cell. Pons-Y-Moll et al. [Pon02] observed that undoped and Er-doped films showed compressive stress of –1.8 GPa, while Eu-doped films have lower residual stress (–1.4 GPa). This effect is explained by the larger ion radius of europium, compensating part of the compressive stresses. Stress is not only induced by lattice mismatch or non-perfect substrate surface but also caused by the thermal behavior of the film–substrate system (thermal stress). This is due to the difference between the thermal expansion coefficient of the substrate α_{s} and that of the film α_{f} during cooling of the deposited film to room temperature. Knowing Young's modulus E_{f} and Poisson's ratio ν_{f} of the film, the thermally induced interfacial stress σ_{th} can be calculated by

$$\sigma_{\mathrm{th}} = [E_{\mathrm{f}}(\alpha_{\mathrm{f}} - \alpha_{\mathrm{s}})\Delta T]/(1 - \nu_{\mathrm{f}}) \; , \tag{5.9}$$

where ΔT is the difference between the substrate temperature during film growth (700°C) and the finally reached temperature (20°C). Using the values given in table 2.1, the thermal stress in the yttria–alumina system is 0.56 GPa. Reducing the growth temperature will result in reduced thermal stress, but also in films with a smaller degree of crystallinity. However, compared with stress induced by lattice mismatch, the thermal stress plays a minor role in sesquioxide film growth.

5.1.3 Thin Y_2O_3 Films

With decreasing film thickness, a change in the θ-2θ-scans becomes visible. Figure 5.7 shows the diffraction patterns of a 100 nm (a) and a 20 nm thick (b) yttria film. Both films were grown at a substrate temperature of 700°C and an oxygen pressure of 5×10^{-2} mbar. It can be seen that for a film thickness of 100 nm, the peak position of the {222} reflection ($2\theta = 29.14°$) is nearly identical to that of the bulk crystal resulting in a lattice constant of $a_\perp = 10.607$ Å. As a result of the lower film thickness, the peak width increased slightly (FWHM = 0.193°) giving an out-of-plane grain size of ~ 90 nm, which is nearly the film thickness.

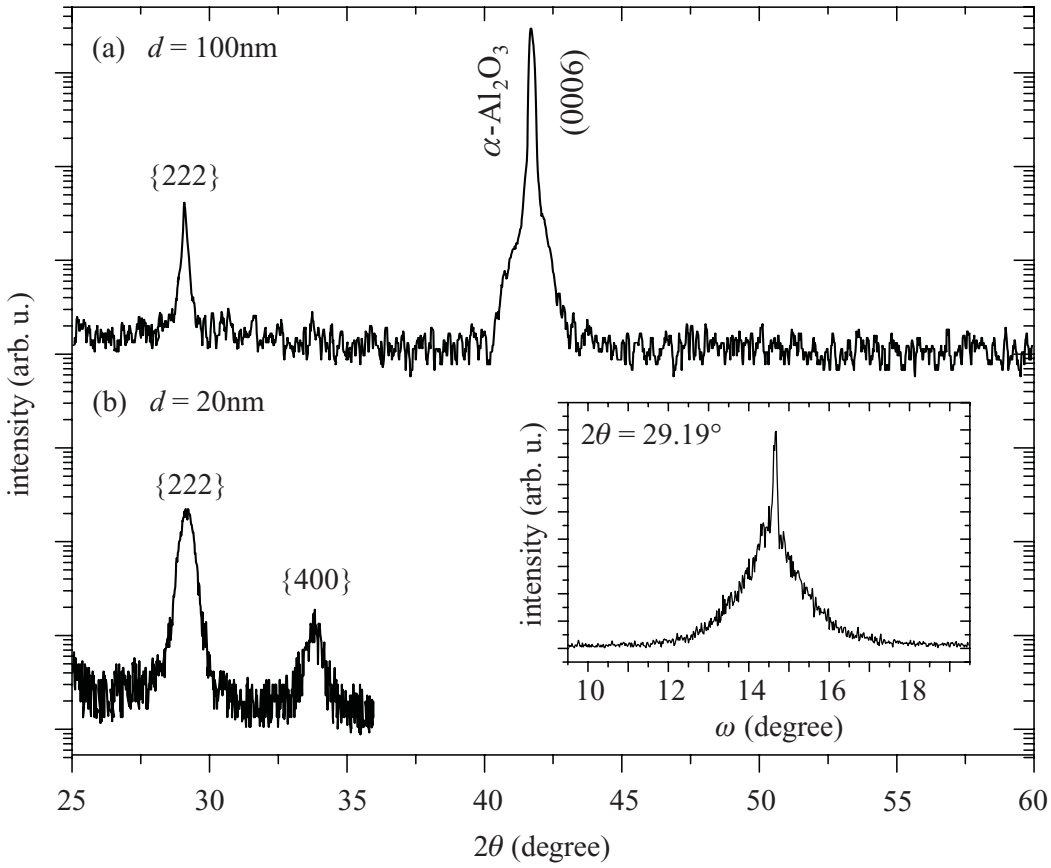

Figure 5.7: *X-ray diffraction patterns of thin yttria films grown on α-Al_2O_3 at 700°C: (a) 100 nm thickness and (b) 20 nm thickness. Inset: rocking curve of 20 nm film.*

In the case of the Y_2O_3 film with 20 nm thickness, the situation changes. The {222} diffraction peak appears at $2\theta = 29.19°$ with a FWHM of 0.57°. The corresponding out-of-plane lattice constant is smaller than the bulk value ($a_\perp = 10.59$ Å) indicating compressive stress in the growth direction ($\varepsilon_\perp = -1.2 \times 10^{-3}$). Interestingly, this film shows also compressive stress in the in-plane direction (see results of SXRD, p. 60). Additionally, in this diffraction pattern, the {400} peak appears at 33.84° (FWHM = 1.03°). The {222} rocking curve of the 20 nm thick film is also presented in the inset of figure 5.7. In this case, the crystallites are not as perfectly aligned with respect to the substrate surface as in the 500 nm thick films.

5.1.4 Surface X-ray Diffraction

As shown in the previous section, the geometrical structure of materials can be investigated easily by X-ray diffraction. To study the surface and near surface regions in more detail, a modification of the conventional setup, called surface X-ray diffraction (SXRD), is used. The advantage over electron diffraction is the penetration depth of the radiation, which is scalable over a wide range. Thus, buried layers and systems of different layers can be investigated. In contrast to XRD, where only information about planes parallel to the surface is obtained, the method of SXRD results in diffraction patterns of planes which are perpendicular to the surface [Kum98].

In general, for X-rays the real part of the refractive index of matter is smaller than 1. As a consequence, the direction of propagation of the transmitted (refracted) wave makes an angle with the surface which is smaller than the angle between the incident ray and the surface ($\alpha_t < \alpha_i$). This is in contrast to visible radiation. At a certain angle of incidence α_i, termed critical angle α_c, α_t is 0. This effect is called total reflection. For angles smaller than α_c, the incoming wave is totally reflected. In this case, the wave will penetrate into the crystal only in a very thin, near-surface region (evanescent wave), where its propagation direction is parallel to the surface (see figure 5.8). Due to this propagation direction, only planes perpendicular to the surface are detected. By varying the penetration depth of the evanescent wave, which depends only on the angle of incidence α_i, the refractive index n, and the wavelength of the X-ray radiation λ, the surface sensitivity in SXRD is regulated easily. Figure 5.9 shows the dependence of the penetration depth (or attenuation length) l_i on the angle of incidence α_i for radiation with a wavelength of $\lambda = 1.24\,\text{Å}$ in Y_2O_3.

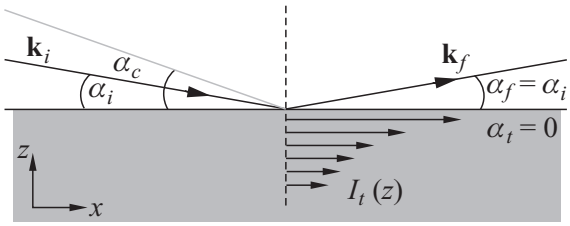

Figure 5.8: *Diffraction of X-rays at a vacuum–crystal-interface for $\alpha_i < \alpha_c$.*

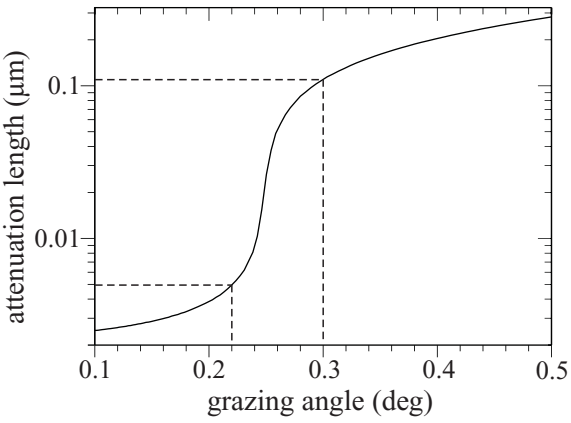

Figure 5.9: *Calculated attenuation length of 10 keV radiation in Y_2O_3.*

Surface Coordinates

The coordinate system used in crystallography of bulk crystals is not well suited for the description of surfaces. In order to find proper surface coordinates, the notation of the LEED method (Low Energy Electron Diffraction) has been used successfully in SXRD. A general approach to LEED notation can be found in the literature [DeC96, Van86].

Here, only the surface coordinates of cubic Y_2O_3 in $\langle 111 \rangle$ growth direction are presented. In this case, the $\{111\}$ planes should be parallel to the substrate surface, and thus, the magnitude of the lattice vectors of yttria can be re-defined as

$$|\mathbf{a}| = |\mathbf{b}| = \tfrac{1}{2}\sqrt{2}a_{\text{bulk}} \qquad \text{and} \qquad |\mathbf{c}| = \tfrac{1}{3}\sqrt{3}a_{\text{bulk}} \,, \tag{5.10}$$

where a_{bulk} denotes the conventional lattice constant. The angle between $\mathbf{a}$ and $\mathbf{c}$ as well as the angle between $\mathbf{b}$ and $\mathbf{c}$ is 90° each, while the angle between $\mathbf{a}$ and $\mathbf{b}$ is 120°. Using these surface vectors the corresponding reciprocal lattice vectors[2] are

$$|\mathbf{a}^*| = |\mathbf{b}^*| = \frac{8\pi}{\sqrt{6}\, a_{\text{bulk}}} \qquad \text{and} \qquad |\mathbf{c}^*| = \frac{6\pi}{\sqrt{3}\, a_{\text{bulk}}} \,, \tag{5.11}$$

with an angle of 60° between $\mathbf{a}^*$ and $\mathbf{b}^*$, while the angle of $\mathbf{a}^*$ and $\mathbf{b}^*$ with $\mathbf{c}^*$ is 90° each (see figure 5.10 (a). As described above, only planes perpendicular to the surface are detected using SXRD. In case of $\langle 111 \rangle$ grown yttria on sapphire one can find planes perpendicular to the $\{111\}$ planes. This condition is fulfilled for $\{110\}$ planes, if $\{111\} \cdot \{110\} = 0$. In practice, the $\{440\}$ plane was detected as this plane offers the highest relative intensity (see appendix C). The experiments have been performed with synchrotron radiation at beamline BW2 at HASYLAB (DESY). This setup is described in [Bun99]. The principle scheme of SXRD is shown in figure 5.10 (b). It can be seen that, in contrast to XRD, in SXRD the 2θ angle lies in the surface plane. The wavelength of the X-rays was 1.24 Å corresponding to an energy of 10 keV. The angle of incidence with respect to the surface was varied between 0.2° and 0.3° depending on the thickness of the films.

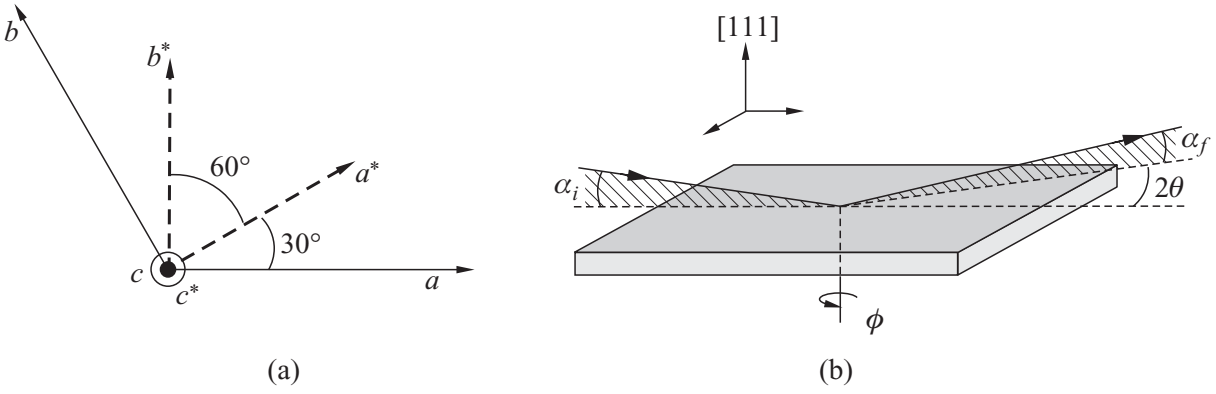

Figure 5.10: *(a) Surface coordinates of (111) Y_2O_3, (b) Principle of surface X-ray diffraction.*

[2]The reciprocal lattice vector is defined as $\mathbf{a}^* = 2\pi(\mathbf{b} \times \mathbf{c})/V$, where V is the volume of the elementary cell $V = \mathbf{a} \cdot (\mathbf{b} \times \mathbf{c})$. The calculation of the reciprocal lattice vectors $\mathbf{b}^*$ and $\mathbf{c}^*$ is carried out by cyclic permutation of the vectors.

SXRD Results of 20 nm and 100 nm Yttria Films

In figure 5.12 (a) a θ-2θ scan of an yttria film with a thickness of 20 nm is shown. The spectrum is dominated by a peak at $2\theta = 38.96°$ with a FWHM linewidth of $\Delta 2\theta = 1.43°$. For comparison, in additional experiments the FWHM of the sapphire peak at 52.46° has been determined to be 0.6°. Since the diffraction angles θ of different X-ray wavelengths λ are related by

$$\sin\theta_{\mathrm{XRD}} = \frac{\lambda_{\mathrm{XRD}}}{\lambda_{\mathrm{SXRD}}} \sin\theta_{\mathrm{SXRD}} \ ,$$

this peak can be assigned to diffraction at {440} planes (the subscripts 'XRD' and 'SXRD' indicate the diffraction angles and wavelengths used in conventional X-ray diffraction and surface XRD, respectively). The recalculation of the experimental 2θ diffraction angle of Cu-Kα_1 radiation results in $2\theta = 48.95°$, which is slightly smaller than the theoretical bulk value of $2\theta = 48.55°$. Using equation 5.3 the lattice constant of yttria parallel to the surface in the 20 nm thick film is calculated to $a_{\parallel} = 10.51\,\text{Å}$, which is considerably smaller than the bulk value of $a_{\mathrm{bulk}} = 10.603\,\text{Å}$. Compared with the lattice constant $a_{\perp} = 10.59\,\text{Å}$ obtained by conventional XRD it can be seen that the unit cell of yttria is strongly distorted, i. e. compressed, in both directions indicating strain due to the lattice mismatch.

The assignment of the reflection peaks between 20° and 30° was not straight forward because one has to take into account that at the interface not only Y_2O_3 but also $Y_3Al_5O_{12}$ and $YAlO_3$ can exist due to subplantation effects (see section 5.4, p. 80 f and p. 84 f). Each these three structures has various diffraction lines in this 2θ range.

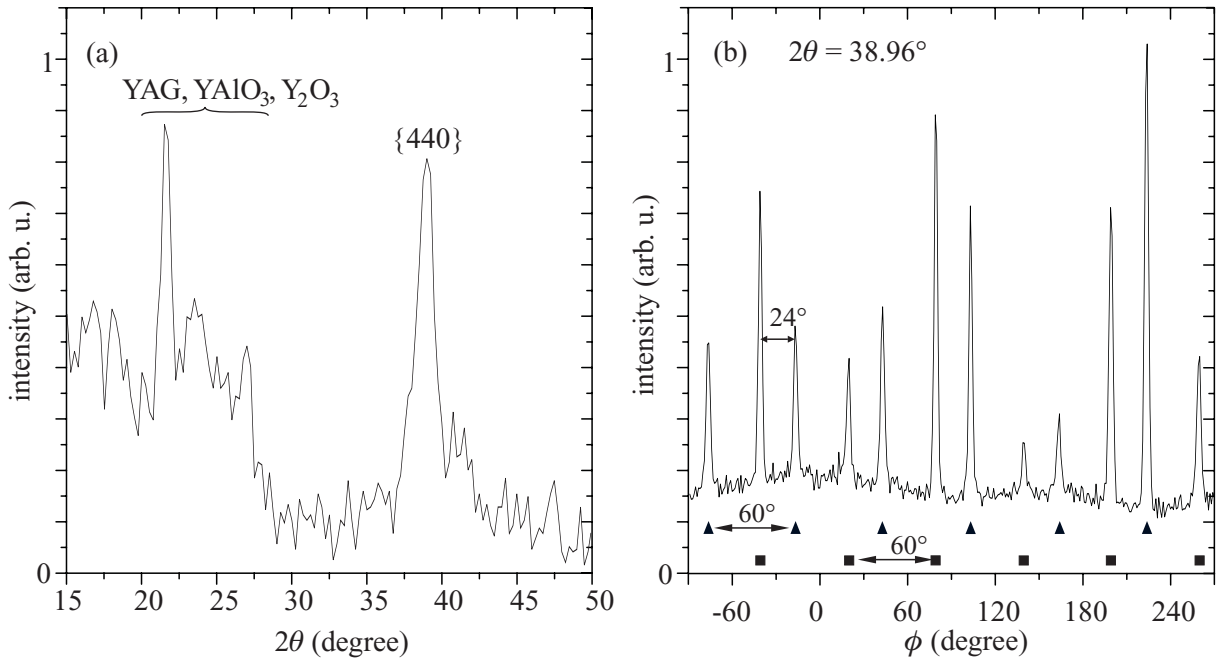

Figure 5.11: *SXRD of 20 nm Y_2O_3 film: (a) 2θ-scan, (b) φ-scan*

The ϕ-scan of the 20 nm thick film shows two sets of 6 peaks which are separated by 24°. The distance between each of the six peaks in a set is 60°. This sixfold symmetry is again an indication of the $\langle 111 \rangle$ growth of yttria as there are three $\{110\}$ planes separated by 120° perpendicular to $\{111\}$. Each $\{110\}$ plane results in two reflection peaks separated by 180°. The two sets of peaks represent two domains grown in $\langle 111 \rangle$ direction but rotated by 24° against each other. The appearance of two different domains with the same growth direction is commonly known as *twinning*. An explanation for twinning are the positions of the atoms in the yttria matrix, which form a slightly distorted cube. Thus, the atoms forming the $\{111\}$ planes do not create an equal-sided triangle. Due to the distortion, two of the angles in the triangle are $\approx 58°$ instead of 60°. However, this angle deviation is not sufficient enough to explain the large rotation by 24°. However, due to subplantation effects the substrate surface is not pure Al_2O_3, but also consists of YAG and $YAlO_3$ components. Since YAG is a cubic system with a lattice constant of $a_{YAG} = 11.93\,\text{Å}$, the continuous growth of cubic Y_2O_3 along the $\langle 111 \rangle$ direction can occur. The fact that very sharp diffraction peaks appear in the ϕ-scan is an indication of the homogeneous orientation of the $\langle 111 \rangle$ grown crystallites.

The same measurements have been performed on a 100 nm thick yttria film. The θ-2θ scan of this film presented in figure 5.12 shows again the dominating $\{440\}$ peak at $2\theta = 38.4°$ with a FWHM peak width of $\Delta 2\theta = 1.14°$. The corresponding 2θ-position for Cu-Kα_1-radiation is 48.55°, which results in a lattice constant of $a_{\parallel} = 10.63\,\text{Å}$ ($a_{\perp} = 10.607\,\text{Å}$). In this case, the unit cell of yttria is stretched to obtain lattice matching with the substrate ($\varepsilon_{\parallel} = 2.5 \times 10^{-3}$). In addition to the $\{440\}$ peak, three additional yttria peaks can be seen in the θ-2θ scan: $\{222\}$ at 23.4°, $\{400\}$ at 27° and $\{622\}$ at 45.6°. The diffraction

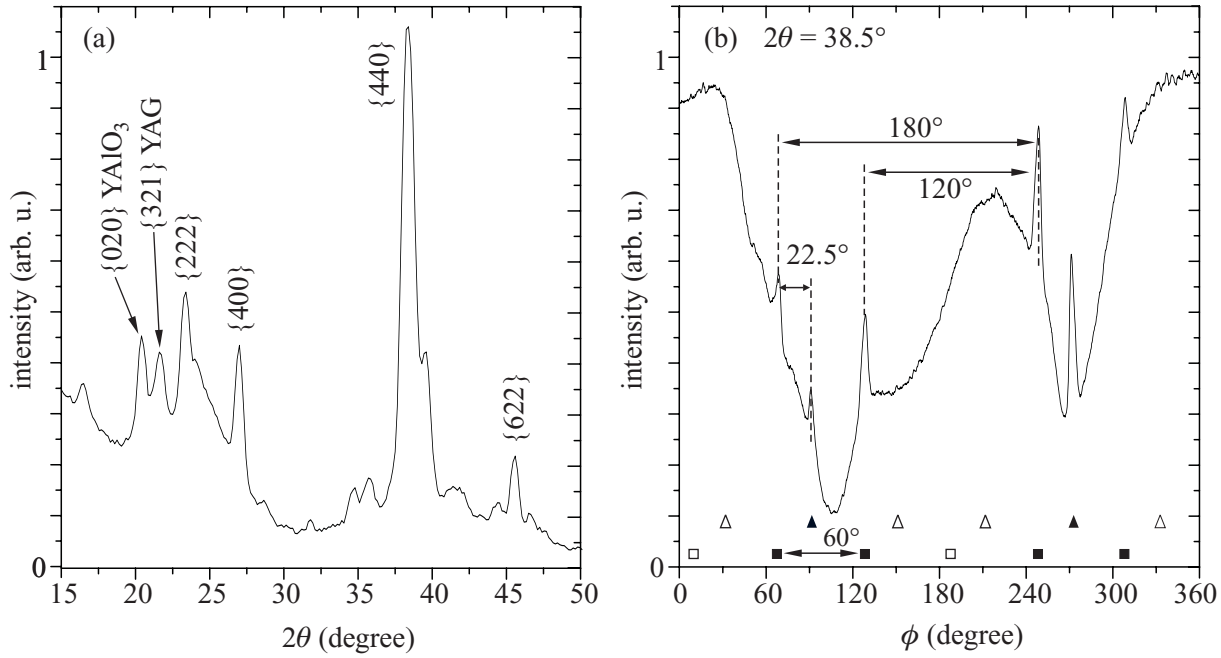

Figure 5.12: *SXRD of 100 nm Y_2O_3 film: (a) 2θ-scan, (b) φ-scan.*

peaks at 20.4° and 21.6° can be assigned to the crystal structures of $YAlO_3$ and $Y_3Al_5O_{12}$. From the relative intensities of the different peaks it can be seen that the film is textured along the ⟨111⟩ direction of cubic Y_2O_3, but has a polycrystalline component.

To obtain more information about the orientation of the ⟨110⟩ grown crystallites, the sample was rotated by 360° at a fixed 2θ angle of 38.4° (ϕ-scan). The result is shown in figure **??** (b). In addition to six sharp peaks, a large oscillation in the diffracted intensity can be seen. This is very likely an effect of the rectangular sample geometry ($5 \times 10\,\mathrm{mm}^2$), in contrast to the 20 nm thick film where a square sample was used.

It is not yet clear why six of the 12 peaks observed in the 20 nm thick film vanish (the missing ones are indicated by hollow symbols in figure 5.12). Probably, the strong background oscillation superimposes the weak diffraction peaks and only the strongest are visible. However, it can be seen that the domain of ⟨110⟩ crystallites indicated by (■) is grown out with increasing film thickness and dominates the 100 nm thick film, as this domain is represented by four peaks compared to the two peaks of the (▲) domain.

Discussion of the XRD and SXRD results

It was shown that the Y_2O_3-films grown on α-alumina at a substrate temperature of 700℃ and at an ambient oxygen pressure of 5×10^{-2} mbar are highly textured along the ⟨111⟩ direction. However, the films are not uniaxially textured, but show polycrystalline components. Additionally, at thin films a twinning of the ⟨111⟩ grown crystallites was observed. The non-perfect film growth has various reasons [Ars80]:

1. defects due to imperfections on the substrate (e. g. dislocations, strain),
2. defects due to different lattice constants,
3. defects created by the formation of different phases,
4. defects due to varying growth conditions,
5. surface defects on the grown film,
6. defects due to the incorporation of impurities or the irregular distribution of the components or the dopants of the growing film and
7. defects due to thermally induced stress.

The most important point is the difference in lattice constants. For this reason, films of Lu_2O_3, Sc_2O_3, and $YScO_3$ have been grown. These materials show reduced lattice mismatch with the alumina substrate, which should result in a more favorable growth along the ⟨111⟩ direction. First X-ray measurements on the lutetia and scandia films seem to justify these assumptions, as in the corresponding diffraction patterns only the {222} and {444} peaks occur. As demonstrated by L. Rabisch [Rab03], films of $LuScO_3$ on α-alumina prepared by electron beam evaporation show only sharp {222} and {444}

reflection peaks in the diffraction pattern. The FWHM width of these peaks is smaller than in comparable Y_2O_3 or Lu_2O_3 films indicating better lattice matching with the substrate (as predicted in section 3.3) and, thus, leading to a more epitaxial growth behavior.

Another parameter which might lead to imperfections is the target–substrate distance during the deposition, i. e. the particle energy at the substrate surface. High energy particles can be subplanted into the alumina matrix resulting in a new crystalline matrix. For example, the reaction $3 \times Y_2O_3 + 5 \times Al_2O_3 \rightarrow 2 \times Y_3Al_5O_{12}$ can take place, and the resulting structure of YAG offers a different lattice constant than alumina: the desired condition of lattice matching is not fulfilled. This behavior was proven on the one hand by the SXRD measurements, and on the other hand by the optical spectroscopy presented in section 5.4, clearly identifying the band edge of $Y_3Al_5O_{12}$.

5.2 Rutherford Backscattering

Rutherford backscattering analysis (RBS) is based on collisions between atomic nuclei. The sample is bombarded with a monoenergetic beam of highly energetic charged particles, typically helium ions, and the number and energy of ions which scatter backwards after colliding with heavier atoms in the near-surface region of the sample is measured (see figure 5.13). With this information, it is possible to determine atomic masses and elemental concentrations versus depth below the surface [Gos87a, Gos87b].

The vast majority of high-energy probing particles are implanted into the material and do not escape. Only a small fraction of the incident particles undergo a direct collision with a nucleus of one of the atoms and are backscattered out of the sample.

The energy measured for a particle backscattered at a given angle depends on two processes: The loss of energy experienced by the particles while they pass through the sample, both before and after a collision, and the loss of energy as a result of the collision itself (transfer of momentum to the target atom).

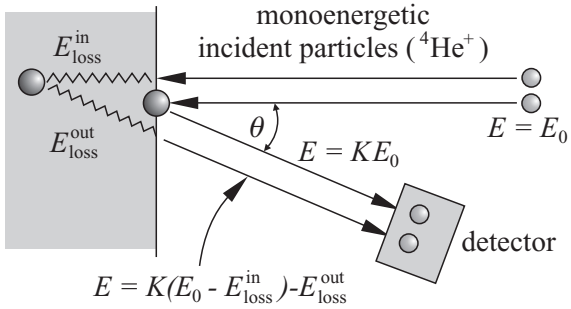

Figure 5.13: *Energy loss processes for backscattering.*

When the probing particles penetrate to some depth into a dense medium, the projectile energy dissipates due to interactions with electrons (electronic stopping) and to glancing collisions with the nuclei of target atoms (nuclear stopping). Thus, a particle which backscatters from an element at some depth in a sample will have measurably less energy than a particle which backscatters from the same element at the sample surface. The amount of energy a projectile loses per distance traversed in a sample depends on the projectiles mass, its velocity, the elements in the sample, and the density of the sample material.

The ratio of the projectile energy after a collision to the projectile energy before a collision is defined as the kinematic factor:

$$K = \frac{E_{\text{scattered}}}{E_{\text{incident}}} = \left[\frac{\sqrt{1 - \left(\frac{M_1 \sin\theta}{M_2}\right)^2} + \frac{M_1 \cos\theta}{M_2}}{1 + \frac{M_1}{M_2}} \right]^2 , \tag{5.12}$$

where E is the ion energy, M_1 is the mass of the incident ions and M_2 is the mass of the target atoms. θ is defined as the angle between the trajectory of the particles before and after scattering (see figure 5.13).

The number of backscattering events that occur from a given element in a sample depends mainly on two factors: the concentration of the element and the effective size of its nucleus. The probability for a collision to occur is called scattering cross section. The scattering cross section is proportional to the square of the atomic number of the target atom.

Using a multi-channel analyzer, the signal from the detector can be converted into a histogram of particle energies. A simplified drawing of a typical RBS-spectrum is shown in figure 5.14, where M_1 is the mass of the probing particles, and M_2 and M_3 represent the masses of two different types of atoms in the thin film ($M_1 \ll M_2 < M_3$). The particles repelled by the heavier dopants M_3 have higher energies and appear at a higher channel number than the lighter particles. The energies of the backscattered particles depend also on their position relative to the surface. For example, the width of the 'plateau' in the peak for the dopant M_3 in gives an indication of the depth to which these elements have penetrated. The yield for the different elements present in the film measured at the surface can be used to calculate the stoichiometry of the surface layer. The determination of the overall stoichiometry, e. g. stoichiometry below the surface, requires a more complex analysis which is retrieved by computer modelling.

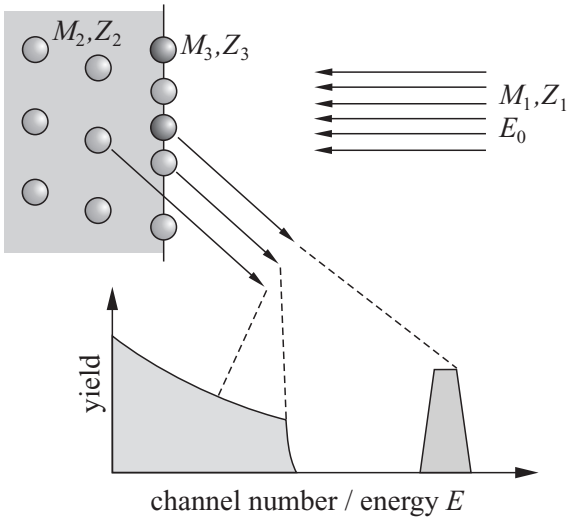

Figure 5.14: *Simplified RBS spectrum showing the energy distribution of the backscattered particles.*

5.2.1 Channeling

In addition, RBS can also be used to study the structure of single crystal samples [Fel86]. This variation of the typical RBS measurement is called *channelling* technique. The channeling effect occurs when the incident beam is aligned with a major crystallographic axis of a single crystal target. In this case the scattering probabilities are modified compared with a non-crystalline material. Thus, the difference between an aligned (orientated) and an unaligned (random) spectrum provides information about degree of disorder in the crystal. If a channeling effect could be observed in thin films it is an indication of epitaxial growth behavior between the substrate and the growing film. This can be explained by the fact, that for significant channeling not only the film has to be single crystalline but also the rows of atoms of the substrate must be aligned in the same direction, e. g. epitaxial film growth is achieved.

5.2.2 Experimental

To determine the composition of the films Rutherford backscattering experiments have been performed at the Departamento de Física Aplicada, Universidad Autonoma de Madrid, Spain. In this case, a 2 MeV $^4He^+$ beam with a spot size of $1 \times 1\,mm^2$ has been used to bombard the samples, which were held under vacuum ($p = 5 \times 10^{-7}$ mbar). The backscattered particles have been detected at an angle $\theta_{RBS} = 171°$ with a PIPS detector (Passivated Implanted Planar Silicon detector). From this measurement, it could be

shown that the sesquioxide films have the correct stoichiometric composition and contain no impurities.

As an example, figure 5.15 shows the RBS spectrum of an Eu:Y_2O_3 film with a thickness of 500 nm grown at $T_{sub} = 700$℃ and $p(O_2) = 5 \times 10^{-2}$ mbar. The dashed line (b) indicates a simulation of the system Eu(1.5%):Y_2O_3 (500 nm) / Al_2O_3, and the positions of the different elements are marked. Although both compositions have the same cation–anion ratio of 2:3, one can distinguish the O content in the substrate and the O content in the film due to the different O concentration in the alumina substrate in a depth of 500 nm. This behavior is related to the higher density of cation sites in Y_2O_3 compared to Al_2O_3. The result of the randomly orientated film, i. e. no specific sample alignment with respect to the incident H^+-beam, is presented by the solid line (a). Both curves, the simulation and the measurement, fit very well for channel numbers > 30 indicating the correct stoichiometry as well as the correct film thickness.

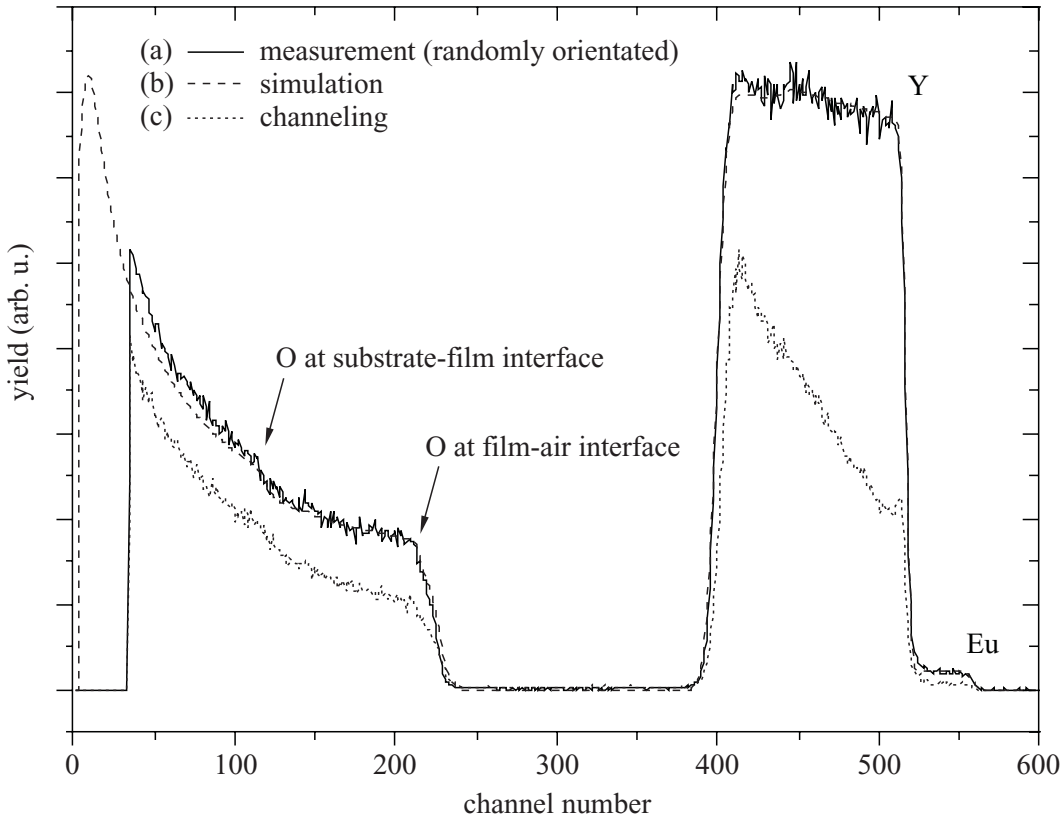

Figure 5.15: *RBS spectrum of a 500 nm Eu(1.5%):Y_2O_3 film on alumina.*

Additionally, at optimum growth conditions, a channelling effect was observed (c), i. e. an increase of Y-yield at lower energies. This channeling effect can be explained by a highly textured growth of Y_2O_3 along the ⟨111⟩ direction as well as epitaxial growth of the Y_2O_3 film along the ⟨111⟩-direction on the [0001] sapphire substrate (see fig. 5.15). The yield increases at lower energies because of the so called de-channelling effect. The de-channeling appears, because the incoming H^+-ions suffer from small-angle scattering from atoms, which are positioned at random positions inside the 'channels' of a certain

crystallographic direction. This de-channeling occurs because the crystal and thus, the channels are not perfect. The deeper the ions penetrate into the crystal the less distinct are the channels, and they do not have the precise direction necessary to see the channeling effect, hence the yield increases. Epitaxial growth means that lattice matching between the substrate and the Y_2O_3 film can be achieved. This is an important result for possible waveguide applications because dislocations and defects at the interface are minimized. A similar effect was described by Cho et al. [Cho99], who observed a channeling effect in the system Y_2O_3 (111) / Si (111).

The stoichiometry of the yttria films remains constant over a wide range of oxygen pressures. For $p(O_2) > 0.1$ mbar, a negative influence of the higher oxygen concentration in the atmosphere during film growth on the composition of the films can be observed, e. g. for a film grown at an oxygen pressure of 0.5 mbar, the stoichiometry changed from Y_2O_3 to $Y_2O_{3.5}$. For conservation of charge, the additional oxygen is incorporated as neutral atoms in interstices of the Y_2O_3-matrix. However, this change of composition has no influence on the optical properties of the Eu-doped films (see section 5.4). In contrast, the substrate temperature has no influence on the film composition, but strongly affects the luminescence behavior. Due to reduced crystalline growth at lower temperatures, there is no long-range order in the matrix surrounding the Eu-ions resulting in inhomogeneous broadening of absorption and emission lines.

Compositional RBS experiments on Lu_2O_3-films have shown that after growth at a substrate temperature of 700℃ and an oxygen pressure of 0.5 mbar, the films have the correct stoichiometry. In addition, also in the Lu_2O_3 a channeling effect can be observed.

Thus, it can be concluded that for all types of sesquioxides, RE_2O_3 and $RE^{(1)}RE^{(2)}O_3$, the material transfer from the target to the substrate via the plasma results in a conservation of stoichiometry. Moreover, the fabrication of sesquioxide films on α-alumina substrates by PLD results in crystalline and epitaxial film growth as indicated by the observed channeling effect.

5.3 Atomic Force Microscopy

To characterize the surface of the films the technique of atomic force microscopy (AFM) has been used. In atomic force microscopy, a probe consisting of a sharp tip (radius of the order of 10 nm), integrated onto the end of a cantilever, is raster scanned across the sample surface using piezoelectric scanners to measure attractive or repulsive forces between the tip and the sample [Bin86]. Thus, the topography and several physical and chemical properties can be mapped in direct space with high lateral and vertical resolution (in the nm-range).

In practice, three imaging modes can be used to produce topographic images of sample surfaces: contact mode (ionic repulsion forces), non-contact mode (Van der Waals, electrostatic, magnetic or capillary forces), and tapping mode. In each modes the tip–sample force interaction leads to a bending of the cantilever. This bending as well as torsional deflections of the cantilever, due to lateral forces acting between tip and sample, are detected by applying the light pointer principle, in which a laser beam is reflected off of the cantilever and onto a segmented photodiode (see figure 5.16).

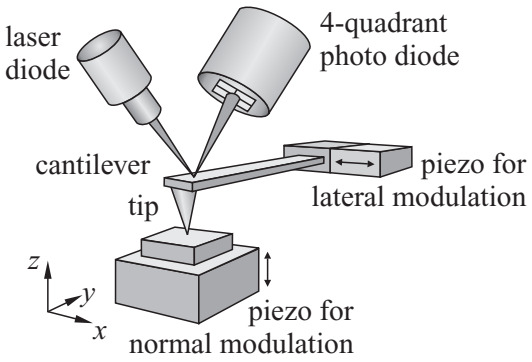

Figure 5.16: *AFM setup.*

During scanning, a particular operating parameter, e. g. the force between tip and sample surface, is maintained at a constant level, and images are generated through a feedback loop between the optical detection system and the piezoelectric scanners. In contact mode, the mode of operation used for the samples described in this work, the probe is essentially dragged across the sample surface maintaining a constant bend in the cantilever. As the topography of the sample changes, the z-scanner must move the relative position of the sample with respect to the tip to maintain this constant deflection. Using the feedback mechanism, the topography of the sample is mapped during scanning by assuming that the motion of the z-scanner directly corresponds to the sample topography. It is also possible to sense the local mechanical properties of the sample surface (resistance to deformations or frictional forces acting between tip and surface) when operating in contact mode.

For some applications it is not only useful to have an image of the surface topography but also to have a characteristic parameter of the surface roughness. In general, this is the root-mean-square roughness R_{RMS} [DIN78], which can be determined from discrete points of the measured surface topography $z(x_k, y_l)$, i. e.

$$R_{\mathrm{RMS}} := \sqrt{\frac{1}{N_x N_y} \sum_{k=1}^{N_x} \sum_{l=1}^{N_y} |z(x_k, y_l) - \bar{z}|^2} \,. \tag{5.13}$$

In this equation N_x and N_y are the discrete numbers of data points in x- and y-direction, respectively, which are identified by the different indices k and l. The value $\bar{z}$ describes a levelled plane with the smallest deviations from the data points (least squares fit) [Bra92].

All measurements have been performed in contact mode, which allows a very sensitive regulation of the tip-surface distance. Additionally, the local mechanical properties of the surface can be retrieved. The microscope used was a modified model of the EXPLORER series from TOPOMETRIX at the Bundesanstalt für Materialforschung und -prüfung (Berlin, Germany).

500 nm Yttria Films

Figure 5.17 shows an AFM-image of an uncoated alumina substrate. In addition to some ring-shaped structures, which are traces of the acetone used for cleaning, the surface is perfectly smooth with an RMS-roughness < 0.4 nm. This result is in good agrement with the specifications of the supplier.

The surface of an amorphous yttria film with a thickness of 500 nm grown at room temperature on alumina is shown in figure 5.18. Due to the low substrate temperature, no crystalline structure is visible, but a grain structure with an in-plane size of 40 nm to 60 nm and an average height of 5 nm. This morphology is homogeneous over the whole film surface. The RMS-roughness taken from a surface area of 2.24 µm × 2.24 µm is only 1.7 nm. In general, amorphous films are characterized by a smooth surface and thus, a small roughness.

In contrast to an amorphous film, figure 5.19 shows the surface morphology of a 500 nm thick crystalline yttria film. The triangular (2D) or pyramidal (3D) shaped crystallite structure observed is a signature of the crystallographic cubic-fluorite structure of bulk

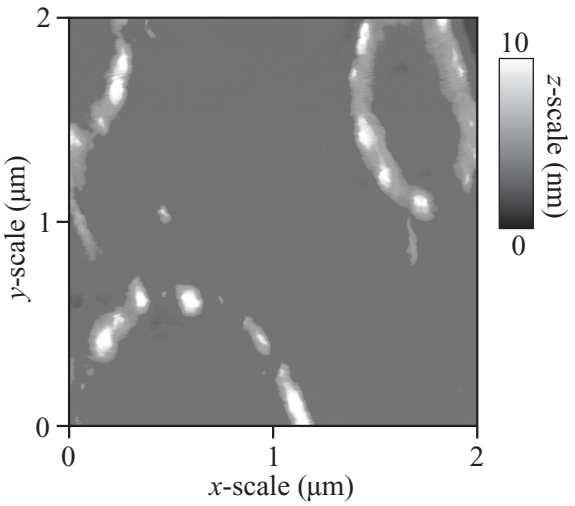

Figure 5.17: *Surface of an uncoated alumina substrate.*

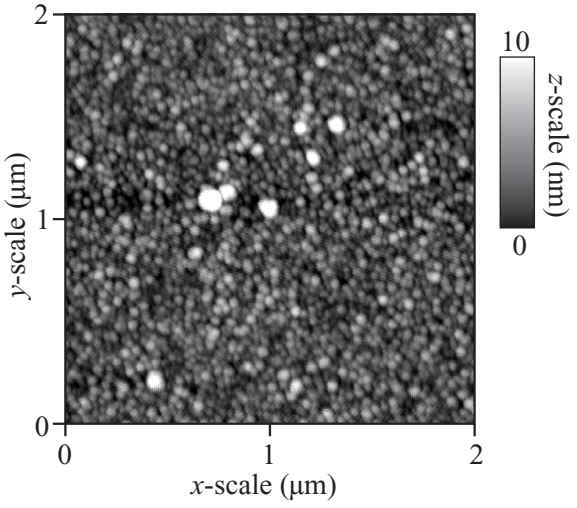

Figure 5.18: *Surface of an amorphous Y_2O_3-film (thickness 500 nm).*

Y_2O_3 and can be assigned to the ⟨111⟩ growth direction. The crystallites have edge lengths of the order of 120 nm – 160 nm. A surface morphology with pyramidally shaped grains was also observed by [Cho97] and [Kor99], but their structure was not as distinct as the picture presented here.

A similar structure is observed at the cleavage of a ⟨111⟩ grown Y_2O_3 bulk crystal. Figure 5.19 shows a picture of such a cleavage taken by an optical light microscope [Mix99]. A confirmation of the ⟨111⟩ growth direction is given by scanning electron microscopy (SEM) pictures of an etched {111} sulphur surface showing the same triangular structure [Pet81]. This leads to the conjecture that the ⟨111⟩ growth direction is connected with a pyramidal structure of the crystallites. Together with the results of X-ray diffraction and Rutherford backscattering, it can be concluded that film surface presented in the left picture of figure 5.19 shows a {111} plane of yttria.

In contrast to the cleavage structure in the bulk crystal, the film surface shows distorted triangles which are not parallel to the surface, but show a small angle with the substrate. This effect can be explained by the lattice mismatch between the grown yttria film and the corundum substrate. It should be noted that not all investigated Y_2O_3-films show this triangular surface pattern, but also surface structures similar to those of Sc_2O_3-films (see figure 5.21).

Compared with the amorphous film, the RMS-roughness of the crystalline film increased slightly to 2.4 nm. In general, the roughness of thick films, amorphous as well as crystalline, is comparably small, which clearly shows that these films can have optical quality and thus, are suitable for waveguide devices or optical coatings.

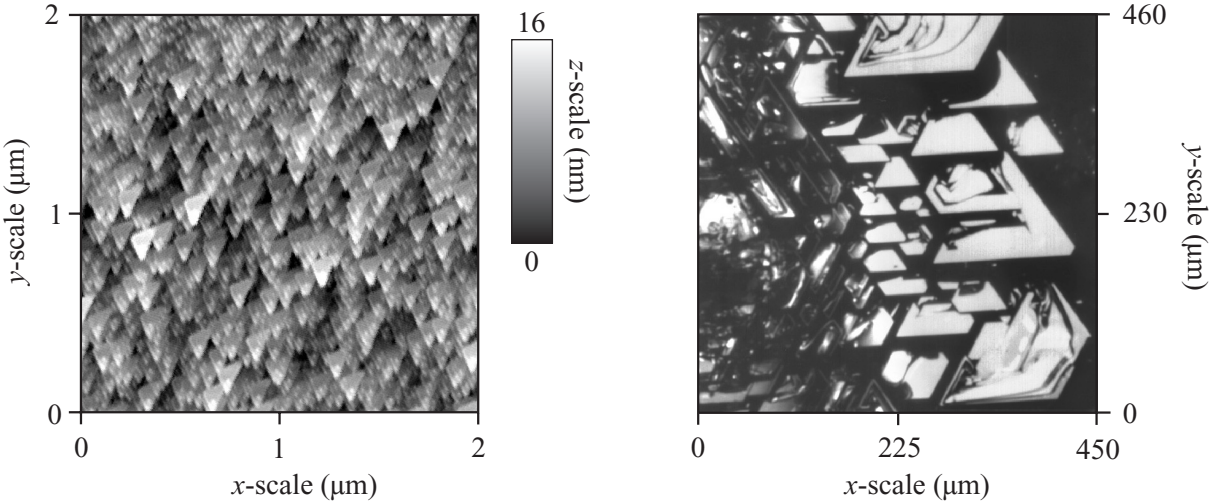

Figure 5.19: *Surface of a 500 nm thick crystalline yttria film (left), {111}-cleavage of an yttria bulk crystal (right).*

5 nm Yttria Film

In figure 5.20, the surface of a 5 nm thick yttria film is presented. It can be seen that at this early stage of film growth, there is no complete film covering the substrate surface. Instead, three dimensional island growth of small crystallites occurs. The size of the crystallites can also be seen in figure 5.20. The in-plane dimensions are between 50 nm and 200 nm, whereas the height ranges from 15 nm to 25 nm. 3D-island growth of yttria on α-alumina was already observed by [Kor00]. An interesting, however, until now not observed feature can be seen in the shape of the grains. Most of the edges of the crystallites have a 60°/120° angle, which is, together with the AFM result of a 500 nm thick crystalline film (see figure 5.19), an additional proof of the ⟨111⟩ growth direction. The 'perfect' triangular structure of the {111} planes shows also angles of 60°.

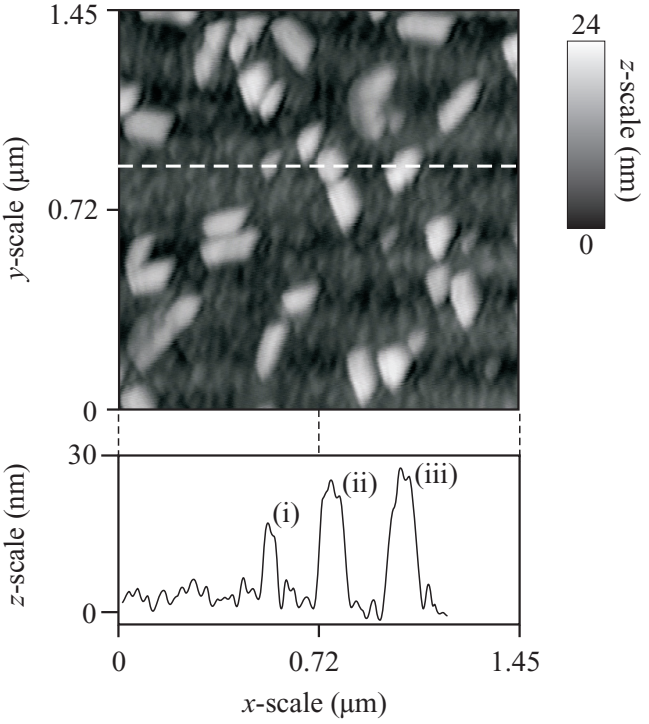

Figure 5.20: *Surface of a 5 nm thick yttria film. The section of the film at the dashed line gives the different widths b and heights h of the crystallites: (i) b = 52 nm / h = 17 nm, (ii) b = 93 nm / h = 22 nm, (iii) b = 102 nm / h = 25 nm*

In contrast to the presented surface roughness values of yttria films, Kim Anh et al. [Kim03] reported a RMS-roughness for a 480 nm thick film of only 0.43 nm. In general, the RMS-roughness is connected with the crystallinity as well as with the film growth mode. In case of large lattice mismatch, the most likely growth mode is the 3D island growth mode resulting in higher roughnesses than in a layer-like 2D growth mode. However, even with no lattice matching between a film and a substrate at all, a 2D layer growth mode can occur, as reported by [Sun96].

The surface roughness of thin films depends on a variety of parameters. As the grade of crystallinity is strongly affected by the substrate temperature, also the surface morphology will change with the substrate temperature. Koren et al. experienced that the roughness can also be manipulated by changing the partial pressure of O_2 in an O_2/Ar backgground gas mixture [Kor00].

Films of Lu_2O_3, Sc_2O_3, and $YScO_3$

A different situation occurs in the Lu_2O_3, Sc_2O_3, and $YScO_3$ films. Even though there is no geometrical structure visible (as in case of the Y_2O_3 film), a preferred growth direction of the grains is actually observed. The surface roughness of these films is of the same order of magnitude as the roughness of yttria films, e. g. a 100 nm thick Lu_2O_3-film has a R_{RMS}-value of 1.3 nm taken from a surface area of 1.23 µm × 1.23 µm.

An AFM-picture of a Sc_2O_3 film with a thickness of 20 nm is shown in figure 5.21. This film has a very low surface roughness of only 1.0 nm. The surface morphology looks similar to the surface of a ⟨111⟩ grown MgO film [Che02], indicating the same growth direction for this scandia film. In the present case, the length of the grains is of the order of 450 nm. With increasing film thickness the grain size increases, e. g. in a scandia film with 100 nm film thickness the length of the crystallites is up to 1.5 µm. This enhanced grain size is resulting in a higher RMS-roughness (here: $R_{\mathrm{RMS}} = 2.3$ nm). At first glance, this seems to be a disadvantage (no sharp interfaces), however as the grains become larger the density of grain boundaries, responsible for scattering, decreases.

The film surface of the mixed system $YScO_3$ is presented in figure 5.22. Since for this system no growth rate was measured, the thickness can only be roughly estimated to 200 nm. One can see that the surface is not an even plane but show a 'squamous' structure, i. e. the single grains overlap partly, similar to the triangular shaped Y_2O_3-surface. In this structure the grains with sizes around 300 nm have also a preferred direction. The roughness of the whole area is 3 nm, while the roughness in the lower left part is only 0.8 nm (marked area (i) in figure 5.22). This comparably large overall roughness can be explained by overgrowth of the islands formed in the beginning of film growth (area (ii)), which will result in smooth films only at larger thicknesses.

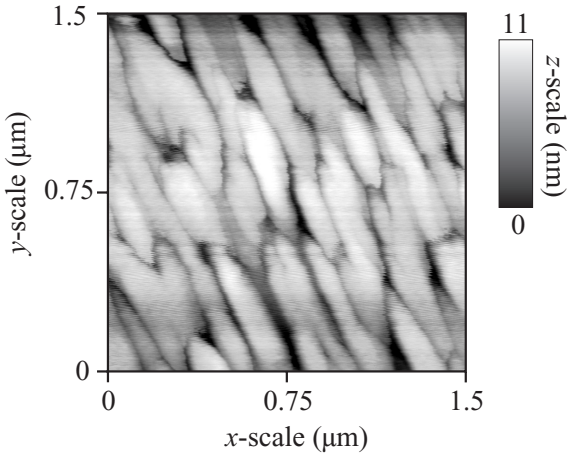

Figure 5.21: *Surface of a 20 nm scandia film.*

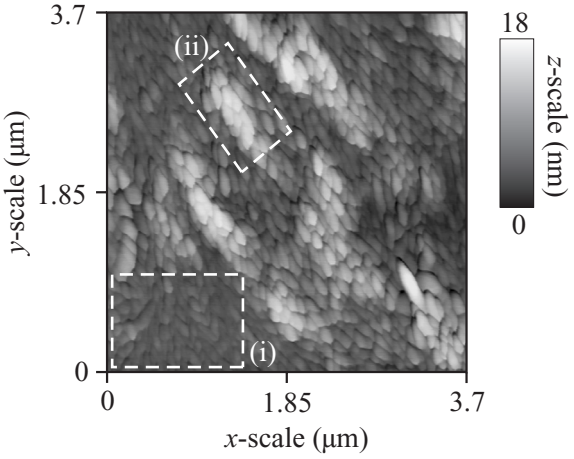

Figure 5.22: *Surface of an $YScO_3$ film (thickness ≈ 200 nm).*

5.4 Optical Spectroscopy

To obtain additional information about the rare-earth-doped thin films, optical spectroscopy has been performed.

Fluorescence and excitation measurements of the thin films in the ultraviolet and visible spectral region have been carried out at room temperature with a modular fluorescence spectrometer (Yobin Yvon FL 321 FLUOROLOG-3). The excitation wavelengths between 250 nm and 600 nm are provided by a high-pressure Xe-lamp and the desired wavelengths are selected by a double monochromator with a reciprocal linear dispersion of $\Delta\lambda/\Delta x = 2.18$ nm per mm slit width. The fluorescence light is resolved with a double monochromator (reciprocal linear dispersion $\Delta\lambda/\Delta x = 2.64$) and then detected either by a photomultiplier (Hamamatsu R 928P), a photoncounter (Hamamatsu R 649) or a CCD camera (Yobin Yvon Spectrum-1 G93), depending on the intensity of the fluorescence light. To separate the emitted light from the excitation light different band edge filters can be used in front of the detection monochromator. The experimental setup is shown in figure 5.23.

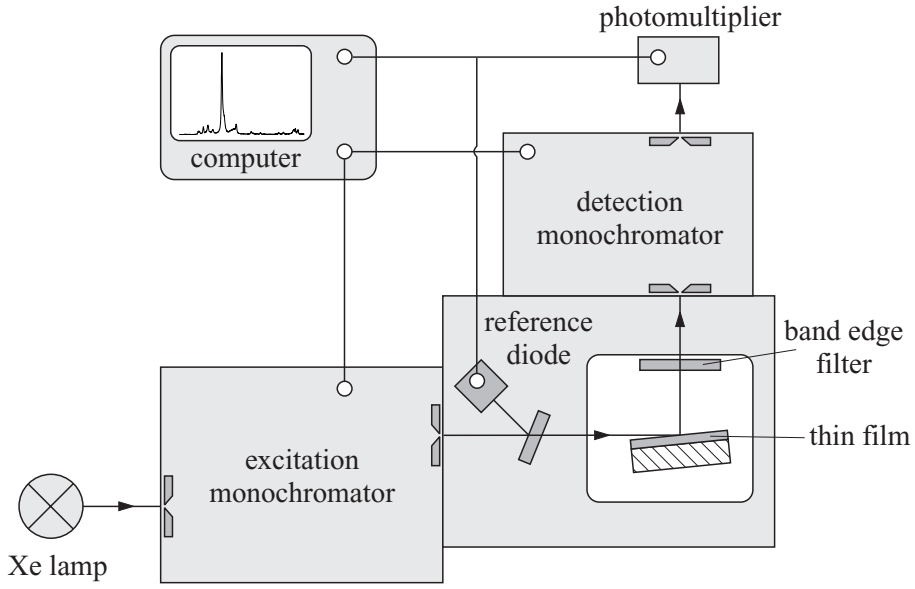

Figure 5.23: *Schematic setup of the* FLUOROLOG *spectrometer.*

For excitation measurements the spectral photon flux of a particular emission band is detected with respect to the variation of the excitation wavelength. The fluorescence signal S is corrected by the apparatus function (spectral distribution of the lamp, spectral sensitivity of the monochromator) given by the signal R of the reference diode.

Fluorescence spectra are taken at a fixed excitation wavelength while the fluorescent light is collected wavelength-dependent using the detection monochromator and one of the described detection units. The recorded signal S is then corrected by the spectral transmission of the detection monochromator and the spectral sensitivity of the detection units.

Additional excitation measurements in the vacuum ultraviolet spectral region (VUV) have been performed at the SuperLumi setup, where excitation wavelengths between 58 nm and 330 nm are available. The source for this wavelength region is the synchrotron radiation of the electron–positron storage ring DORIS at DESY, Hamburg, Germany. In figure 5.24, the simplified setup of this complex platform is shown. A detailed description can be found in [Kam89, Klo89, Möl86, Var94]. The synchrotron radiation is separated spectrically by a primary monochromator with a spectral resolution of 0.3 nm. The fluorescence light of the excited sample is analyzed using a secondary monochromator and detected either with a photomultiplier (excitation measurements) or a CCD camera (emission measurements). The sample holder can be cooled with liquid helium down to 10 K.

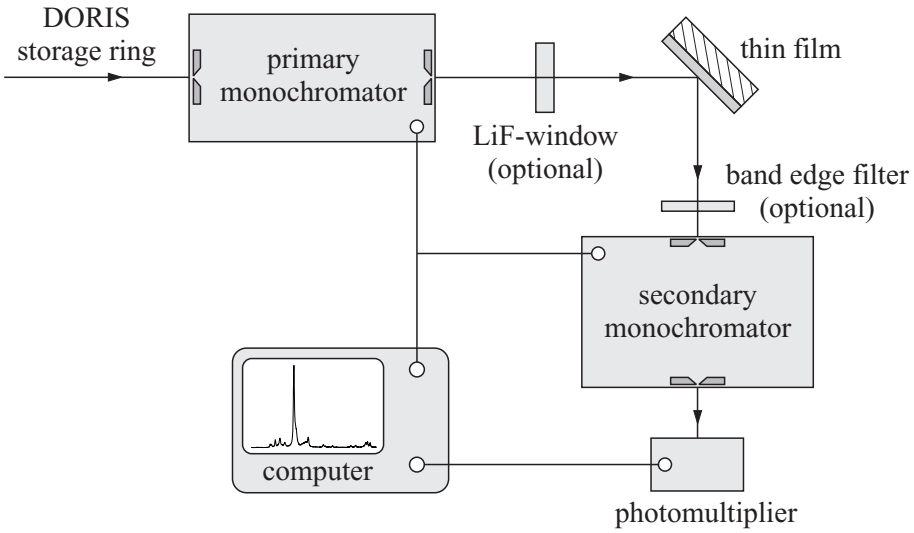

Figure 5.24: *Schematic setup of the* SuperLumi *station.*

5.4.1 500 nm Eu^{3+}:Y_2O_3 Films

First, the luminescence properties of 500 nm thick films fabricated under different growth conditions have been investigated using the Fluorolog spectrometer. In figure 5.25, the emission spectra of an Eu(1%):Y_2O_3 bulk crystal (a), a 500 nm thick crystalline Eu(4%):Y_2O_3 film grown at a substrate temperature of 700° (b), and an amorphous 500 nm thick Eu(4%):Y_2O_3 film (c) grown at room temperature, i. e. T_{sub} = 20°C, are presented. These emission spectra were taken by excitation of Eu^{3+}:Y_2O_3 into the charge transfer band (see section 2.3.4). This band originates from interaction between Eu^{3+} and O^{2-} and ranges from 200 nm to 265 nm with a maximum around 240 nm. This process can be described by an electron transfer from the oxygen ligands to the europium ion: $O(2p^2)Eu(4f^6) \rightarrow O(2p^1)Eu(4f^7)$.

It can be seen that the crystalline film shows a spectrum, which is similar to the reference spectrum of the corresponding bulk material, with the dominating $^5D_0 \rightarrow {}^7F_2$ transitions at 611 nm (see also section 2.3.6). However, despite the similarity between the spectra, a slight broadening of the peaks can be observed. Additionally, around 625 nm a plateau is

formed. In contrast, the spectrum of the amorphous film does not show sharp emission lines due to inhomogeneous broadening. In addition to the Eu^{3+} luminescence, the R_1 and R_2 lines of trivalent chromium – an impurity in the α-alumina substrate – can be observed at 692 nm.

Thus, the luminescence characteristic depends strongly on the substrate temperature during the film growth. This observation is in good agreement with the results obtained by XRD, where an increasing degree of crystallinity with increasing substrate temperature has been observed (see section 5.1.2, p. 53). However, the luminescence behavior of the 500 nm thick films does not depend on the variation of the oxygen pressure during film growth, although an alteration was observed in the diffraction patterns of XRD. The strong broadening of the 2θ peaks in the XRD measurements with increasing oxygen pressure (see figure 5.5, p. 54) indicates a decrease of the crystallite size. Since the Eu fluorescence of these particles has still a crystalline character, the particle size is large enough to provide a long-range order.

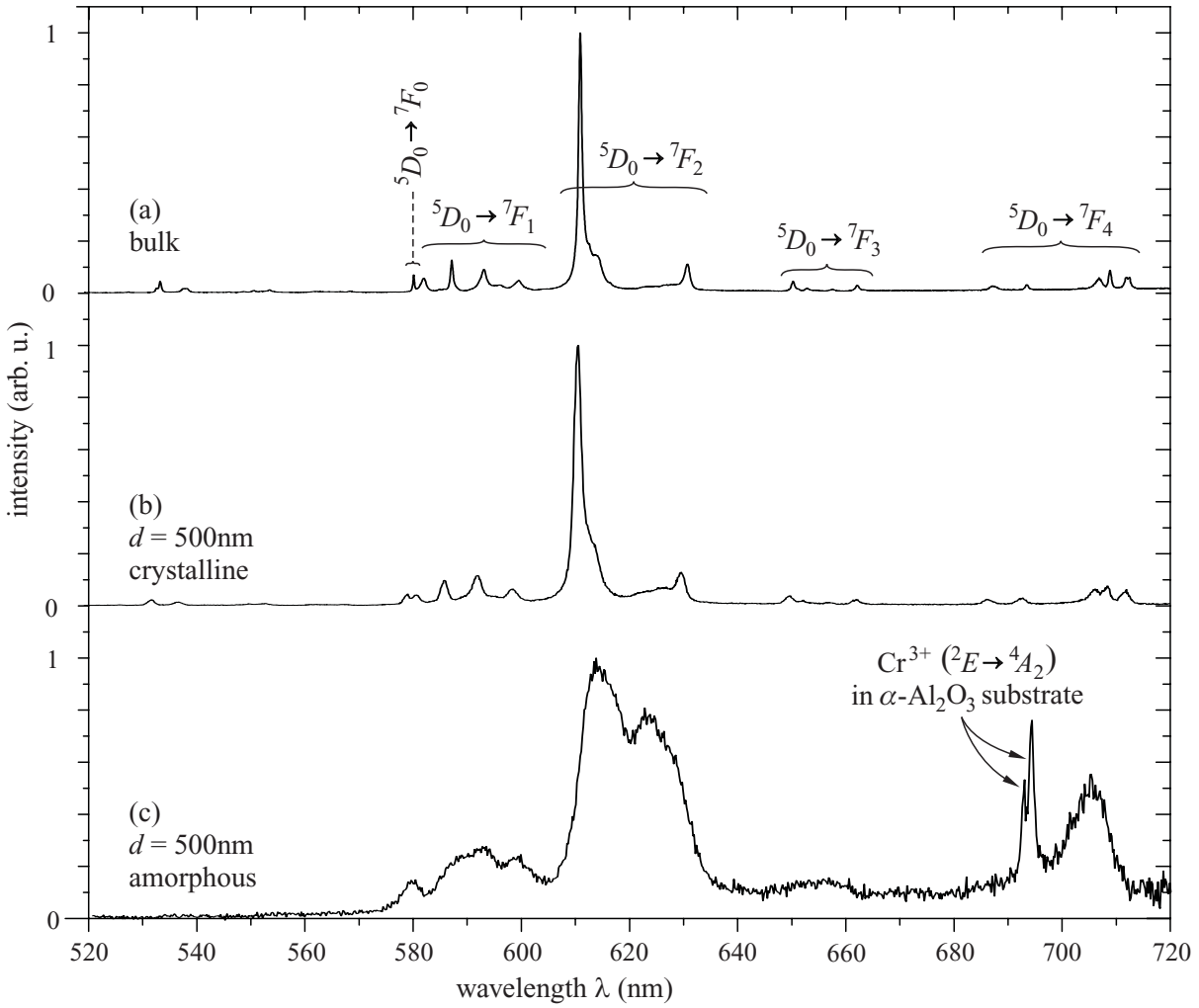

Figure 5.25: *Comparison of Eu(4%):Y_2O_3 emission spectra with different crystallinity: (a) bulk crystal, (b) 500 nm thick crystalline film, (c) amorphous film. Intensity normalized to peak intensity at 611 nm.*

5.4.2 Thin Eu^{3+}:Y_2O_3 Films

In the following, Eu^{3+}:Y_2O_3 films of different thicknesses are investigated by excitation and emission measurements at the FLUOROLOG setup. The film thicknesses are 100 nm, 20 nm, 5 nm, and 1 nm. All films were grown at a substrate temperature of 700℃ and an oxygen partial pressure of 5×10^{-2} mbar.

The excitation spectra ($\lambda_{em} = 611$ nm) shown in the left part of figure 5.26 are characterized by the onset of a strong band starting around 300 nm and peaking around 240 nm. This band is assigned to the charge transfer transition. The excitation spectrum of the 100 nm film has a structure similar to the equivalent bulk excitation spectrum (see figure 5.26 (a)) with the exception that the spectrum presented in figure 5.26 (b) shows a strong broadening of the lines compared to the bulk spectrum. Down to a film thickness of 5 nm, the spectra have the same peak structure (in figure 5.26 (c) the peaks appear very weak due to a short integration time). Additionally, a broad background from 370 nm to 450 nm appears in the 20 nm and 5 nm film. At a film thickness of 1 nm, only this broad structure is visible and no sharp lines can be found.

A more distinct, thickness dependent luminescence behavior can be observed in the emission spectra ($\lambda_{ex} = 243$ nm). The emission spectrum of the 100 nm film is similar to that of a corresponding crystalline bulk sample, except for the plateau between 618 nm and 630 nm (figure 5.26 (b), right). The intense, narrow peak at 611 nm originates from the $^5D_0 \rightarrow {}^7F_2$ transition of Eu^{3+} in the C_2 site whereas the less intense features at 586 nm, 592 nm, and 599 nm belong to the $^5D_0 \rightarrow {}^7F_1$ transition of Eu^{3+} ions occupying the C_2 as well as the C_{3i} site. However, when the film thickness is reduced below 100 nm, the spectrum of Eu^{3+}:Y_2O_3 shows drastic changes as it can be seen in the right part of figure 5.26 (c) - (e). The peak intensity at 611 nm decreases with thinner films and completely vanishes in the case of the 1 nm-film. The peaks at 612.6 nm and 615.5 nm, which can be observed in the shoulder of the 611 nm peak in the 500 nm and 100 nm thick films, can now be resolved (FWHM $\leq$ 1.7 nm), and their intensity increases with decreasing film thickness. These peaks can be assigned to $^5D_0 \rightarrow {}^7F_2$ transitions of the C_2-sites, which are normally very weak (see figure 2.6 ,p. 23). The features around 580 nm, the transition $^5D_0 \rightarrow {}^7F_0$ of the C_2 site at 579.4 nm, and the transition $^5D_0 \rightarrow {}^7F_1$ of the C_{3i} site at 581.2 nm vanish completely in films with a thickness smaller than 100 nm. The peak at 630 nm ($^5D_0 \rightarrow {}^7F_2$), clearly visible in the spectra of the 100 nm and 20 nm films, decreases drastically in intensity in the 5 nm film and vanishes completely in the 1 nm film. In addition, a blue shift of this peak is observed.

Using a single-frequency laser diode (instead of the UV lamp) with a center wavelength of 397 nm (a shift of ±3 nm was possible due to a Littrow configuration), a direct excitation of the Eu-*4f*-levels was possible. The obtained fluorescence spectra remained unchanged compared to the charge transfer excitation spectra. This result indicates that the same luminescence centers with the same local symmetry are involved in this excitation and emission process.

Similar spectroscopic results have been obtained in thin films of Eu^{3+}:Lu_2O_3 as it can be seen in figure 5.31 (p. 88). Independent of CT or direct excitation, the main emission

line at 611 nm vanishes and the two peaks at 613 nm and 616 nm gain intensity. A similar change in the emission characteristics of Eu^{3+} has been observed in nanocrystalline Eu^{3+}:Y_2O_3 [Qi02]. However, in that case the emission was much broader than in the spectra presented here.

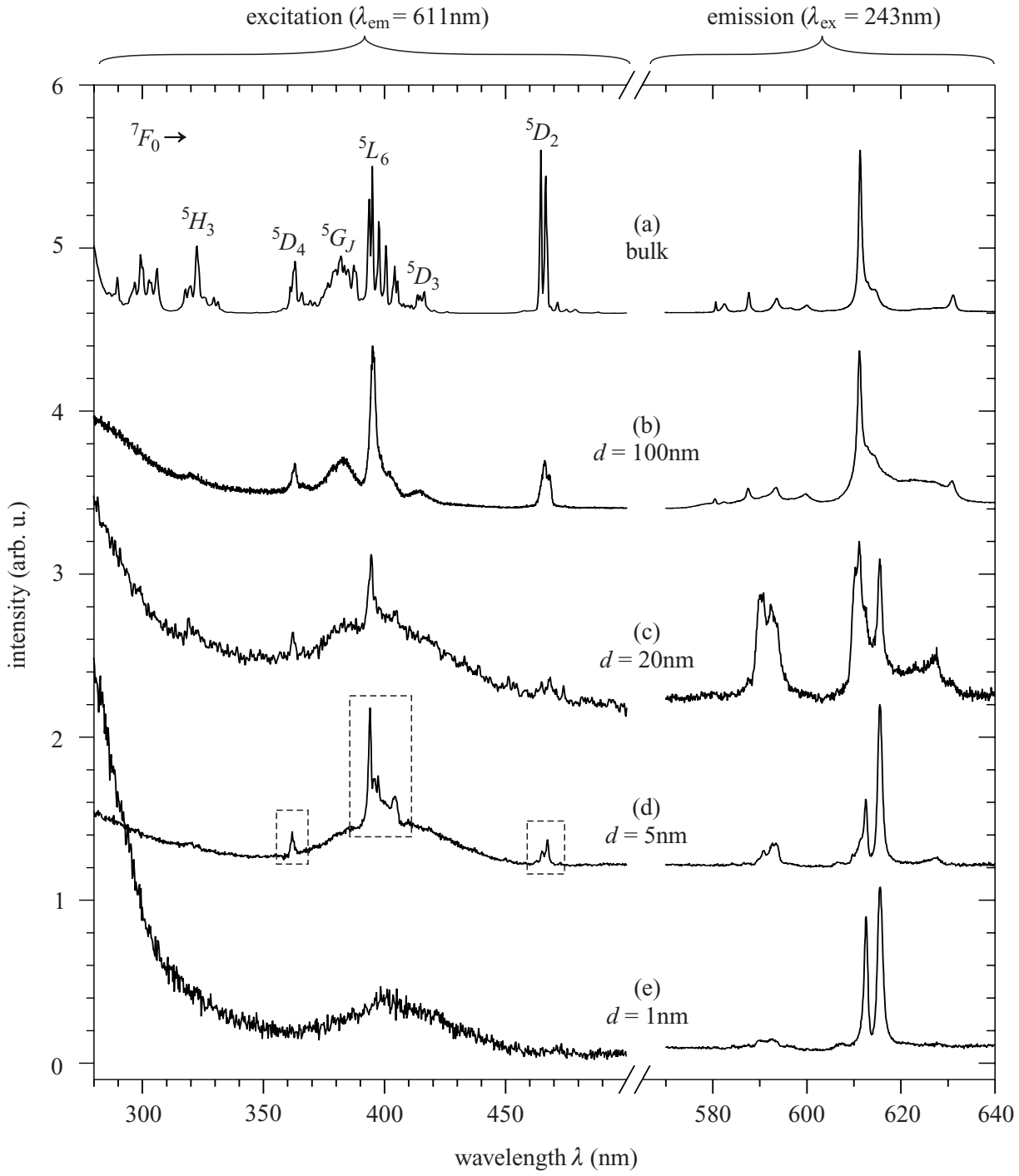

Figure 5.26: *Excitation (left) and emission spectra (right) of Eu(4%):Y_2O_3 films with different thicknesses. The regions marked with a rectangle were measured with a longer integration time.*

VUV Excitation Measurements

To obtain more information about the spectroscopic behavior of thin Eu-doped films, additional excitation measurements have been performed in the VUV spectral range with wavelengths ranging from 58 nm to 350 nm at SuperLumi (see p. 76). In these experiments a variation of luminescence behavior can be observed in films with different thicknesses, too.

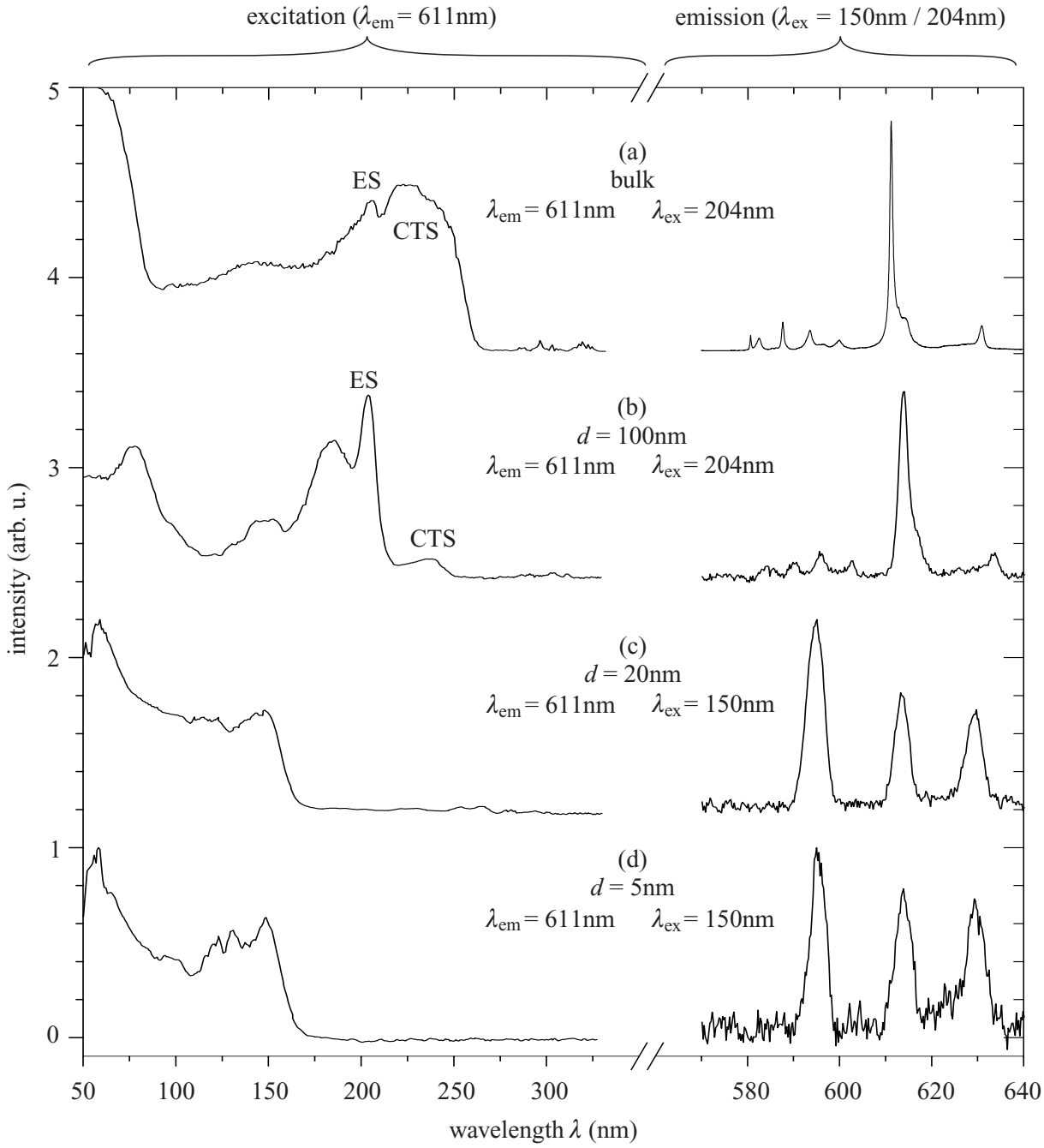

Figure 5.27: *VUV excitation and emission spectra of Eu(4%):Y_2O_3 films. ES - excitonic state, CTS - charge transfer state.*

As already observed in the previous luminescence experiments, the excitation and the corresponding emission spectrum is similar to the bulk spectrum only in the case of the 100 nm thick film (see figure 5.27 (a) and (b)). In the excitation spectrum of the 100 nm film ($\lambda_{em} = 611$ nm), the small structure around 240 nm can be identified as the CTS. The strong peak at 204 nm (6.08 eV) corresponds to the well-known excitonic state (ES). Subsequent to the ES, the interband transitions of Y_2O_3 are visible. Abramov et al. [Abr78] explained the structure in the excitation spectrum for energies smaller than 6.6 eV by the contribution of the *4d*-states of yttrium in the conduction band. Excitation of the excitonic state (ES) leads to the well-known emission spectrum of europium-doped yttria due to an energy transfer from the ES to the ^5D_J states of the Eu^{3+}-ion. In contrast to the work of P. Burmester [Bur02], no radiative decay of the excitonic state at 345 nm (3.6 eV) was observed – although the excitonic state dominates the excitation spectrum. Since the ES exists in the 100 nm thick film, an explanation of this different behavior is a fast relaxation from the ES to lower lying energy levels, finally resulting in a population of the Eu^{3+} $^5D_0$ level.

In case of the 20 nm and 5 nm thick films, the excitonic structure and the yttria interband transitions vanish. Instead, there appears a peak at 150 nm (8.26 eV), which can be interpreted as band-to-band transitions of a different, newly-formed material, e. g. YAG. Interestingly, the fluorescence spectrum arising from the excitation of the state at 8.26 eV is different compared to direct excitation or CT excitation and leads to three emission peaks at 595 nm, 613.5 nm, and 629.4 nm with a peak width of about 4.5 nm each (FWHM). Thus, there are hints for the assumption that these Eu^{3+}-ions are not located in an Y_2O_3 matrix, but in YAG or $YAlO_3$ (see following discussion).

In general, the excitation of an exciton occurs only in a surface layer with a thickness $\lesssim 100$ nm, whereas the CT process can occur to depths of 5 µm. Thus, in thin films the excitonic transitions are expected to be more efficient than the CT process. However, also in thin films the ES can be considerably influenced especially when the film thickness has the same dimension as the radius of the exciton. In the excitation spectra 5.27 (c) and (d) of the 20 nm and 5 nm thick films no excitonic transitions to the Eu^{3+} are visible. However, this does not mean that an excitation of the ES is not possible but only that no energy transfer from the ES to the Eu^{3+} occurs.

Discussion of the Spectroscopic Results

The change in luminescence behavior of thin films (thickness $\leq 20\,\text{nm}$) compared to the bulk crystal and thick films can be summarized by the following four observations:

1. Direct excitation into the ^5D_J levels of Eu^{3+} leads to two strong emission peaks at 612.5 nm and 615.5 nm.
2. Excitation into the CT band results in the same effect.
3. No visible luminescence from Eu^{3+} occurs when excited into the ES.
4. The band-to-band excitation at 8.26 eV results in three emission lines at 595 nm, 613 nm, and 629 nm.

These observations lead to the conclusion that there are actually two different luminescence centers occupied by Eu-ions. Since impurities like other rare-earth ions can be excluded due to the energetic positions of the emission lines, the Eu-ion must be present at two different crystallographic surroundings.

In the following, various effects leading to a change of the emission characteristics of Eu^{3+}:Y_2O_3 are presented, and their influence on the film–substrate system is discussed. Of special interest are effects, which can occur due to miniaturization of a solid (interface and surface effects, quantum confinement), but also the possibility of intermixing compounds is considered.

i) Interface Effects

Most important for the effects occurring in the luminescence spectra of thin films are interface and surface effects. Due to the lattice mismatch between the Al_2O_3-substrate and the Y_2O_3-film, the dopant ions (here: Eu^{3+}) can have a locally varying coordination number. Additionally, an important parameter is the bond length between the metal ion and its ligands. Apart from lattice matching, the epitaxial film growth depends on the deformation of the bonds, which directly influences the optical properties of the luminescent centers. In the present case, the (0001) surface plane of the Al_2O_3-substrate can consist of oxygen atoms. However a set of three O^{2-}-ions belongs to one Al^{3+} coordination sphere. The Eu^{3+} is sixfold coordinated in the Al_2O_3 matrix as well as in the Al_2O_3 matrix. Therefore, it is possible that the set of three O^{2-}-ions belongs to the coordination sphere of an Eu^{3+}-ion in the first layer of a grown film, too. However, the Al–O bond length in Al_2O_3 is shorter than the Y1–O and Y2–O bond length in Y_2O_3 by 19.5% and 18.1%, respectively. Consequently, a shortened Eu–O bond length with respect to the bulk crystal is expected at the interface. This comparatively large mismatch in cation coordination sphere radius will influence the film properties at the interface.

Calculations by Burmester indicate that even small variations of the distance between Eu and O can result in a significant modification of the electronic band

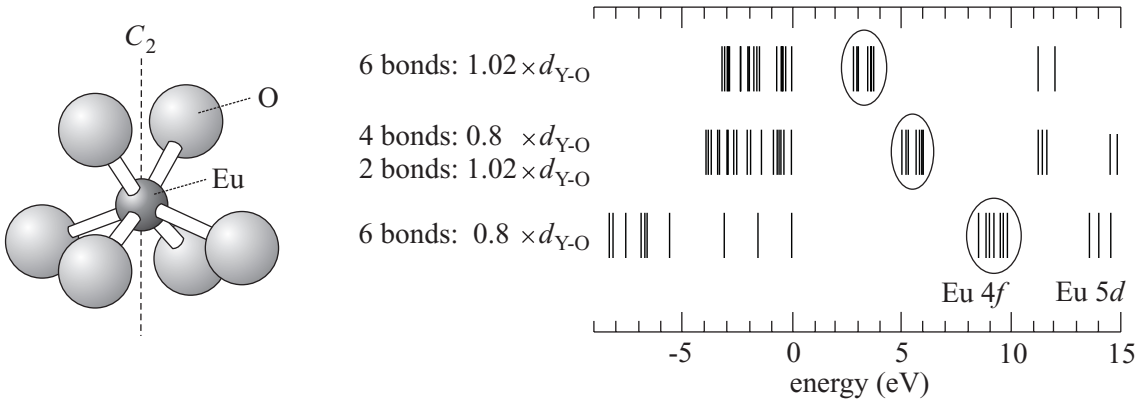

Figure 5.28: *Relative energy level positions of O 2p and Eu 4f 5d states due to bond length variations in an Eu-O_6-cluster with C_2-symmetry* [Bur02].

structure [Bur02]. Figure 5.28 shows the relative positions of the O *2p* and Eu *4f 5d* energy levels for different Eu–O bond length in C_2 symmetry. The basis for these self-consistent, relativistic one-electron cluster-calculations was an EuO_6 cluster as depicted in figure 5.28. In the first case, the Eu–O bond length was stretched by 2% compared to the Y1–O bond length in Y_2O_3 because in sixfold coordination the radius of the Eu^{3+}-ion is 3% larger than the radius of the Y^{3+}-ion. The O *2p* state with the highest energy, representing the upper edge of the valence band, is set to $E = 0\,\text{eV}$. In the energy level structure the bond length of the four in-plane oxygen ions were shortened by 20% whereas the remaining two bonds are again stretched by 2%. If all six bonds are shortened by 20% the energy difference between the O *2p* and the Eu *4f* states is increased further. This result indicates not only a blue shift of the charge transfer band but also variations of the energetic positions of the Eu *4f* levels when the bond length are shortened. In addition, the ions do no longer occupy the correct lattice positions, and thus, the former symmetry is broken. This has the effect, that normally forbidden transitions become allowed due to an admixing of states with different parity. This would also explain the sharp lines obtained by optical spectroscopy, showing clearly crystalline behavior of the films. This result is in good agreement with the results of the XRD and RBS measurements, which indicate crystalline growth of the films, too.

ii) Surface Effects

In addition to the different local environment of the Eu-ions due to interface effects, surface effects may also play an important role for the luminescence behavior. As seen in section 5.3, in the early stages of film growth, the formation of 3D-islands in the nm-range takes place. In this case, the crystallites have a large surface area compared to their volume, where unsaturated bonds or lattice defects can occur in a large number leading to surface defect states.

Since at the surface as well as at the interface the lattice periodicity along the surface normal is disturbed, the coordination number (CN) of surface atoms is reduced. This reduction will shorten the remaining bonds of the surface atoms. Sun found out that CN-induced bond contraction is independent of the chemical bond or the

dimension [Sun99]. This mechanism has been evidenced for a number of materials, e. g. a bond contraction of 13% on nitride surfaces or 4–12% bond contraction of O–Cu bonding [Sun01]. Using Extended X-ray Absorption Fine Structure (EXAFS) analysis, Qi et al. observed a significant change in the coordination number in Eu^{3+}:Y_2O_3 nanoparticles with a size of about 10 nm [Qi02].

iii) Quantum Confinement

Related to the surface effects are quantum confinement effects. Quantum confinement describes how the electronic properties, i. e. the position of the energy levels, change when the radius of the particles R reaches the dimension of the Bohr radius a_B. For example, semiconductor nanocrystals exhibit a shift of the absorption edge to higher energies due to quantum confinement. This increase in band gap energy leads to a blue shift in luminescence. However, up to now, no quantum confinement effects in nanocrystalline yttria have been observed. This is due to the fact that in insulating oxides, like Y_2O_3 or YVO_4, the Bohr radius of the exciton is very small ($a_{B,exc} \approx 1$ nm). Based on the works of Kayanuma [Kay88] and Konrad et al. [Kon01] the particle-size-dependent energy shift ΔE of the exciton excitation energy due to quantum confinement can be estimated by

$$\Delta E = \frac{\hbar^2 \pi^2}{2(m_e + m_h)} \frac{1}{R^2} , \tag{5.14}$$

where m_e and m_h are the mass of the electron and the mass of the hole, respectively. Typically, $\Delta E \approx 1$ meV in the regime of weak confinement, where the particle radius R satisfies $R \geq 4a_B$. However, this energy shift is too small for a sufficient explanation of the observed luminescence effects. Moreover, due to the strongly localized electrons of rare-earth-ions in a crystalline matrix no confinement of electronic states can occur. Thus, the theory of quantum confinement cannot be applied to the thin Eu^{3+}:Y_2O_3 films to explain the change in emission characteristics.

Other confinement effects may be induced by inter-ionic electronic interaction and electron-phonon interaction. Due to the large surface area of crystallites in the nm-range a hydrostatic pressure, caused by the Gibbs–Thomson effect, might increase the phonon energy or the coupling constant [Kon01]. The presence of a hydrostatic pressure can lead to a phase transition in nanocrystalline yttria forming the high pressure monoclinic phase as observed by Skandan et al. [Ska92]. But also these effects are not suitable to give a correct interpretation of the spectra.

iv) Subplantation Effects

In the process of PLD the ns-laser ablated particles can have energies up to 100 eV. Depending on the target–substrate distance and the oxygen pressure they lose a certain amount of this energy. As in the used experimental setup this distance was only 3.5 cm, the particles hitting the surface had enough energy to implant Eu:Y_2O_3 into the Al_2O_3 matrix of the substrate.

In this case, not only the resulting different bond length has an influence on the spectroscopic behavior, e. g. when an Eu-ion is incorporated on an Al-site, but

also the lattice deformations in the substrate caused by the subplantation. The subplantation of Y- and Eu-ions into the Al_2O_3-matrix will result in significant lattice deformations, because the radius of the sixfold coordinated Al^{3+}-ion is only 0.54 Å, while the sixfold coordinated Y^{3+} and Eu^{3+}-ions have radii of 0.92 Å and 0.98 Å, respectively. Thus, within the first coordination sphere of Y (Eu) in Al_2O_3, oxygen vacancies are created, while in the second sphere O-ions are incorporated at interstices, and the coordination of Y (Eu) is reduced from sixfold to threefold.

Depending on the Y_2O_3 concentration, i. e. the ratio between Y_2O_3 and Al_2O_3, the formation of three intermediate compounds of very different crystal structures between Y_2O_3 and Al_2O_3 can take place, namely $YAlO_3$ (YAP), $Y_3Al_5O_{12}$ (YAG), and $Y_4Al_2O_9$ (YAM).

The most likely are the double oxides $3 \times Y_2O_3 + 5 \times Al_2O_3 \rightarrow 2 \times Y_3Al_5O_{12}$ (YAG – yttrium aluminum garnet) and $Y_2O_3 + Al_2O_3 \rightarrow 2 \times YAlO_3$ (yttrium orthoaluminate). Since $YAlO_3$ has a bandgap energy of only 7.7 eV [Abr78], the measured spectrum indicates the bandgap energy of YAG ($E_{\mathrm{gap}} = 8.2\,\mathrm{eV}$). In case of the formation of YAG, the Eu-ions are eight-fold coordinated, while in $YAlO_3$ the coordination number is 12. However, the coordination sphere of $YAlO_3$ is not really spherical and shows a character, which is more like eight-fold coordinated. Thus, the incorporation of Eu^{3+} in YAG and $YAlO_3$ is similar.

Both, the direct and the CT excitation of the Eu^{3+}-ions result in considerably modified fluorescence characteristics in films with thicknesses $\leq$ 20 nm compared to the corresponding Eu:Y_2O_3 bulk emission. Since these films are characterized by strong 3D island growth (instead of a completely closed film surface), surface effects are responsible for partial annihilation of transitions ($^5D_0 \rightarrow {}^7F_0$), change in intensity relations ($^5D_0 \rightarrow {}^7F_2$ at 612.6 nm and 615.5 nm compared to $^5D_0 \rightarrow {}^7F_2$ at 611 nm), and for shifts in transition lines (blue shift of $^5D_0 \rightarrow {}^7F_2$ at 630 nm). With increasing film thickness, resulting in a completely closed film surface, the characteristic Eu^{3+}:Y_2O_3 fluorescence can be observed. Thus, the different local environment around the Eu^{3+}-ions compared to the bulk structure (due to the interface and the large surface-to-volume ratio) leads to changed bond lengths and changed coordination numbers of the Y(Eu)–O shell. These are the parameters responsible for the observed effect.

Excitation of the Eu-ions in the VUV spectral region at 150 nm yields a completely different emission spectrum with three strong peaks. While the excitation wavelength corresponds to the bandgap energy of YAG, the emission details are attributed to a mixture of Eu:YAG and Eu:$YAlO_3$ (see figure 5.29). Since the band edge of $YAlO_3$ ($E_{\mathrm{gap}} = 7.7\,\mathrm{eV}$) is slightly below the band edge of YAG, Eu-ions in both crystallographic matrices can be excited explaining the mixture of emission. However, in the subplantation region the lattice of YAG as well as the lattice of $YAlO_3$ are strongly distorted. These deformations result in a different electronic structure. These changes give an explanation of the missing excitonic state at 7.2 eV in the excitation spectra. Additionally, the disturbed lattice has a considerable influence on the positions of the Eu^{3+} energy levels, because the local crystal field is changed. This leads to a shift as well as to a broadening of the emission lines, and the peaks of Eu:YAG and Eu:$YAlO_3$ cannot be resolved resulting in three broad peaks

(FWHM ≈ 4.5 nm) as it can be seen in figure 5.29 (a).

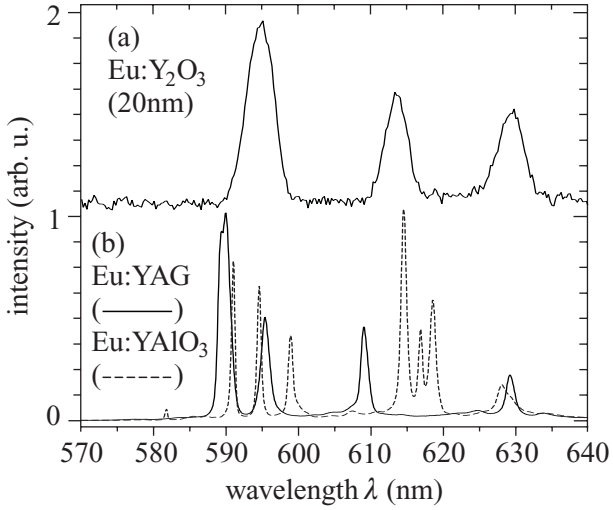

Figure 5.29: *(a) Emission spectrum of 20 nm Y_2O_3, (b) emission spectra of Eu:YAG and Eu:$YAlO_3$ bulk crystals.*

The strong blue luminescence observed by P. Burmester in Eu:Y_2O_3-PLD-films directly grown on α-Al_2O_3 is not observed [Bur02]. This luminescence is attributed to Eu^{2+}-ions in the interface region. An explanation for the different luminescence behavior, although the films were prepared by the same method using the same target materials, is the kinetic energy of the particles hitting the substrate surface. Compared to other PLD experiments, relatively short target–substrate distance have been used here. Correspondingly, the plume species have high kinetic energies leading to more significant subplantation effects. This model is supported by the spectroscopic results of EBV-fabricated Eu:Y_2O_3-films by L. Rabisch, Institute of Laser-Physics, Hamburg, Germany. Due to the low particle energies in the EBV process, no significant interaction with the substrate occurs, and the resulting films show only the well-known Eu^{3+} luminescence.

Surface Cover Layer

If the observed change in the spectra presented in figure 5.26 is due to a surface effect an undoped Y_2O_3 cover layer on top of the grown films should allow to answer this question. The influence of an in-situ grown cover layer on top of $\sim$1 nm thick Eu:Y_2O_3 films was already demonstrated. The Eu-spectra of these film are similar to the bulk spectrum, whereas the spectra of the 1 nm thick films without a cover layer show an amorphous character. Therefore, the thin films presented in this work (1 nm − 100 nm) were covered with an undoped yttria layer using the technique of EBV. However, no change in the spectra is observed here. A possible explanation might be the fact, that the films were kept in air during all former investigations. As a consequence the film surface is contaminated with different organic compounds, which prevent continuous film growth. Thus, with this 'ex-situ' method of fabricating a cover layer, no interpretation of the spectra by means of surface effects is possible.

Post-Deposition Annealing

Since the deposition of an undoped Y_2O_3 cover layer on top of the thin films had no influence on the spectroscopic behavior (see page 86), post-deposition annealing at 1000°C has been performed on films with different thicknesses (1 nm, 5 nm, 20 nm, 100 nm and 500 nm). To avoid thermal stress, the heating and the cooling process took 36 h each, while the annealing time at 1000°C was set to 24 h. As a result, the optical behavior changed

dramatically as it can be seen in figure 5.30 (a)-(d). Additionally, XRD measurements have been performed on these tempered films, and a change in the crystalline structure can be observed (figure 5.30 (e)), too. In the XRD spectrum of the 500 nm thick Y_2O_3 film annealed at 1000°C for 24 h one can clearly identify the main Y_2O_3 diffraction peaks. However, after annealing the film is not as highly textured along the ⟨111⟩ direction as it was before (see section 5.1.2, p. 53). Instead a more polycrystalline structure is visible (diffraction peaks of {211}, {222}, {400}, {622}, {613}, and {444}). In addition, many different peaks can be resolved. These peaks can clearly identified as the diffraction peaks of $YAlO_3$ and YAG. This result is interesting because Korzenski et. al [Kor00] observed a significant increase in the crystallinity of their Y_2O_3 films by post-deposition annealing in an oxygen ambient at 800°C, 1000°C, and 1200°C for 1 h. The complete different behavior (grade of crystallinity as well as luminescence characteristics) of the samples presented here is a result of the long annealing time of 24 h. The mobility of the ions starts at temperatures around 800°C. At 1000°C the mobility is still quite small, but due to the long time and the small film thickness, a mixing of Al_2O_3 and Y_2O_3 is possible. As a consequence the formation of YAG or $YAlO_3$ can take place.

Since at the subsurface layer the formation of YAG and $YAlO_3$ has already occured due to subplantation, the process of replacing Y_2O_3 by YAG and $YAlO_3$ expands to the surface. Consequently, no Eu:Y_2O_3 fluorescence is observed after the annealing process. The fact that the resulting emission spectra at excitation wavelengths of 255 nm differ from the corresponding YAG and $YAlO_3$ bulk spectra (figure 5.29) can be explained by a strong intermixing of the compounds. As a result, one has to deal with distorted and non-regularly oriented crystallites of Eu-doped Al_2O_3, $Y_3Al_5O_{12}$, $YAlO_3$, $Y_4Al_2O_9$, and Y_2O_3.

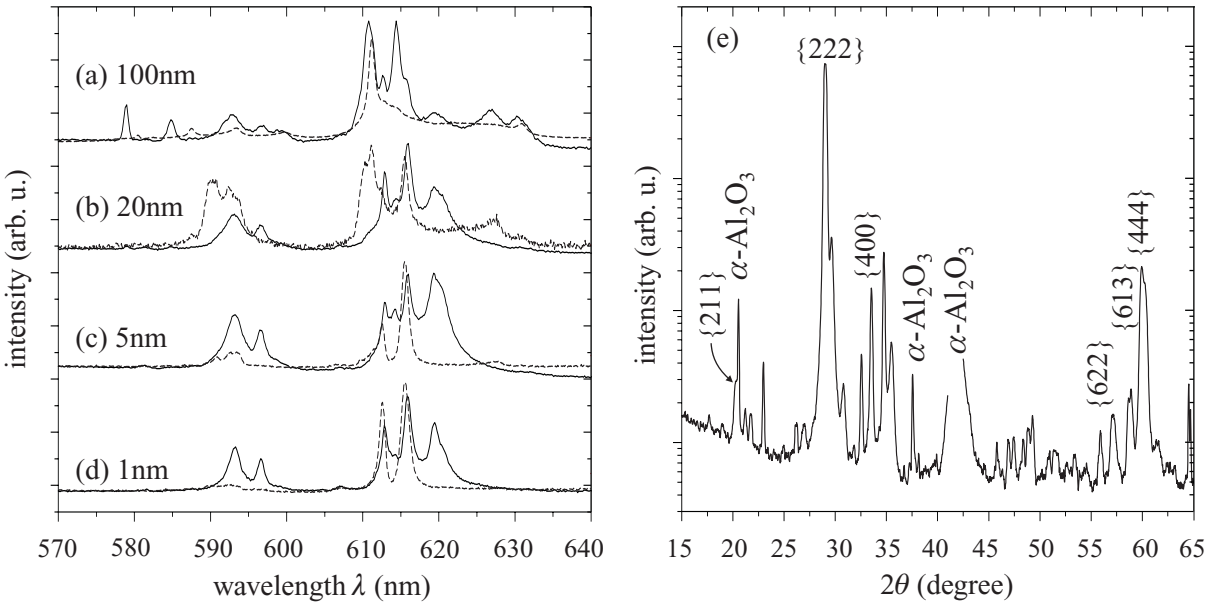

Figure 5.30: *(a)-(d) Emission spectra ($\lambda_{ex} = 255$ nm) of thin yttria films after annealing at 1000°C. The dashed curve represents the original spectrum while the solid line indicates the annealed samples. (e) XRD spectrum of a 500 nm Eu(4%):Y_2O_3 after annealing at 1000°C. The {hkl} values belong to cubic yttria.*

5.4.3 Thin Eu^{3+}:Lu_2O_3 Films

The phenomenon of changing luminescence behavior when the film thickness is decreased, as observed in Eu:Y_2O_3, can also be seen in Eu:Lu_2O_3 as depicted in figure 5.31 and 5.32.

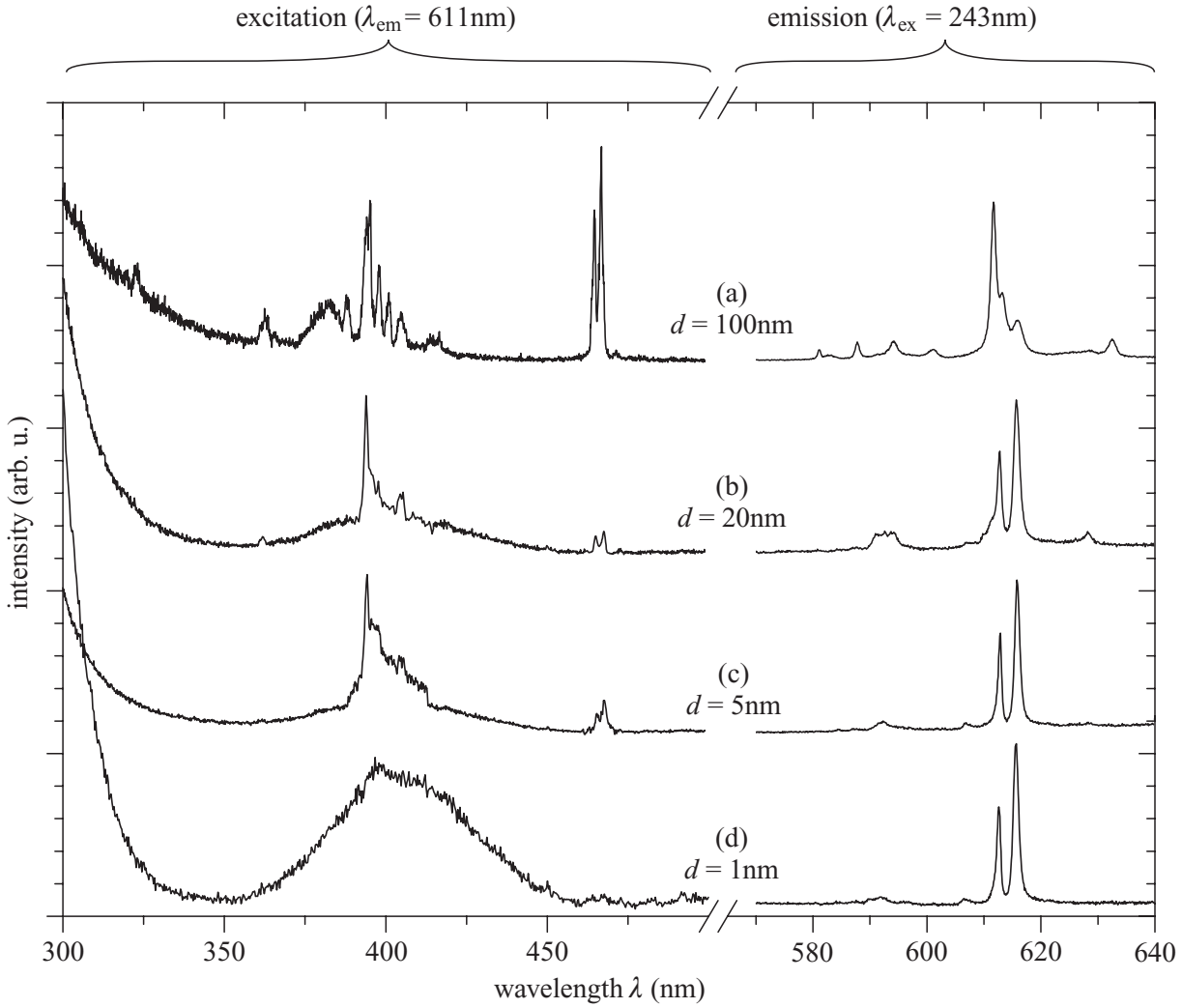

Figure 5.31: *Excitation (left) and emission (right) spectra of Eu(4%):Lu_2O_3 films with different thicknesses.*

The excitation spectra in the spectral range 300 nm – 550 nm (emission at $\lambda_{em} = 611$ nm) correspond to the Eu^{3+} energy levels, but additionally a broad background peaking at 400 nm occurs for films with a thickness $\leq$ 20 nm. In case of the 1 nm thick film, no peaks except the broad structure are visible. Only in case of the 100 nm film excitation into the charge transfer band reveals the 'correct' Eu^{3+}-emission. For thinner films, the same double-peak structure as in Eu:Y_2O_3 at 613 nm and 616 nm can be observed (FWHM $\leq$ 1.1 nm). The $^5D_0 \rightarrow {}^7F_0$ and the $^5D_0 \rightarrow {}^7F_1$ transitions between 580 nm and 600 nm vanish completely. Instead, there appears a broad feature at 593 nm in the 20 nm film, which decreases in intensity in the 5 nm and 1 nm films. Additionally, the blue shift of the peak at 630 nm, already observed in Eu:Y_2O_3 appears also in Eu:Lu_2O_3.

VUV Excitation Measurements

The results of the VUV excitation measurements of Eu:Lu_2O_3 are also very similar to the Eu:Y_2O_3 spectra. Only in case of the 100 nm thick film, the characteristic excitonic state at 210 nm (5.9 eV) can be observed. If the excitation occurs into this state, then the corresponding emission spectrum is similar to that of a bulk crystal (see figure 5.32 (a), solid line). Additionally, a band edge at 147 nm is observed in this excitation spectrum ($\lambda_{em} = 611$ nm). Excitation into this band edge, i. e. $\lambda_{ex} = 147$ nm, leads to a different emission spectrum (dashed spectrum line in figure 5.32 (a)). This peak can be assigned to starting interband transitions in the mixed compound $Lu_3Al_5O_{12}$ (LuAG) resulting from subplantation. In contrast to the yttria films, in this 100 nm thick film it is possible to investigate the two different Eu^{3+}-surroundings of Lu_2O_3 and LuAG simultaneously. Since the effect of changing luminescence behavior when the film thickness is decreased has been observed in Y_2O_3 films as well as in Lu_2O_3 films, the explanation of subplantation is the most favorable (compared to the other possibilities discussed in the previous section).

The excitonic state at 5.9 eV vanishes when the film thickness is decreased further ($\leq$ 20 nm), and only the band-to-band transitions of LuAG occur in these films, as it can be seen in figures 5.32 (b) and (c). Excitation into the conduction band results again in the three-peak emission structure originating from Eu^{3+}-centers in distorted LuAG and $LuAlO_3$ matrices.

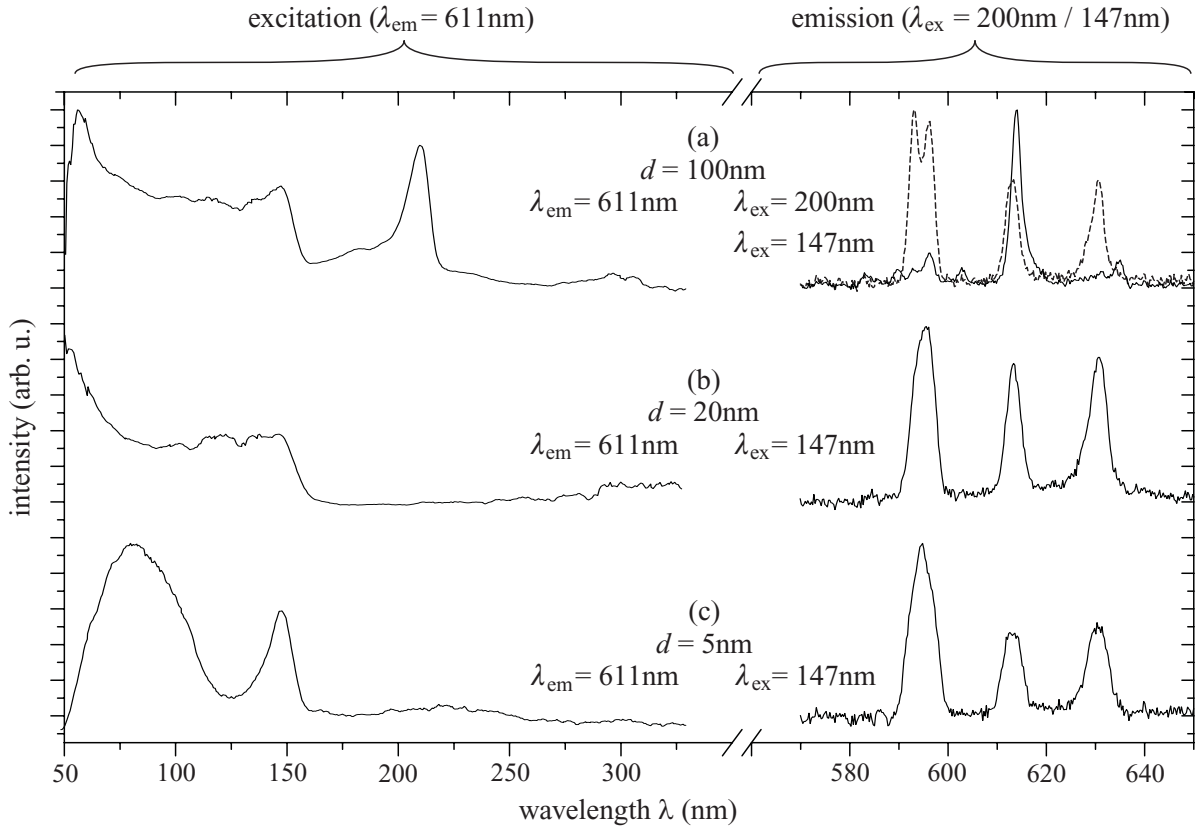

Figure 5.32: *Excitation (left) and emission spectra (right) of Eu(4%):Lu_2O_3 films with different thicknesses.*

5.4.4 Thin Er^{3+}:Sc_2O_3 Films

In addition to europium, other rare-earth ions have been incorporated in sesquioxide films, too, e. g. erbium. Using a single-crystal target of $Er^{3+}(3\%):Sc_2O_3$, films with thicknesses of 1 nm, 5 nm, 20 nm, and 100 nm have been fabricated on α-Al_2O_3. Scandia is very interesting for thin film production, because it offers the smallest lattice mismatch among the sesquioxides with respect to the alumina substrate (see section 3.3).

Up to now, no complete spectroscopic characterization of the Er-doped films has been carried out, because of the complex energy level scheme of erbium and the diversity of transitions possible (see figure 5.33), but only fluorescence measurements in the near infrared. The fluorescence was measured via lock-in technique in the infrared region from 1.4 µm – 1.7 µm with a liquid nitrogen cooled Ge-photodetector. For excitation of the trivalent erbium ions into the $^4F_{7/2}$-level, an Ar-ion laser operating at 488 nm was used. Non-radiative and radiative transitions lead to population of the $^4I_{13/2}$-level from where the fluorescence around 1.55 µm into the $^4I_{15/2}$ ground state was observed. Using a grating with 1200 grooves/mm, the CHROMEX monochromator had a reciprocal linear dispersion of 3 nm per mm slit width. The results of the measurements are presented in figure 5.34 (a)-(c).

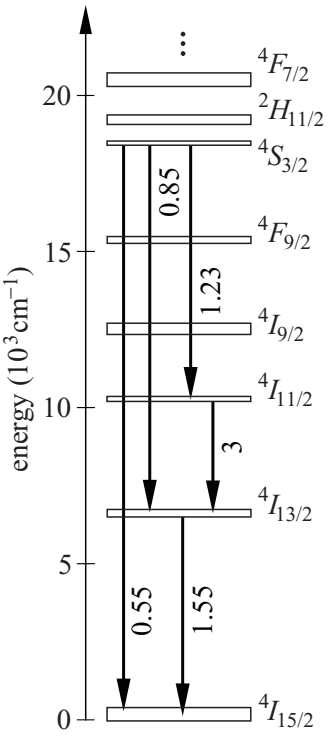

Figure 5.33: *Energy level scheme of Er^{3+} in Sc_2O_3. Transition wavelengths in µm.*

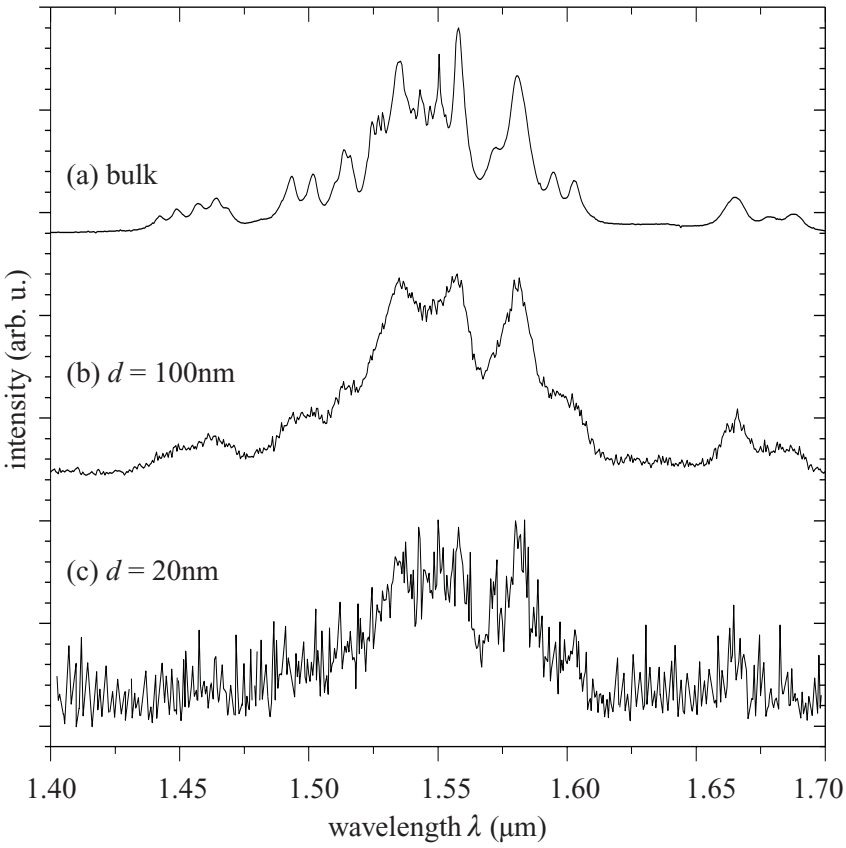

Figure 5.34: *Infrared (IR) emission spectra of $Er(4\%):Lu_2O_3$ films with different thicknesses ($\lambda_{ex} = 488$ nm).*

The spectrum of the bulk crystal was recorded with 0.15 nm resolution, while for the spectra of the 100 nm and 20 nm thick films a resolution of 0.75 nm and 1.5 nm, respectively, was used. It can be seen that the europium spectra of the thin films have the same structure as the corresponding bulk spectrum (in contrast to the Eu-doped Y_2O_3 and Lu_2O_3 films). However, a broadening of the peaks can be observed, and thus, there are fewer features visible in the spectrum. This behavior indicates an amorphous character of the films, which is surprising, because scandia films should have a more crystalline behavior than yttria or lutetia due to the smaller lattice mismatch. However, the target–substrate distance as well as the laser fluence used for the deposition was the same as for the fabrication of the Y_2O_3 and Lu_2O_3 films, and thus, also in this case subplantation can take place.

6 Waveguides

The importance of the production of planar waveguides as key elements in integrated optics was already discussed in chapter 1. Thus, only a brief description of planar waveguide theory and first results of planar yttria waveguides are presented here. The first part presents a model to calculate the spatial mode profile of a guided wave in a three-layer asymmetric planar waveguide device. This model follows the general work of Yariv [Yar89] and Lee [Lee86] and the recent, more specialized derivation of Bonner [Bon00]. The model developed is then applied to the Y_2O_3 waveguides fabricated during the course of this thesis, and the results of the waveguide experiments are presented.

6.1 Theory of Waveguides

First, a three-layer asymmetric waveguide is considered to introduce common terminology. Figure 6.1 shows a geometrical interpretation of light confinement within a waveguide structure. The core is the active layer, while the substrate and superstrate are the media surrounding the core. In the ray-optical model, the confinement or guidance of light in a film can be described by the phenomenon of total internal reflection. If the refractive index of the film n_f is larger than the refractive indices of the surrounding media, n_s of the substrate and n_c of the superstrate, total internal reflection is possible. The critical angle of total internal reflection θ_crit is given by

$$\sin\theta_{\mathrm{crit,c/s}} = \frac{n_\mathrm{c/s}}{n_\mathrm{f}} \,. \tag{6.1}$$

Thus, guiding of light inside the film requires angles of incidence θ greater than the critical angle θ_crit, i. e. $\theta \geq \theta_\mathrm{crit}$. Due to this condition, the coupling angles θ_in are restricted to a certain range,

$$n_0 \sin\theta_\mathrm{in} \leq \sqrt{n_\mathrm{f}^2 - n_\mathrm{c/s}^2} \tag{6.2}$$

where n_0 is the refractive index of the medium from which the coupling takes place. The maximum allowed value of the product $n_0 \sin\theta_\mathrm{in}$ is defined as the numerical aperture NA. The propagation inside the film can be described by the z-component of the wavevector $\mathbf{k}$ in a medium having an effective refractive index $n_\mathrm{eff} = n_\mathrm{f}\sin\theta$. The propagation constant β is defined as

$$\beta := k_z = k_0 n_\mathrm{eff} \,, \tag{6.3}$$

where $k_0 = |\mathbf{k}_0|$ is the wavevector of the incoming wave.

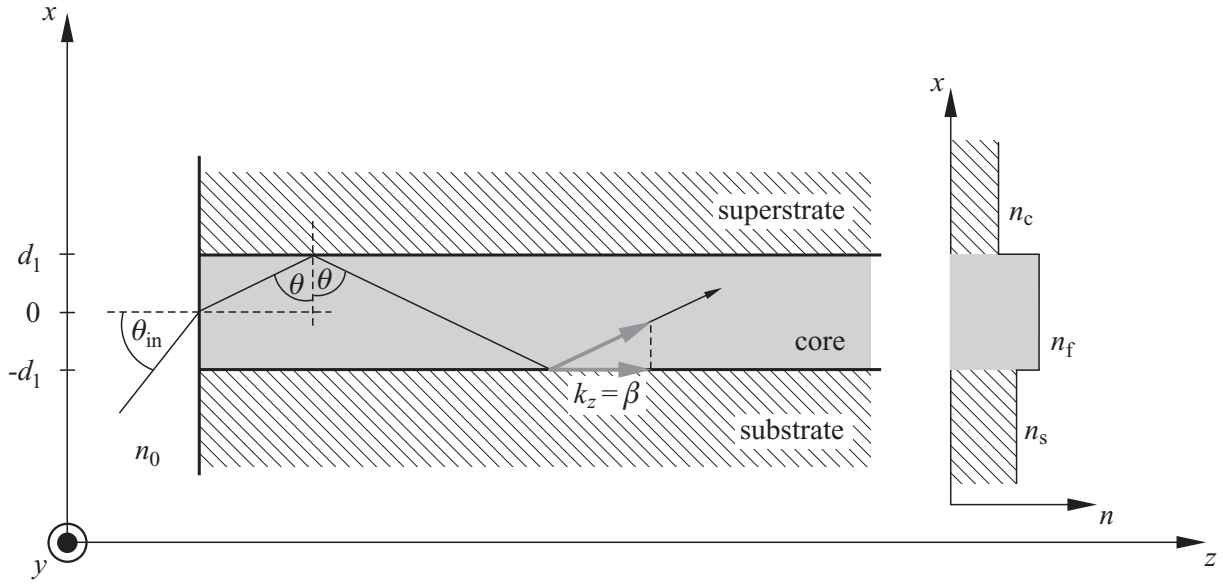

Figure 6.1: *3-layer waveguide in the ray-optical model*

For a correct treatment of waveguides with dimensions $2d_1 \approx \lambda$, where only a discrete number of modes is guided, the light has to be considered as an electromagnetic field instead of rays. Following the Maxwell equations,

$$\nabla \cdot \mathbf{B} = 0 \tag{6.4}$$

$$\nabla \times \mathbf{E} + \frac{\partial \mathbf{B}}{\partial t} = 0 \tag{6.5}$$

$$\nabla \cdot \mathbf{D} = \varrho \tag{6.6}$$

$$\nabla \times \mathbf{H} - \frac{\partial \mathbf{D}}{\partial t} = \mathbf{j} \tag{6.7}$$

where $\mathbf{E}$ and $\mathbf{B}$ are the electric and magnetic fields, respectively, $\mathbf{D}$ is the electric displacement vector, $\mathbf{H}$ is the magnetic flux density, and ϱ and $\mathbf{j}$ are the charge and current densities, respectively. Taking into account that for isotropic dielectric media $\mathbf{D} = \varepsilon\mathbf{E}$ and $\nabla \cdot \mathbf{E} = \varrho = 0$, the equation for propagating waves is

$$\triangle\mathbf{E} = \left(\frac{n}{c}\right)^2 \frac{\partial^2}{\partial t^2}\mathbf{E} \,. \tag{6.8}$$

The solution of equation 6.8 for a wave propagating in z-direction can be written as

$$\mathbf{E}(\mathbf{r}, t) = \mathbf{E}(x, y)\, e^{i(\omega t - \beta z)} \,, \tag{6.9}$$

which describes a wave travelling in z-direction. For the following discussion, only modes with transverse electric (TE) polarization (i. e. the polarization of the $\mathbf{E}$-field is parallel to the y-axis) will be considered; transverse magnetic (TM) solutions (where $\mathbf{H}$ is polarized along the y-direction) can be found analogously from the Maxwell equations.

6.1.1 Three-Layer Asymmetric Slab Waveguide

The complete mode description requires solutions of the wave equation in the different films of a waveguide structure. Considering a planar waveguide geometry as depicted in figure 6.1, i. e. infinite extension in y-direction, there is no y-dependence of the fields, $\partial E/\partial y = 0$, and equation 6.9 can be rewritten

$$\mathbf{E}(\mathbf{r}, t) = \mathbf{E}_y(x)\, e^{i(\omega t - \beta z)} \tag{6.10}$$

The electric field distribution in this slab waveguide structure is then obtained by combining equations 6.8 and 6.10 and exploiting the boundary conditions at the interfaces. As the transverse mode profile does not change by travelling along the z-direction, the value of $k_{z,p}$ has to be the same in all films.

The solutions for the electric fields in the three different regions correspond to an oscillating wave in the core and exponential decays in the substrate and superstrate, i. e.

$$\mathbf{E}_y(x,z) = \begin{cases} E_1\, e^{-\alpha_1 x}\, e^{-ik_z x} & x \geq \quad d_1 \\ \cos(kx + \psi)\, e^{-ik_z x} & -d_1 \leq x < \quad d_1 \\ E_5\, e^{\alpha_5 x}\, e^{-ik_z x} & x < \; -d_1\ . \end{cases} \tag{6.11}$$

In this equation E_1 and E_5 are the electric field amplitudes,

$$E_1 = \cos(kd_1 + \psi)\, e^{\alpha_1 d_1} \tag{6.12}$$

$$E_5 = \cos(-kd_1 + \psi)\, e^{-\alpha_5 d_1}\ , \tag{6.13}$$

α_1, α_5 and k are the wavenumbers,

$$\alpha_1 = k_0 \sqrt{n_{\text{eff}}^2 - n_{\text{c}}^2} \tag{6.14}$$

$$k = k_0 \sqrt{n_{\text{f}}^2 - n_{\text{eff}}^2} \tag{6.15}$$

$$\alpha_5 = k_0 \sqrt{n_{\text{eff}}^2 - n_{\text{s}}^2}\ , \tag{6.16}$$

and ψ is a phase offset. Due to the continuity condition of $\partial E_y/\partial x$ at the interfaces $x = \pm d_1$, the phase ψ can be eliminated and one gets the so-called *mode guidance condition equation* for a mode number p,

$$2kd_1 - \arctan\frac{\alpha_1}{k} - \arctan\frac{\alpha_5}{k} = p\,\pi\ . \tag{6.17}$$

All wave numbers k and α_m can be deduced by solving this equation for each n_{eff} of a particular mode p, and the intensity profile of each mode can be plotted ($I \propto |\mathbf{E}|^2$). An important result following from equation 6.17 is the fact that in an asymmetric waveguide the fundamental mode, TE_0, requires a minimum layer thickness, $d_{\text{min}}^{TE_0}$, otherwise no guiding is possible. For pure single-mode guiding of TE_0, the maximum layer thickness is limited, too, i. e $d_{\text{min}}^{TE_0} < d < d_{\text{max}}^{TE_0}$. Thus, single-mode guiding of light with wavelength $\lambda = 1\,\mu\text{m}$ in the system $Al_2O_3 - Y_2O_3 - \alpha$-$Al_2O_3$ requires a thickness of the core of 200 nm – 950 nm.

6.2 Yttria Waveguide

As shown in the previous section, the difference of refractive indices of the used materials is important for the guiding mechanism. Thus, waveguiding in sesquioxide films prepared on alumina substrates should be possible, because their refractive indices are higher than that of Al_2O_3. Due to the hexagonal structure, Al_2O_3 offers two different refractive indices: the ordinary ($n_o \perp c$) and the extraordinary ($n_e \parallel c$) refractive index. For epitaxial film growth it is necessary to use c-cut alumina substrates, i. e. (0001) α-Al_2O_3, to obtain lattice matching between film and substrate (see chapters 2 and 3). Thus, guided TE modes experience the ordinary refractive index n_o of Al_2O_3, while guided TM modes, which are polarized parallel to the c-axis of alumina, experience the extraordinary refractive index n_e.

The wavelength dependence of the refractive index is represented by the Sellmeier equations. The corresponding equations for Y_2O_3, Lu_2O_3, Sc_2O_3, and Al_2O_3 are summarized in table 6.1, and their graphical representation is shown in figure 6.2.

Y_2O_3	n^2	$=$	$3.5387 + \dfrac{0.0422}{\lambda^2 - 0.0243} - 0.0091\,\lambda^2$
Lu_2O_3	n^2	$=$	$3.6200 + \dfrac{0.0413}{\lambda^2 - 0.0239} - 0.0086\,\lambda^2$
Sc_2O_3	n^2	$=$	$3.8325 + \dfrac{0.0493}{\lambda^2 - 0.0238} - 0.0141\,\lambda^2$
Al_2O_3	n_o^2	$=$	$1.5586 + \dfrac{1.5237\,\lambda^2}{\lambda^2 - 0.0110} + \dfrac{5.3604\,\lambda^2}{\lambda^2 - 325.66}$
	n_e^2	$=$	$1.7811 + \dfrac{1.2762\,\lambda^2}{\lambda^2 - 0.0124} + \dfrac{0.3394\,\lambda^2}{\lambda^2 - 17.03}$

Table 6.1: *Sellmeier equations for the sesquioxides as well as for alumina. The unit for λ is μm* [Hel98].

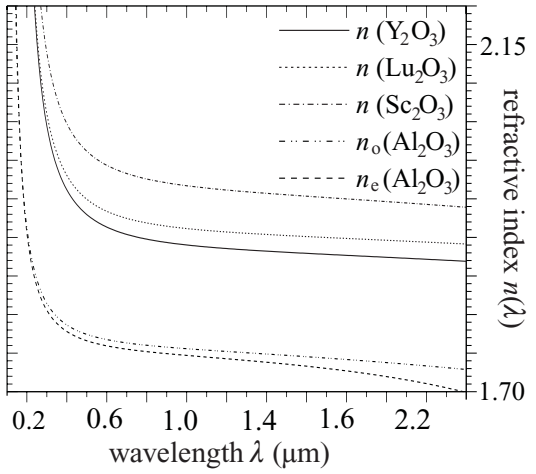

Figure 6.2: *Refractive indices of the used materials.*

Up to now, only a few attempts to fabricate yttria waveguides have been reported in the literature, e. g. guiding experiments in undoped Y_2O_3 films [Zha98] and in Er:Y_2O_3 on sapphire [Kor01, Lec02].

6.2.1 Waveguide Preparation

Two yttria waveguides were prepared on α-Al_2O_3. The Eu-doped Y_2O_3 waveguide with a film thickness of 1 µm was grown by electron beam evaporation (EBV) and then covered with an amorphous alumina film with a thickness of 1 µm. Since the film growth occurred at room temperature, the yttria film is also amorphous. The second waveguide consists

of a crystalline, 800 nm thick Nd:Y_2O_3 film prepared by PLD covered with an amorphous Al_2O_3 layer of 250 nm thickness. The dimension of the waveguides, i. e. a film thickness $d = 1\,\mu m$, was chosen in order to find a compromise between efficient incoupling of the light and single mode guiding. For a film thickness of 1 µm, the mode guidance condition predicts only small contributions of the 1st order mode.

The endfaces of the waveguide structures were polished with different diamond suspensions having grain sizes down to 0.5 µm. After polishing, the surfaces of the endfaces were investigated using an optical microscope. In general, the surfaces of both waveguides are smooth and show no large defects, as can be seen in figure 6.3 (a). However, in some regions close to the endfaces, the yttria film fabricated by EBV and the alumina cover layer is partially removed (figure 6.3 (b)). Top-view investigations of the film show an even, smooth surface. There are two reasons for the mechanical instability of the film: On the one hand, the film is grown by EBV at room temperature. The particles hit the substrate surface with low kinetic energies, resulting in an amorphous film with low surface adhesion. Due to the mechanical forces acting on the films during polishing, the film loses the adhesion and breaks away. On the other hand, yttria has a lower hardness than alumina (Mohs hardness of 6.8 compared to 9.0). As the films were polished using a diamond suspension, yttria is removed more easily than alumina. Both effects together lead to the poor endface quality presented in figure 6.3 (b). After polishing, the size of both waveguides was reduced to 7 mm × 10 mm. Thus, the length of the waveguides used in the following guiding experiments was 7 mm.

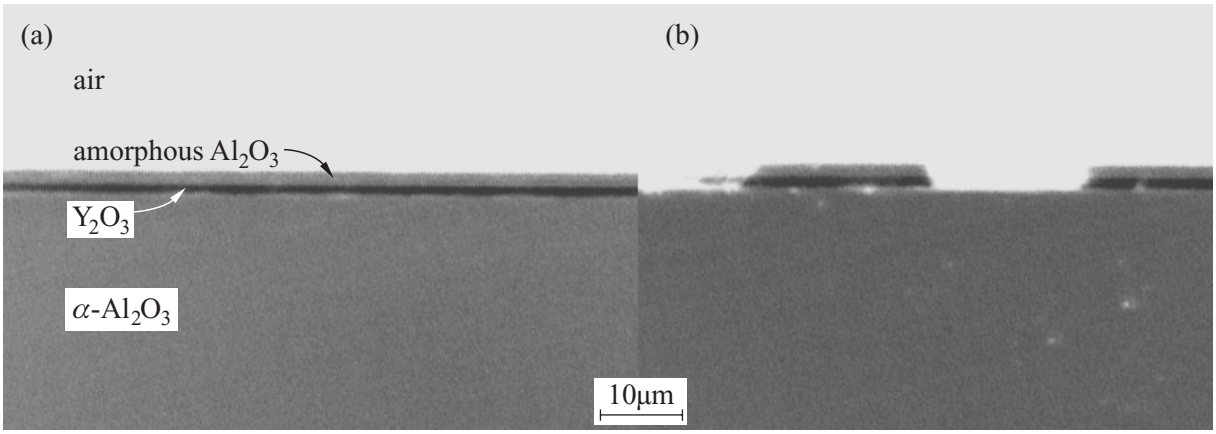

Figure 6.3: *Optical microscope picture of the polished waveguide endfaces: (a) upper part, (b) lower part of the sample with huge scratches at the endface.*

6.2.2 Waveguide Experiments

The waveguides were mounted on a precision manipulator with two translational and two angular adjustments with the endfaces perpendicular to the incoming light beam. The input and output optics were mounted on three-axis positioners. For guiding experiments, the light of a He-Ne-laser ($\lambda_{HeNe} = 632.8\,nm$) or an Ar-ion-laser ($\lambda_{Ar} = 512\,nm$) was

coupled into the waveguide via an optical fibre. The fibre was placed as close as possible to the waveguide endfaces (without getting in contact). The optimum launch position is achieved when the fringes of unlaunched pump light caused by a *Lloyd's mirror effect* are most widely separated. Using a microscope objective (40× magnification) at the end of the 7 mm long waveguide, the guided mode was projected either on a screen, a CCD camera or a powermeter.

An image of the resulting intensity distribution in the EBV-fabricated waveguide recorded by the CCD camera is presented in figure 6.4 (a). It can be seen that the output is nearly uniform along the y-direction. The measured intensity profile in the x-direction can be interpreted as the fundamental mode of the waveguide, because $|\mathbf{E}(TE_0)|^2 \propto I$ has the same structure. A comparison between the experimental result and the numerical simulation (solution of equation 6.11 for the TE_0 mode) is given in figure 6.4 (b). The curves of the simulation and the measurement match very good, except for a slight broadening in the lower intensity part of the measured curve. This can be explained by leaking of energy into the substrate as well as into the superstrate due to not well-defined interfaces. While theory predicts 94% of the intensity stored in the core, and only 4% and 2% in the substrate and superstrate, respectively, the experimental results shows that only 83% of the overall intensity is guided in the core. The remaining intensity is leaking into the substrate (10%) and superstrate (7%).

Surprisingly, no waveguiding could be observed in a PLD-fabricated 800 nm thick Nd:Y_2O_3 film covered with an Al_2O_3 layer of 250 nm thickness. However, this can be understood from the distribution of material deposited by PLD. Since there is a non-uniformity of the film thickness, as shown in chapter 4, the thickness of the waveguide at the endfaces is smaller than the maximum film thickness (800 nm) in the center of the film. Even if the thickness is large enough to allow single mode guiding, it is very difficult to launch light into the waveguide efficiently.

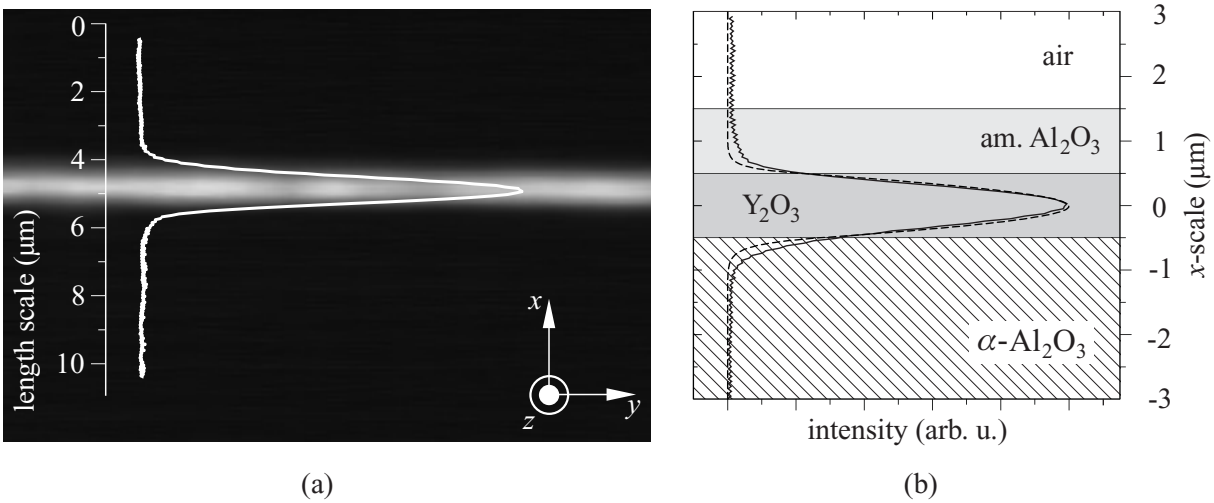

Figure 6.4: *(a) Waveguide intensity distribution ($\lambda = 514$ nm), (b) experimental mode intensity distribution (solid line) compared with the theoretical prediction (dashed line).*

6.2.3 Ridge Waveguide Simulations

In the previous section, the experimental realization of a planar Y_2O_3 waveguide has been demonstrated. However, even if one is able to produce perfect planar waveguides, this geometry has a tremendous disadvantage. Since a change of refractive index exists only in one direction, the confinement of light occurs only in this direction. In the other dimension, the propagation follows the traditional laws of optics in homogeneous media without significant restrictions resulting in a strong divergence. This problem can be solved by using a waveguide in stripe geometry leading to an additional spatial confinement of the guided light. The stripe with a refractive index higher than that of its surroundings can be embedded, buried or fabricated directly on top of the substrate. However, these waveguide types often suffer from additional stray losses because of missing precision and missing smoothness of the sidewalls. This disadvantage can be overcome with a ridge waveguide. In this case, the index change is achieved due to a stripe on top of the planar waveguide resulting in higher refractive indices for the modes propagating below this rib.

Thus, simulations of a planar Y_2O_3 waveguide with a rib of amorphous alumina have been performed. The structure is shown in figure 6.5. Amorphous alumina was chosen since it is easier to structure by etching techniques than the crystalline form α-Al_2O_3. The thickness of the active yttria layer was set to 1.5 µm resulting in a double-mode waveguide (see equation 6.17). The rib structure is characterized by an overlay of constant offset e with the rib of height h and width w on top of it. Calculations were performed with the commercially available software FimmWave (PhotoDesign Ltd.), which is a fully vectorial mode finder for 3D waveguide structures. In the following, the results of these simulations are summarized. At first, the guiding of the two lowest order modes, which was predicted by the mode guidance condition equation 6.17, has been proven. From a geometrical point of view, strong confinement of these modes is only obtained if $e = 0$, i. e. no overlay on top of the Y_2O_3-layer except the rib of width w. The effect is depicted in figure 6.6. In both

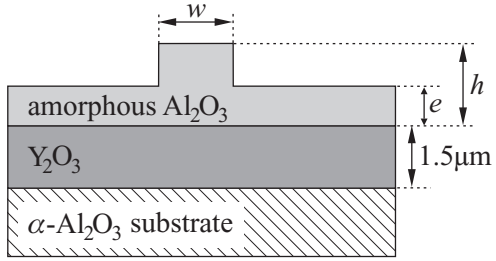

Figure 6.5: *Definition of a ridge waveguide structure.*

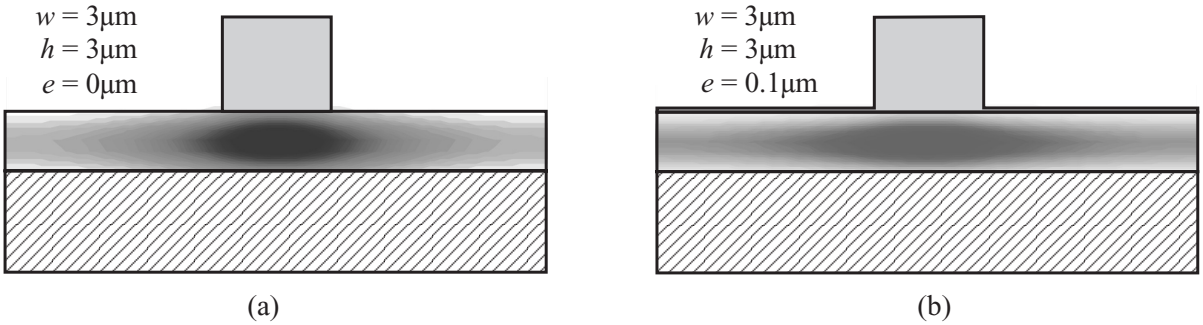

Figure 6.6: *Simulations of the intensity distribution at the endface of a 10 mm long rib waveguide structure. The material definitions and dimension are given in figure 6.5*

cases, the width and height of the rib are 3 µm. While there is no additional cover layer in figure (a), the simulation for an overlay of only 100 nm is presented in figure (b). It can bee seen, that in the first case, the intensity of the fundamental mode is strongly localized below the rib. In contrast, in the second case ($e = 0.1\,\mu\text{m}$), a lot of intensity extends in the y-direction, and thus is lost perpendicular to the propagation direction. While varying the height of the rib ($h = 1\,\mu\text{m}, 2\,\mu\text{m}, 3\,\mu\text{m}$) for $e = 0$ shows that the parameter h does not play a significant role for the mode confinement, the widths of the ribs influence the confinement and the mode propagation. Simulations for widths of $w = 3\,\mu\text{m}, 5\,\mu\text{m}$, and 7 µm indicate a double-mode system only for the 3 µm and 5 µm wide ribs. For a rib width of 7 µm, there are additional modes propagating.

Thus, the results obtained by the simulations clearly show that is possible to achieve guiding in an yttria ridge waveguide.

6.3 Photonic Crystals

This section deals with the relatively new field of photonic crystals which gained more and more interest in the last few years, because the propagation of photons can be controlled easily by a periodic arrangement of refractive index variations. It is the optical analogon of an electronic semiconductor.

The idea of controlling radiation by different materials goes back to 1946 when Purcell [Pur46] predicted that spontaneous emission at radio frequencies could be modified by the surrounding environment. For optical frequencies this effect was first studied by Yablonovitch [Yab87] and John [Joh87] in 1987 leading to structures commonly known as photonic bandgap materials. An overview about this new class of materials and their properties can be found in the literature [Joa95, Sak01].

The basic principle of a photonic crystal is rather simple as only a structure with periodically modulated refractive index is required. Thus, for a theoretical description of photonic crystals one can take benefit of the fundamental analogy between photonic crystals and conventional crystals: waves in periodic potentials. As a consequence, it is possible to treat the photonic and electronic cases with similar approaches. The arrangement of the atomic potentials in a regular crystal affects the wave functions of electrons resulting in a range of allowed energies and a band structure characterized by an energy gap. In the same way, photons react to the periodic refractive index contrast, which takes up the role of the atomic potentials for the photons, and causes the formation of photonic bands. In analogy to bandgaps in ordinary crystals, there appears a frequency range where no electromagnetic eigenmodes exist, the so-called *photonic bandgap*. By introducing a defect into this regular structure, modes appear whose eigenfunctions are strongly localized around the defect. These modes are called *localized defect modes*. For example, a point defect could act as a microcavity and a line defect corresponds to a 'classical' waveguide. While the spontaneous emission of a photon from an excited state is completely forbidden inside the bandgap, the spontaneous emission is accelerated if the emission frequency coincides with the eigenfrequency of the localized mode and the emitting atom is located in the defect.

This unique approach to control light using photonic crystals enables advances in optoelectronic applications not only by miniaturization but also by creating new devices like superprisms, which are highly dispersive [Kos98, Kra03], or materials with a 'negative' refractive index [Mar03]. Furthermore, the idea of photonic crystals has also being exploited in the technology of optical fibres, termed photonic crystal fibres (PCF) [Kni98, Rus03].

The periodic variation of the refractive index leads to a discrete translational symmetry in photonic crystals. This symmetry is described by a dielectric function $\varepsilon(\mathbf{r})$, which is a periodic function of $\mathbf{r}$, i. e. $\varepsilon(\mathbf{r}) = \varepsilon(\mathbf{r} + \mathbf{R})$, where $\mathbf{R}$ is an integral multiple of a primitive lattice vector $\mathbf{a}$. The following discussion is restricted to a mixed low-loss dielectric medium ($\varepsilon \in \mathbb{R}$) with no free charges or currents ($\varrho = 0, \mathbf{j} = 0$). Due to the linearity of the Maxwell equations, the time dependence can be separated by expanding the $\mathbf{E}$-field and the $\mathbf{H}$-field into a set of harmonic modes. Decoupling of the Maxwell

equations (see p. 94) results in an eigenvalue problem

$$\nabla \times \frac{1}{\varepsilon(\mathbf{r})} \nabla \times \mathbf{H}(\mathbf{r}) = \frac{\omega^2}{c^2} \mathbf{H}(\mathbf{r}) \tag{6.18}$$

depending entirely on $\mathbf{H}(\mathbf{r})$. The solutions of this eigenvalue problem are eigenfunctions $\mathbf{H}(\mathbf{r})$ of the hermite operator $\nabla \times \varepsilon^{-1}(\mathbf{r}) \nabla \times$ to the eigenvalue ω^2/c^2. Analogously to the electronic eigenstates in a semiconductor described by Bloch's theorem (Bloch states), the eigenmodes in a photonic crystal can thus be written as

$$\mathbf{H}_\mathbf{k}(\mathbf{r}) = \mathbf{u}_\mathbf{k}(\mathbf{r})\, e^{i\mathbf{k}\cdot\mathbf{r}} \,, \tag{6.19}$$

where $\mathbf{u}_\mathbf{k}(\mathbf{r}) = \mathbf{u}_\mathbf{k}(\mathbf{r} + \mathbf{R})$ is a periodic function for all lattice vectors $\mathbf{R}$. Inserting expression 6.19 in equation 6.18 results in

$$(i\mathbf{k} + \nabla) \times \left(\frac{1}{\varepsilon(\mathbf{r})} (i\mathbf{k} + \nabla \times \mathbf{u}_\mathbf{k}(\mathbf{r})) \right) = \frac{\omega^2}{c^2} \mathbf{u}_\mathbf{k}(\mathbf{r}) \tag{6.20}$$

For each value of $\mathbf{k}$, an infinite set of modes with discretely spaced frequencies can be found. The modes of each set are then labelled with the band index n forming a family of continuous functions $\omega_n(\mathbf{k})$, which is usually called the band structure of the photonic crystal.

As efficient waveguiding in photonic crystals is possible due to introducing a line defect, the question arises if this is also a proper way of fabricating dielectric oxide waveguides. For that reason, band structure calculations for the Y_2O_3–Al_2O_3 system have been carried out, in order to find out, if the sesquioxides are suitable for photonic waveguides. For these calculations the freely available software MIT Photonic-Bands by S. G. Johnson from the Massachusetts Institute of Technology (MIT) was used. The simulation is based on a 2D photonic crystal composed of a regular square array of circular air cylinders with radius r in Y_2O_3. The distance between the air cylinders is the lattice constant a of the photonic crystal. A scheme of this structure in real space as well as the Brillouin zone with points of high symmetry is presented as inset in figure 6.7.

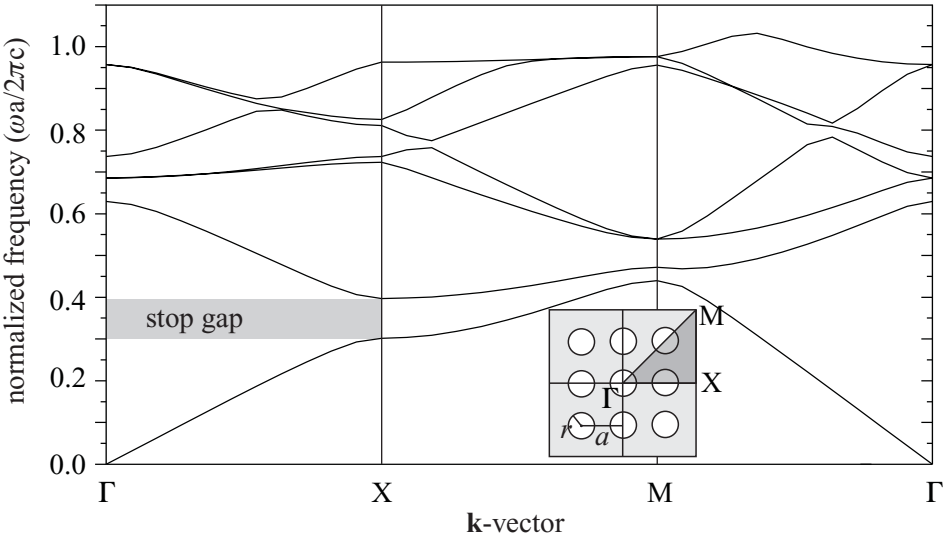

Figure 6.7: *Photonic band structure of a 2D photonic crystal*

As the photonic structure of yttria is on an alumina substrate, the dielectric constant was set to $\varepsilon = 3.511$, which corresponds to an effective refractive index of $n_{\text{eff}} = \sqrt{\varepsilon} = 1.874$. The ratio of the radius of the cylinder r to the lattice constant a is 0.38. It can bee seen in figure 6.7 that a stop gap appears along the Γ–X-direction in the frequency range $0.3 < \omega a/2\pi c < 0.4$. As a consequence, electromagnetic waves with frequencies within this range cannot propagate along the Γ–X-direction.

If a number of rows is left out, a line defect is created and eigenstates within the bandgap are allowed, i. e. the localized defect modes can propagate. Thus, additional guiding in the lateral direction is achieved. Figure 6.8 shows a simulation of a waveguide obtained by three missing rows of air cylinders. The main problems in a realization of such a waveguide structure are the small lattice constant and the small hole diameter required to form the bandgap. For a wavelength of 1 µm to propagate the lattice constant a has to be in the range of 300 nm to 400 nm corresponding to hole diameters between 230 nm and 300 nm.

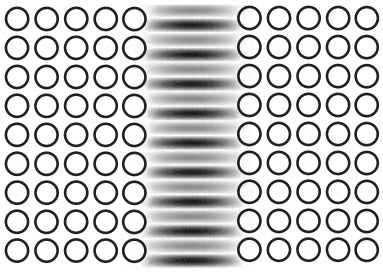

Figure 6.8: *Waveguide based on a photonic crystal*

The methods for fabricating these structures by etching techniques exist already, but up to now they have been successfully applied only to semiconductors and polymers.

In addition to etching techniques applied to obtain the photonic structure, self-assembling of colloidal suspensions of spherical polystyrene or silica particles can be used to create templates (so-called opal structure). After the spaces between the spheres are filled with a high-refractive-index material, the spheres are removed leaving a high-refractive-index matrix with periodic air voids.

Using this technique, first photonic crystals based on Y_2O_3 have been fabricated [Wit03]. The opal structure infilled with green emitting cubic Tb:Y_2O_3 phosphor yields a stop band position of 559 nm. Due to this stop band, the emission intensity in the green is strongly modulated under UV excitation.

7 Conclusions

7.1 Summary of Results

The subject of the present work was the preparation and characterization of crystalline rare-earth-doped sesquioxide films for optical applications, such as crystalline waveguides and optical coatings. This chapter summarizes the work that has has been described in this thesis: definition of the film and the substrate materials, the film preparation by pulsed laser deposition, the investigation of the films by different analytical tools, and finally the fabrication of an yttria waveguide. Additionally, an outlook to future work that would logically follow from this work is presented.

Definition of Film–Substrate System

The preparation of thin sesquioxide films was aimed because this class of materials offer a number of advantageous mechanical and thermal properties (e. g. high melting point, large hardness, low phonon energies, large thermal conductivity), which makes them favorable for new integrated optic devices. Sesquioxides are already well-known hosts for rare earth doped luminescent materials (e. g. Eu:Y_2O_3 as red phosphor) and solid state lasers (e. g. Yb:Y_2O_3, Tm:Sc_2O_3), and in combination with thin film technology an improvement of these devices can be envisioned, too.

A proper substrate for sesquioxide films is α-Al_2O_3, because it offers a a lattice constant that nearly matches that of cubic Y_2O_3 in the $\langle 111 \rangle$ direction, which is important for epitaxial film growth. For $\langle 111 \rangle$ grown Y_2O_3 on (0001) α-Al_2O_3 this mismatch is 4.8%. The lattice mismatch of Lu_2O_3 and Sc_2O_3 are 2.8% and -2.5%, respectively leading to the production of films with less dislocations. Since the refractive index of α-Al_2O_3 is lower than that of the sesquioxides, waveguiding in the RE_2O_3 films should be possible. In addition, α-Al_2O_3 has a high thermal conductivity, which is of the same order of that of the sesquioxides Thus, the RE_2O_3–Al_2O_3 system becomes interesting for the realization of waveguide lasers because of an efficient heat transfer from the active layer to the heat sink via the substrate.

Preparation

The sesquioxide films were fabricated by the pulsed laser deposition technique. The targets used in the presented ablation experiments were either pressed and sintered sesquioxide

powders or sesquioxide single crystals. After the sintering process at 1700℃, the density of the pellets was about 90% of the single crystal density. In practice, no difference in the ablation behavior and the resulting film structure have been observed when different types of targets were used.

Using an ArF excimer laser with a wavelength of 193 nm and a pulse duration of 15 ns, the targets were irradiated with laser fluences between between 2 J/cm^2 and 4 J/cm^2, depending on the material, resulting in growth rates of about 0.1 Å per pulse. The threshold fluence necessary for ablation from sintered Y_2O_3 targets upon nanosecond laser irradiation at 193 nm was determined to be around 0.35 J/cm^2. At optimum growth conditions (substrate temperature of 700℃ and partial oxygen pressure of 5×10^{-2} mbar) crystalline film growth was achieved.

Structural Characterization

The characterization of the thin films was carried out by applying a number of analytical techniques. The structural characterization includes X-ray diffraction (XRD), surface X-ray diffraction (SXRD), Rutherford backscattering (RBS) and atomic force microscopy (AFM).

The results of the XRD and SXRD measurements on thick yttria films (500 nm) indicate a highly textured film growth along the ⟨111⟩ direction. This is in good agreement with the results obtained by RBS, where not only the correct stoichiometry could be proven but also epitaxial growth of Y_2O_3 on α-alumina was observed by the channeling effect. Additionally, the surface of a crystalline Y_2O_3-film with a thickness of 500 nm shows a regular nano-structure of pyramidally shaped crystallites, which are formed due to the ⟨111⟩ growth. This interpretation was evidenced by the similar structure of a {111} cleavage facet of yttria. The film surface morphologies of Lu_2O_3, Sc_2O_3, and $YScO_3$ show no clear geometrical structures. However, in these films the grains with in-plane dimensions up to 1.5 µm have a preferred orientation, and the thickness-dependent surface roughness is small (< 2.5 nm). In addition, no craters (possibly caused by droplets) or other irregularities have been observed on the film surfaces. These results are very promising as they indicate smooth surfaces which are important for optical applications.

In contrast, thin films with a thickness ≤ 100 nm do not show perfect crystalline growth. Using the method of SXRD, it was found that the films were indeed mainly textured along the ⟨111⟩ direction, but have also a polycrystalline component. In addition, there are two different domains forming the ⟨111⟩ texture. This twinning can be explained by the positions of the anions, which form a distorted cube and thus, the atoms forming the {111} planes create no equal-sided triangles.

An interesting result is obtained by AFM measurements on the surface of a 5 nm thick Y_2O_3 film. This film had no completely covered surface but showed 3D island growth. The shape of the single crystallites is triangular or quadrangular with at least one angle of either 60° or 120°, which is an indication of the ⟨111⟩ growth direction in the early stage of film growth. With this observation, the existence of twinning becomes more understandable, because the islands form independently of each other.

Optical Spectroscopy

Additional information about the rare-earth-doped sesquioxide films have been obtained by optical spectroscopy. These spectroscopic investigations were mainly focused on the Eu^{3+}-doped Y_2O_3 and Lu_2O_3-films, because europium is not only a good luminescent probe emitting in the visible part of the spectrum but also because the energetic position of the main fluorescence level, $^5D_0$, reacts very sensitive to the surrounding crystal field (since $J = 0$, i. e. no Stark splitting occurs).

The luminescence characteristics of the dopants depend strongly on the crystallinity of the host matrix, which is directly connected to the substrate temperature during the film growth. Thus, with decreasing substrate temperature the films contain an increasing amorphous component. This amorphous character at low substrate temperatures was also observed in the luminescence spectra. In contrast, the ambient gas pressure had no significant influence on the luminescence behavior, even though it influences the crystallinity, too. But as low substrate temperatures lead to amorphous films, the variations in gas pressure lead to a more polycrystalline structure of the films, where a long-range order in the matrix is given, resulting in unchanged luminescence.

Films down to a thickness of 100 nm show the same luminescence behavior as the corresponding bulk material. The significant change in luminescence when the film thickness is decreased further can be explained by a phase change of the material. Due to subplantation and interdiffusion of, for example, Y_2O_3 into the Al_2O_3 matrix, a new phase can evolve, e. g. $YAlO_3$ or $Y_3Al_5O_{12}$. This hypothesis is based on the results obtained by VUV excitation measurements indicating strong band-to-band transitions starting at 8.26 eV, which corresponds to the bandgap energy of $Y_3Al_5O_{12}$.

It is believed that the subplantation, caused by high-energy particles in the plasma plume, is related to the short target–substrate distance. The kinetic energies could be reduced by a higher ambient gas pressure. However, on the other hand this leads to non-stoichiometric film compositions.

Additionally, surface effects might play an important role, because the presented thin films are not closed films by means of a completely covered substrate surface, but single 3D islands. Due to a large surface-to-volume ratio of these islands, the number of defects, such as unsaturated bonds or varying bond lengths, which have a significant influence on the spectroscopic behavior, is strongly increased compared to defects on a flat surface.

Waveguides

For possible applications in integrated optics, waveguide experiments on the system Y_2O_3–Al_2O_3 have been performed, and single-mode guiding of the fundamental mode was demonstrated. Simulations of a ridge waveguide based on this system allowed an optimization of the waveguide structure resulting in a reduced loss of energy compared to pure planar waveguides. In addition, photonic band structure calculations for the Y_2O_3–Al_2O_3 system have shown, that the sesquioxides are also suitable for photonic crystal waveguide structures.

7.2 Résumé

The aim of the research detailed in this thesis has been to show that PLD is an efficient technique for fabrication thin sesquioxide films for optical applications, such as coatings, bragg mirrors, waveguides and crystalline waveguide lasers. From the results presented here, it can be concluded that using PLD, films with the desired specifications (correct stoichiometry, crystallinity, smooth surface) can be produced.

Although the thin films produced are by no means perfect, as indicated by X-ray diffraction measurements and the optical spectroscopy, it is likely that these deficiencies are not intrinsic to the technique of PLD and can be ruled out through further work on the specific deposition process parameters. Within this context, an important result for ongoing experiments on the fabrication of thin films by PLD are the strong subplantation effects when high-energy particles strike the substrate. Even if species with high kinetic energies are favorable for crystalline growth, one has to find a compromise between the desired growth mode and destructive effects.

7.3 Outlook and Future Work

The questions left open in this thesis can partly be answered by different theoretical and analytical techniques.

By numerical calculation of the energy level positions using crystal field theory, a qualitative description of the luminescence behavior is obtained and can be used for the discussion of the measured spectra.

As it is obvious that the interface region between substrate and film plays an important role, one has to find tools which are capable of investigating this small region. In addition to SXRD and RBS, two other techniques have to be mentioned, which - up to now - have not been applied to the fabricated thin sesquioxide films. These are the methods of TEM (Transmission Electron Microscopy) and EXAFS (Extended X-ray Absorption Fine Structure) analysis. While TEM allows a direct view of the atomic positions at the interface and - in combination with a Z-number-dependence resolution - the identification of the different components [Gao99, Top01], the influence of the interface and surface on the bond length can be investigated by EXAFS in more detail, as already demonstrated by [Qi02].

Using a SNOM (Scanning Near-field Optical Microscope) instead of an AFM, not only the surface topography can be recorded, but also single islands of rare-earth-doped crystallites can be investigated spectroscopically. This characterization technique rules out the statistic component of conventional spectroscopy and allows to study the influence of surface effects on individual atoms. In fact, these islands can act as 'nanocrystal cages' for the rare-earth-ions. This confinement of a single atom (*Quantum Confined Atom*) within a nanocrystal offers the chance to studying fundamental physics on single atoms.

However, with respect to possible applications, like gate dielectrics or waveguides, a two-

dimensional layer-by-layer growth would be advantageous instead of the three-dimensional island growth, because the interface region would become much smoother. To avoid the formation of islands, Blank et al. used the approach of *pulsed laser interval deposition*, a periodic deposition sequence, where the fast deposition of the amount of material necessary to grow a monolayer is followed by an interval in which no deposition takes place and the atoms can form a complete layer [Bla99]. This process requires the technique of in-situ RHEED (Reflection High Energy Electron Diffraction) to have a precise control of the film thickness. In future PLD experiments this technique will be applied to control the growth of RE_2O_3 films.

Additionally, one has to find the optimum kinetic energies of the plume species in order to minimize surface destruction. This can be achieved, for example, by using particles at thermal speed. The activation energy for crystalline film growth is then provided only by substrate heating.

Different lattice constants of film and substrate materials will also lead to mismatch-induced defects. However, as already demonstrated in our laboratory by L. Rabisch, in EBV-fabricated films 'perfect' lattice matching with respect to the sapphire substrate can be obtained using a mixed system of $LuScO_3$. In addition to α-alumina, there are other potential candidates for substrates, for example SiO_2. The system Sc_2O_3/SiO_2 (α-cristobalite) has a lattice mismatch of only 0.7%. Using SiO_2 (α-tridymite) the lattice mismatch for Lu_2O_3 is only 0.2%. For that reason, first experiments using these systems are currently running.

In addition to the fundamental aspects of film formation and growth, the main challenge is the fabrication of functional devices, such as waveguide structures or crystalline bragg mirrors directly grown on laser crystals. Based on the simulations, one of the next steps in our laboratory will be the realization of an yttria ridge waveguide, where the radiation is not only guided in the vertical but also in the lateral direction by a rib structure.

A Energy levels of Eu^{3+} in Y_2O_3

Data for the C_2-site are taken from [Cha82], whereas the positions for the C_{3i} can be found in [Gru85, Heb70]. For the $^7F_{3,4,5,6}$ manifolds in C_{3i} sites there are no experimental data availiable.

C_2-site	
$^7F_0$:	0
$^7F_1$:	199, 360, 543
$^7F_2$:	859, 906, 949, [1226], 1380
$^7F_3$:	1847, 1867, 1907, [1946], 2021, 2130, 2160
$^7F_4$:	2669, 2800, 2846, 3014, 3080, 3119, 3163, 3178, 3190
$^7F_5$:	3755, [3785], 3825, [3888], 3904, 3938, 4015, 4127, [4211], 4227, [4248]
$^7F_6$:	4791, 4812, 5032, [5038], 5045, [5038], 5045, [5073], 5271, [5300], 5314, [5445], 5459, [5634], 5636
$^5D_0$:	17216
$^5D_1$:	18930, 18954, 18992
$^5D_2$:	21355, 21367, 21394, 21487, 21503
$^5D_3$:	24258, 24267, 24284, [24293], [24302], (24330), 24354

C_{3i}-site	
$^7F_0$:	0
$^7F_1$:	132, 429
$^7F_2$:	827, 948, 1188
$^5D_0$:	17302
$^5D_1$:	18991, 19080

B List of Fabricated Films

The following table lists all film which were fabricated during the course of this thesis.

name	film	substrate	ν_{rep} (Hz)	E_{Laser} (mJ)	$P(O_2)$ (mbar)	T (℃)	d (nm)
17.10.01.14	Eu(1.5%):Y_2O_3	Al_2O_3	10	200	1×10^{-2}	700	500
18.10.02.16	Eu(1.5%):Y_2O_3	Al_2O_3	10	185	1×10^{-2}	700	500
22.10.02.17	Eu(1.5%):Y_2O_3	Al_2O_3	10	185	1×10^{-1}	653	500
22.10.02.19	Eu(1.5%):Y_2O_3	Al_2O_3	10	185	5×10^{-2}	692	500
23.10.02.20	Eu(1.5%):Y_2O_3	Al_2O_3	10	185	5×10^{-1}	684	500
24.10.01.23	Eu(1.5%):Y_2O_3	Al_2O_3	10	185	4×10^{-3}	663	500
25.10.02.24	Eu(1.5%):Y_2O_3	Al_2O_3	10	185	5×10^{-2}	550	500
25.10.02.25	Eu(1.5%):Y_2O_3	Al_2O_3	10	185	5×10^{-2}	600	500
28.10.02.27	Eu(1.5%):Y_2O_3	Al_2O_3	10	185	5×10^{-2}	650	500
29.10.01.28	Eu(1.5%):Y_2O_3	Al_2O_3	10	185	5×10^{-2}	700	500
29.10.08.29	Eu(1.5%):Lu_2O_3	Al_2O_3	10	185	5×10^{-2}	700	500
30.10.01.30	Eu(1.5%):Y_2O_3	Al_2O_3	10	250	5×10^{-2}	700	500
13.11.03.31	Eu(4%):Y_2O_3	Al_2O_3	10	185	5×10^{-2}	700	500
29.01.03.33	Eu(1.5%):Y_2O_3	Al_2O_3	10	185	5×10^{-2}	20	500
28.01.03.34	Eu(1.5%):Y_2O_3	Al_2O_3	10	185	5×10^{-2}	300	500
28.01.03.35	Eu(4%):Y_2O_3	Al_2O_3	10	185	5×10^{-2}	685	100
29.01.03.36	Eu(4%):Y_2O_3	Al_2O_3	10	185	5×10^{-2}	685	20
29.01.03.37	Eu(4%):Y_2O_3	Al_2O_3	10	185	5×10^{-2}	685	5
29.01.03.38	Eu(4%):Y_2O_3	Al_2O_3	10	185	5×10^{-2}	685	5
30.01.03.39	Eu(4%):Y_2O_3	Al_2O_3	10	185	5×10^{-2}	685	1
30.01.03.40	Eu(4%):Y_2O_3	Si	10	185	5×10^{-2}	600	250
30.01.03.41	Er(1%):Y_2O_3	Al_2O_3	10	185	5×10^{-2}	685	20
30.01.03.42	Er(1%):Y_2O_3	Si	10	185	5×10^{-2}	580	240
31.01.03.43	Er(1%):Y_2O_3	Al_2O_3	10	185	5×10^{-2}	685	20
31.01.09.44	Eu(4%):Lu_2O_3	Si	10	165	5×10^{-2}	655	400
31.01.09.45	Eu(4%):Lu_2O_3	Al_2O_3	10	165	5×10^{-2}	685	100
01.02.09.46	Eu(4%):Lu_2O_3	Al_2O_3	10	165	5×10^{-2}	685	20
01.02.09.47	Eu(4%):Lu_2O_3	Al_2O_3	10	165	5×10^{-2}	685	5
02.02.09.48	Eu(4%):Lu_2O_3	Al_2O_3	10	165	5×10^{-2}	685	1
02.02.40.49	Nd(0.5%):Lu_2O_3	Si	10	165	5×10^{-2}	20	
02.02.40.50	Nd(0.5%):Lu_2O_3	Al_2O_3	10	165	5×10^{-2}	685	20
03.02.40.51	Nd(0.5%):Lu_2O_3	Al_2O_3	10	165	5×10^{-2}	685	5
03.02.41.52	Er(3%):Sc_2O_3	Si	10	165	5×10^{-2}	20	140
03.02.41.53	Er(3%):Sc_2O_3	Al_2O_3	10	165	5×10^{-2}	680	5
04.02.41.54	Er(3%):Sc_2O_3	Al_2O_3	10	165	5×10^{-2}	680	1
04.02.41.55	Er(3%):Sc_2O_3	Al_2O_3	10	165	5×10^{-2}	685	20
04.02.41.56	Er(3%):Sc_2O_3	Al_2O_3	10	165	5×10^{-2}	685	100
04.02.42.57	Nd(3%):Sc_2O_3	Si	10	165	5×10^{-2}	20	70
05.02.42.58	Nd(3%):Sc_2O_3	Al_2O_3	10	165	5×10^{-2}	680	750
05.02.42.59	Yb(2%):$YScO_3$	Al_2O_3	10	190	5×10^{-2}	675	1500 Pulse
06.02.42.60	Yb(2%):$YScO_3$	Al_2O_3	10	190	5×10^{-2}	675	800 Pulse
06.02.42.61	Yb(2%):$YScO_3$	Al_2O_3	10	190	5×10^{-2}	675	3000 Pulse
06.02.44.62	Nd(> 1%):$GdVO_4$	Al_2O_3	10	210	5×10^{-2}	680	~ 160 nm
07.02.44.63	Nd(> 1%):$GdVO_4$	Al_2O_3	10	205	5×10^{-2}	700	~ 80 nm
07.02.44.64	Nd(> 1%):$GdVO_4$	Al_2O_3	10	200	5×10^{-2}	690	~ 40 nm

Table B.1: *List of films*

C X-ray Diffraction Peaks of Y_2O_3

In the table below, the possible diffraction peaks for different (hkl)-planes of cubic Y_2O_3 in the 2θ-range 5° to 77° are listed. In addition, the corresponding inter-planar spacings d_{hkl} and the relative peak intensity is given.

h	k	l	2θ (deg)	d (Å)	I (rel.)	h	k	l	2θ (deg)	d (Å)	I (rel.)
2	0	0	16.717	5.2990	9.67	4	4	4	60.472	1.5297	196.08
2	1	1	20.511	4.3267	440.15	5	3	4	61.854	1.4988	31.62
2	2	0	23.727	3.7470	0.59	5	4	3	61.854	1.4988	50.94
2	2	2	29.166	3.0594	3816.38	6	4	0	63.218	1.4697	7.31
3	1	2	31.561	2.8325	15.14	6	0	4	63.218	1.4697	43.06
3	2	1	31.561	2.8325	4.17	5	5	2	64.567	1.4422	2.59
4	0	0	33.803	2.6495	984.78	6	3	3	64.567	1.4422	41.89
4	1	1	35.922	2.4980	195.19	7	2	1	64.567	1.4422	53.86
4	2	0	37.937	2.3698	27.92	7	1	2	64.567	1.4422	33.57
4	0	2	37.937	2.3698	14.97	6	2	4	65.900	1.4162	7.85
3	3	2	39.865	2.2595	220.32	6	4	2	65.900	1.4162	53.53
4	2	2	41.718	2.1633	35.23	6	1	5	69.822	1.3460	45.68
4	3	1	43.507	2.0785	149.75	6	5	1	69.822	1.3460	41.04
4	1	3	43.507	2.0785	180.08	7	3	2	69.822	1.3460	0.54
5	1	2	46.919	1.9349	55.58	7	2	3	69.822	1.3460	0.07
5	2	1	46.919	1.9349	49.07	8	0	0	71.107	1.3248	183.21
4	4	0	48.555	1.8735	1694.72	8	1	1	72.382	1.3045	68.96
4	3	3	50.151	1.8176	87.16	7	4	1	72.382	1.3045	25.95
6	0	0	51.710	1.7664	15.86	5	5	4	72.382	1.3045	24.83
4	4	2	51.710	1.7664	2.14	7	1	4	72.382	1.3045	31.40
5	2	3	53.237	1.7192	33.55	8	2	0	73.648	1.2852	36.61
5	3	2	53.237	1.7192	38.70	6	4	4	73.648	1.2852	20.25
6	1	1	53.237	1.7192	134.49	8	0	2	73.648	1.2852	23.28
6	0	2	54.734	1.6757	27.45	6	5	3	74.906	1.2667	44.71
6	2	0	54.734	1.6757	17.92	6	3	5	74.906	1.2667	44.22
5	4	1	56.203	1.6353	71.85	6	6	0	76.156	1.2490	0.48
5	1	4	56.203	1.6353	92.63	8	2	2	76.156	1.2490	45.78
6	2	2	57.648	1.5977	1161.69	7	4	3	77.400	1.2320	26.86
6	1	3	59.070	1.5626	127.41	7	3	4	77.400	1.2320	26.17
6	3	1	59.070	1.5626	119.23	8	1	3	77.400	1.2320	39.81

Table C.1: *2θ-positions of X-ray diffraction peaks of cubic Y_2O_3*

Bibliography

[Abr78] V. N. Abramov and A. I. Kuznetsnov. *Fundamental absorption of Y_2O_3 and $YAlO_3$*. Soviet Physics of Solid State **20** (3), 399 (1978).

[Abr83] V. N. Abramov, A. N. Ermoshkin and A. I. Kuznetsnov. *Optical properties and electron energy structure of Y_2O_3 and Sc_2O_3*. Soviet Physics of Solid State **25** (6), 981 (1983).

[And94] A. Andreeva, A. Sisonyuk and E. Himich. *Growth Conditions and Dielectric Properties of Yttrium Oxide Thin Films*. Physica Status Solidi (a) **145**, 441 (1994).

[And98] A. A. Anderson. *Crystalline planar waveguide lasers fabricated by pulsed laser deposition*. Dissertation, Faculty of Science, Department of Physics, University of Southampton (1998).

[Ani83] S. I. Anisimov, Y. B. Zel'dovich, N. A. Inogamov and M. F. Ivanov. *Shock Waves, Explosions, and Detonations*. In: *Progress in Astronautics and Aeronautics, Series 87*, 218 (Washington, DC, 1983).

[Ars80] P. A. Arsenjew, C. S. Bagdasarow, K. Bienert, E. F. Kustow and A. W. Potjomkin. *Kristalle in der modernen Lasertechnik* (Akademische Verlagsgesellschaft Geest & Portig K.-G., Leipzig, 1980).

[Ash76] N. W. Ashcroft and N. D. Mermin. *Solid State Physics* (Saunders College Publishing, Fort Worth, 1976).

[Auc88] O. Auciello, A. R. Krauss, J. Santiago-Aviles, A. F. Schreiner and D. M. Gruen. *Surface compositional and topographical changes resulting from excimer laser impacting on $YBa_2Cu_3O_2$ single phase superconductors*. Applied Physics Letters **52** (3), 239 (1988).

[Bal62] C. J. Ballhausen. *Introduction to Ligand Field Theory* (McGraw-Hill Book Company, Inc., New York, 1962).

[Bar69] W. P. Barr. *The production of low scattering dielectric mirrors using rotating vane particle filtration*. Journal of Physics E **2** (2), 1112 (1969).

[Bar00] M. D. Barnes, A. Mehta, T. Thundat, R. N. Bhargava, V. Chhabra and B. Kulkarni. *On-Off Blinking and Multiple Bright States of single Europium IOns in Eu^{3+}:Y_2O_3 Nanocrystals*. Journal of Physical Chemistry B **104**, 6099 (2000).

[Bar01] S. J. Barrington. *Planar Waveguide Devices fabricated by Pulsed Laser Deposition*. Dissertation, Faculty of Science, Department of Physics, University of Southampton (2001).

[Bat82] I. P. Batra. *Electronic structure of α-Al_2O_3*. Journal of Physics: Condensed Matter **15**, 5399 (1982).

[Bau58] E. Bauer. *Wachstum dünner Schichten*. Zeitschrift für Kristallographie **110**, 372 (1958).

[Bec88] C. H. Becker and J. Pallix. *Laser ablation of bulk $YBa_2Cu_3O_{7-\delta}$ and cluster emission*. Journal of Applied Physics **64** (10), 5152 (1988).

[Ber74] H. Bergmann. *Gmelin Handbuch der Anorganischen Chemie, Seltenerdelemente, Teil C1* (Springer Verlag, Berlin, Heidelberg, New York, 1974).

[Bin86] G. Binning, C. Quate and C. Gerber. *Atomic Force Microscope*. Physical Review Letters **56** (9), 930 (1986).

[Bla99] D. H. A. Blank, G. Koster, G. Rijnders, E. van Setten, P. Slycke and H. Rogalla. *Imposed layer-by-layer growth by pulsed laser interval deposition*. Applied Physics A **69** (Supplement 1), S17 (1999).

[Bla04] D. H. A. Blank. *Controlled PLD growth of complex oxide thin films: Playing LEGO at an atomic scale*. Oral presentation, Institutskolloquium: Quantenoptik und Laserphysik, Institut für Laser-Physik, Hamburg (2004).

[Blo74] N. Bloembergen. *Laser-Induced Electric Breakdown in Solids*. IEEE Journal of Quantum Electronics **QE-10** (3), 375 (1974).

[Bün89] J.-C. G. Bünzli and G. R. Choppin. *Lanthanide Probes in Life, Chemical and Earth Sciences* (Elsevier Science Publishing Company Inc., New York, 1989).

[Bon00] C. L. Bonner. *Multi-watt, diode-pumped planar waveguide lasers*. Dissertation, Faculty of Science, Department of Physics, University Southampton (2000).

[Bor27] M. Born and J. R. Oppenheimer. *Zur Quantentheorie der Molekeln*. Annalen der Physik **84**, 457 (1927).

[Bor75] M. Born and E. Wolf. *Principles of Optics,* 5^{th} edition (Pergamon Press, Oxford, 1975).

[Bár57] C. Bárta, F. Petru and B. Hájek. *Über die Darstellung des Einkristalls von Scandiumoxyd*. Die Naturwissenschaften **45**, 36 (1957).

[Bra92] S. Brandt. *Datenanalyse,* 3. Auflage (BI Wissenschaftsverlag, Mannheim, 1992).

[Bre62] F. Breech and L. Cross. Applied Spectroscopy **16** (1962).

[Bäu00] D. Bäuerle. *Laser Processing and Chemistry* (Springer-Verlag, Berlin, Heidelberg, New York, 2000).

[Bul95] A. V. Bulgakov and N. M. Bulgakova. *Dynamics of laser-induced plume expansion into an ambient gas during film deposition.* Journal of Physics D: Applied Physics **28** (8), 1710 (1995).

[Bul98] A. V. Bulgakov and N. M. Bulgakova. *Gas-dynamic effects of the interaction between a pulsed laser-ablation plume and the ambient gas: analogy with an underepanded jet.* Journal of Physics D **31**, 693 (1998).

[Bun99] O. Bunk. *Bestimmung der Struktur komplexer Halbleiter-Oberflächenrekonstruktion mit Röntgenbeugung.* Dissertation, Fachbereich Physik, Universität Hamburg (1999).

[Bur62] G. Burns. *Shielding and Crystal Fields at Rare-Earth Ions.* Physical Review **128** (5), 2121 (1962).

[Bur02] P. B. W. Burmester. *Optisch aktive, kristalline, Selten-Erd-dotierte Y_2O_3-PLD-Schichten auf α-Al_2O_3.* Dissertation, Fachbereich Physik, Universität Hamburg (2002).

[Cha82] N. C. Chang, J. B. Gruber, R. P. Leavitt and C. A. Morrison. *Optical spectra, energy levels, and crystal-field analysis of tripositive rare earth ions in Y_2O_3. I. Kramers ions in C_2 sites.* Journal of Chemical Physics **76** (8), 3877 (1982).

[Che88] J. T. Cheung and H. Sankur. *Growth of thin films by laser-induced evaporation.* CRC Critical Reviews in Solid State and Material Sciences **14** (1), 63 (1988).

[Che01] R. Chety, E. Millon, A. Boudrioua, J. C. Loulergue, A. Dahoun and J. Perrière. *Growth of $GdCa_4O(BO_3)_3$ thin films by pulsed-laser deposition for nonlinear optical applications.* Journal of Materials Chemistry **11**, 657 (2001).

[Che02] X. Y. Chen, K. H. Wong, C. L. Mak, X. B. Yin, M. Wang, J. M. Liu and Z. G. Liu. *Selective growth of (100)-, (110)-, and (111)-orientated MgO films on Si(100) by pulsed laser deposition.* Journal of Applied Physics **91** (9), 5728 (2002).

[Cho97] K. G. Cho, D. Kumar, D. G. Lee, S. L. Jones, P. H. Holloway and R. K. Singh. *Improved luminescence properties of pulsed laser deposited Eu:Y_2O_3 thin films on diamond coated silicon substrates.* Applied Physics Letters **71** (23), 3335 (1997).

[Cho98] K. G. Cho, D. Kumar, P. H. Holloway and R. K. Singh. *Luminescence behavior of pulsed laser deposited Eu:Y_2O_3 thin film phosphors on sapphire substrates.* Applied Physics Letters **73** (21), 3058 (1998).

[Cho99] M. H. Cho, D. H. Ko, K. Jeong, I. W. Lyo, S. W. Whangbo, H. B. Kim, S. Choi, J. H. Song, S. Cho and C. N. Whang. *Temperature dependence of the properties of heteroepitaxial Y_2O_3 films grown on Si by ion assisted evaporation*. Journal of Applied Physics **86** (1), 198 (1999).

[Cho00] M. H. Cho, D. H. Ko, , Y. K. Choi, I. W. Lyo, K. Jeong, C. N. Whang, H. J. Kim and D. Y. Noh. *Thickness dependence of Y_2O_3 films grown on an oxidized Si surface*. Journal of Vacuum Science and Technology (A) **19** (1), 200 (2000).

[Chr94] D. B. Chrisey and G. K. Hubler. *Pulsed laser deposition of thin films* (John Wiley & Sons, Inc., New York, 1994).

[Coh91] A. Cohen, P. Allenspacher, M. M. Brieger and H. O. I. Jeuck. *Beam target interaction during growth of $YBa_2Cu_3O_{7-x}$ by the laser ablation technique*. Applied Physics Letters **59** (17), 2186 (1991).

[Con28] E. U. Condon. *Nuclear motions associated with electron transitions in diatomic molecules*. Physical Review **32**, 858 (1928).

[Con69] B. H. Connor and T. M. Valentine. *A Neutron Diffraction Study of the Crystal Structure of the C-form of Yttrium Sesquioxide*. Acta Crystallographica 2140 (1969).

[Cul78] B. D. Cullity. *Elements of X-ray diffraction, 2^{nd} edition* (Addison Wesley, London, 1978).

[DeC96] M. DeCrescenzi. *Electron scattering and related spectroscopies* (Singapore World Scientific, Singapore, 1996).

[Die68] G. H. Diecke. *Spectra and Energy Levels of Rare Earth Ions in Crystals* (Interscience Publishers, John Wiley & Sons, New York, 1968).

[Dij87] D. Dijkamp, T. Venkatesan, X. D. Wu, S. A. Shaheen, N. Jisrawi, Y. H. Min-Lee, W. L. McLean and M. Croft. *Preparation of Y-Ba-Cu oxide superconductor thin films using pulsed laser evaporation from high T_c bulk material*. Applied Physics Letters **51** (8), 619 (1987).

[Dik03] A. O. Dikovska, P. A. Atanasov, R. I. Tomov, S. H. Tonchev and D. T. Sapundjiev. *Er:Y_2O_3 thin films grown by pulsed laser deposition*. Vacuum **69**, 273 (2003).

[DIN78] DIN 4761, Deutsche Norm. *Oberflächencharakter, Geometrische Oberflächentextur-Merkmale, Begriffe und Kurzzeichen* (Beuth-Verlag, Berlin / Köln, 1978).

[Dup89] H. Dupendant, J. Gavigan, D. Givord, A. Lienard, J. P. Rebouillat and Y. Souche. *Velocity distribution of microsized particles in thin film laser ablation deposition (LAD) of metals and oxide superconductors*. Applied Surface Science **43**, 369 (1989).

[Dye91] R. C. Dye, R. E. Muenchause and N. S. Nogar. *Laser ablation of Y_2O_3*. Chemical Physics Letters **181** (6), 531 (1991).

[Egg19] J. Eggert. *Über den Dissoziationszustand der Fixsterngase*. Physikalische Zeitschrift **20**, 570 (1919).

[Eph26] F. Ephraim and R. Bloch. Chemische Berichte **59**, 2692 (1926).

[Fel86] L. C. Feldman and J. W. Mayer. *Fundamentals of Surface and Thin Film Analysis* (North-Holland, Elsevier Science Publishers B. V., Amsterdam, 1986).

[For99] L. Fornasiero, E. Mix, V. Peters, K. Petermann and G. Huber. *New oxide crystals for solid state lasers*. Crystal Research Technologie **34** (2), 255 (1999).

[For00] L. Fornasiero, E. Mix, V. Peters, K. Petermann and G. Huber. *Czochralski growth and laser parameters of RE^{3+}-doped Y_2O_3 and Sc_2O_3*. Ceramics International **26** (6), 589 (2000).

[Fra59] F. C. Frank and H. J. van der Merwe. *One-dimensional dislocations*. In: *I. u. II. Proc. Royal Soc.*, 205–225 (London, 1959).

[Fri93] D. Fried, T. Kushida, G. P. Reck and E. W. Rothe. *The yttrium oxide chemiluminescence from the 308 nm excimer laser ablation of $YBa_2Cu_3O_{7-X}$, Y_20_3, and YCl_3*. Journal of Applied Physics **73** (11), 7810 (1993).

[Fuk89] H. Fukumoto, T. Imura and Y. Osaka. *Heteroepitaxial growth of Y_2O_3 films on silicon*. Applied Physics Letters **55** (4), 360 (1989).

[Gab02] R. J. Gaboriaud, F. Pailloux and J. Perriere. *Pulsed laser deposition of Y_2O_3 thin films on MgO*. Applied Surface Science **186**, 477 (2002).

[Gao99] H. J. Gao, D. Kumar, K. G. Cho, P. H. Holloway, R. K. Singh, X. D. Fan, Y. Yan and S. J. Pennycook. *Epitaxial growth of Y_2O_3 thin films on $LaAlO_3$*. Applied Physics Letters **75** (15), 2223 (1999).

[Gol68] R. M. Goldstien. *Thin Film Yttrium Oxide Capacitors Formed By Electrochemical Anodization Techniques*. In: *Proceedings of the Electronic Components Conference*, 141–144 (New York, 1968).

[Gos87a] H. J. Gossmann and L. C. Feldman. *Materials Analysis with High Energy Ion Beams Part I: Rutherford Backscattering*. Materials Research Bulletin **12** (6), 26 (1987).

[Gos87b] H. J. Gossmann and L. C. Feldman. *Materials Analysis with High Energy Ion Beams Part II: Channeling and Other Techniques*. Materials Research Bulletin **12** (6), 30 (1987).

[Gru85] J. B. Gruber, C. A. Morrison, R. P. Leavitt and N. C. Chang. *Optical spectra, energy levels, and crystal-field analysis of tripositive rare earth ions in Y_2O_3. IV. C_{3i} sites*. Journal of Chemical Physics **82** (12), 5373 (1985).

[Gur87] M. Gurvitch, L. Manchanda and J. M. Gibson. *Study of thermally oxidized yttrium films on silicon*. Applied Physics Letters **51** (12), 919 (1987).

[Hai01] N. Hairston. *Lithograpgy Aids Integration of Optics*. Laser Focus World **37**, 93 (2001).

[Han93] D. C. Hanna, A. C. Large, D. P. Shephard, A. C. Trooper, I. Charier, B. Ferrand and D. Pelenc. *Low threshold quasi-three-level 946 nm laser operation of an epitaxially grown Nd:$Y_3Al_5O_{12}$ waveguide*. Applied Physics Letters **63** (1), 7 (1993).

[Heb70] J. Heber, K. H. Hellwege, U. Köbler and H. Murmann. *Energy levels and interaction between Eu^{3+}-ions at lattice sites of symmetry C_2 and symmetry C_{3i} in Y_2O_3*. Zeitschrift für Physik **237**, 189 (1970).

[Hen89] B. Henderson and G. F. Imbusch. *Optical Spectroscopy of Inorganic Solids* (Clarendon Press, Oxford, 1989).

[Hir97] G. Hirata, J. Mckittrick, M. Avalos-Borja, J. Siqueiros and D. Devlin. *Physical properties of Y_2O_3:Eu luminescent films grown by MOCVD and laser ablation*. Applied Surface Science **113/114**, 509 (1997).

[Hoe66] H. R. Hoekstra. *Phase Relationships in the Rare Earth Sesquioxides at High Pressure*. Inorganic Chemistry **5** (5), 754 (1966).

[Hoe75] H. Hoefdraad. *The charge transfer absorption band of Eu^{3+} in oxides*. Journal of Solid State Chemistry **15**, 175 (1975).

[Hoe92] T. H. Hoekstra, L. T. H. Hilderink, P. V. Lambeck and T. J. A. Popma. *Photoluminescence and attenuation of spray-pyrolysis-deposited erbium.doped Y_2O_3 planar optical waveguides*. Optics Letters **17** (21), 1506 (1992).

[Hos77] T. Hoshina, S. Imanaga and S. Yokono. *Charge transfer effects on the luminescent properties of Eu^{3+} in oxysulfides*. Journal of Luminescence **15**, 455 (1977).

[Hu96] W. S. Hu and Z. G. Liu. *Pulsed-laser deposition and optical properties of completely (001) textured optical waveguiding $LiNbO_3$ films upon SiO_2/Si substrates*. Optics Letters **21** (13), 946 (1996).

[Hui00] A. Huignard, A. Aron, P. Aschehoug, B. Viana, J. Théry, A. Laurent and J. Perriere. *Growth by laser ablation of Y_2O_3 and Tm:Y_2O_3 thin films for optical applications*. Journal of Materials Chemistry **10**, 549 (2000).

[Iva75] I. A. Ivanova, A. M. Morozov, M. A. Petrova, I. G. Podkolzina and P. P. Feofilov. *Preparation and properties of single crystals of double fluorides of lithium and the rare earths*. Inorganic Materials **11** (12), 1868 (1975).

[Joa95] J. D. Joannopoulos, R. D. Meade and J. N. Winn. *Photonic Crystals – Molding the Flow of Light* (Princeton University Press, New Jersey, 1995).

[Joh87] S. John. *Strong localization of photons in certain disordered dielectric superlattices*. Physical Review Letters **58**, 2486 (1987).

[Jon97] S. L. Jones, D. Kumar, R. K. Singh and P. H. Holloway. *Luminescence of pulsed laser deposited Eu yttrium oxide films*. Applied Physics Letters **71** (3), 404 (1997).

[Jør64] C. Jørgensen, R. Pappalardo and E. Rittershaus. *Reflection Spectra of Lanthanides in Thorium(IV) Oxide and the Large Nephelauxetic Effect of Oxide Ligands or Vacancies*. Zeitschrift für Naturforschung **19A**, 424 (1964).

[Jør70] C. K. Jørgensen. *Electron Transfer Spectra*. Progress in Inorganic Chemistry **12**, 101 (1970).

[Jud62] B. R. Judd. *Optical Absorption Intensities of Rare-Earth Ions*. Physical Review **127** (3), 750 (1962).

[Kai02] N. Kaiser. *Review of the fundamentals of thin-film growth*. Applied Optics **41** (16), 3053 (2002).

[Kam89] S. Kampf. *Bildung und Zerfall der heteronuklearen Edelgasexzimere KrAr, KrNe, XeKr und XeAr*. Dissertation, Fachbereich Physik, Universität Hamburg (1989).

[Kam90] A. A. Kaminskii. *Laser Crystals - Their Physics and Properties, 2^{nd} edition* (Springer Verlag, New York, 1990).

[Kay88] Y. Kayanuma. *Quantum-size effects of interacting electrons and holes in semiconductor microcrystals with spherical shape*. Physical Review B **38** (14) (1988).

[Kel92] R. Kelly. *Gas dynamics of the pulsed emission of a perfect gas with applications to laser sputtering and to nozzle expansion*. Physical Review A **42** (2) (1992).

[Kim03] T. Kim Anh, L. Quoc Minh, N. Vu, T. Thu Huong, N. Thanh Huong, C. Barthou and W. Strek. *Nanomaterials containing rare-earth ions Tb, Eu, Er and Yb: preparation, optical properties and application potential*. Journal of Luminescence **102-103**, 391 (2003).

[Kir03] M. Kirm. *unveröffentlichte Messungen* (Fachbereich Physik, Universität Hamburg, 2003).

[Klo89] T. Kloiber. *Erosion fester Edelgase durch photonenstimulierte Desorption neutraler Edelgasatome und -moleküle*. Dissertation, Fachbereich Physik, Universität Hamburg (1989).

[Kni98] T. C. Knight, T. A. Birks, P. S. J. Russell and J. P. de Sandro. *Properties of photonic crystal fiber and the effective index model*. Journal of the Optical Society of America A (Optics, Image Science and Vision) **15** (3), 748 (1998).

[Kon01] A. Konrad, U. Herr, R. Tidecks, F. Kummer and K. Samwer. *Luminescence of bulk and nanocrystalline cubic yttria*. Journal of Applied Physics **90** (7), 3516 (2001).

[Kor89] G. Koren, A. Gupta, R. J. Basemann, M. I. Lutwyche and R. Laibowitz. *Laser wavelength dependent properties of $YBa_2Cu_3O_{7-\delta}$ thin films deposited by laser ablation*. Applied Physics Letters **55** (23), 2450 (1989).

[Kor99] F. Korte, S. Nolte, B. N. Chichkov, T. Bauer, G. Kamlage, T. Wagner, C. Fallnich and H. Welling. *Far-field and near-field material processing with femtosecond laser pulses*. Applied Physics A (1999).

[Kor00] M. B. Korzenski, P. Lecoeur, B. Mercey, D. Chippaux, B. Raveau and R. Desfeux. *PLD-Grown Y_2O_3 Thin Films from Y Metal: An Advantageous Alternative to Films Deposited from Yttria*. Chemistry of Materials **12**, 3139 (2000).

[Kor01] M. B. Korzenski, P. Lecoeur, B. Mercey, P. Camy and J. L. Doualan. *Low propagation losses of an Er:Y_2O_3 planar waveguide grown by alternate-target pulsed laser deposition*. Applied Physics Letters **78** (9), 1210 (2001).

[Kos98] H. Kosaka, T. Kawashima, A. Tomita, M. Notomi, T. T. T. Sato and S. Kawakami. *Superprism phenomena in photonic crystals*. Physical Review B **58** (16), R10096 (1998).

[Kra03] T. F. Krauss. *Planar photonic crystal waveguide devices for integrated optics*. Physica Status Solidi (a) **197** (3), 688 (2003).

[Kum98] C. Kumpf. *Die strukturellen und epitaktischen Eigenschaften von Platin- und Iridiumsilizid Schichtsystemen, charakterisiert mit oberflächensensitiven Röntgenstreumethoden*. Dissertation, Mathematisch-Naturwissenschaftliche Fakultät, Universität Rostock (1998).

[Kuz03] Y. Kuzminkh. *not published* (Fachbereich Physik, Universität Hamburg, 2003).

[Lec02] P. Lecoeur, M. B. Korzenski, A. Ambrosini, B. Mercey, P. Camy and J. L. Doualan. *Growth of Er:Y_2O_3 thin films by pulsed laser ablation from metallic targets*. Applied Surface Science **186**, 403 (2002).

[Lee86] D. H. Lee. *Electromagnetic principles of integrated optics* (Chapman and Hall, 1986).

[Lif03] G. Lifantes. *Integrated Photonics: Fundamentals* (Wiley CVH Verlag GmbH, Weinheim, Germany, 2003).

[Liu82] J. M. Liu. *Simple technique for measurement of pulsed Gaussian-beam spot sizes*. Optics Letters **7**, 196 (1982).

[Lou01] L. Lou, W. Zhang, A. Brioude, C. Le Luyer and J. Mugnier. *Preparation and characterization of sol-gel Y_2O_3 planar waveguides*. Optical Materials **18**, 331 (2001).

[Luo02] B. Luo, J. W. J. aand R. M. Mehandru, F. Ren, B. P. Gila, A. H. Onstine, C. R. Abernathy, S. J. Pearton, A. G. Baca, R. D. Briggs, R. J. Shul, C. Monier and J. Han. *Influence of MgO and Sc_2O_3 passivation on AlGaN/GaN high-electron-mobility transistors*. Applied Physics Letters **80** (9), 1661 (2002).

[Mai83] L. I. Maissel and R. Glang. *Handbook of Thin Film Technology* (McGraw-Hill, New York, 1983).

[Man63] M. Mandel. *Paramagnetic resonance of Yb^{3+} in yttrium oxide*. Applied Physics Letters **2** (10), 197 (1963).

[Mar03] P. Markos and C. M. Soukoulis. *Structures with negative index of refraction*. Physica Status Solidi (a) **197** (3), 595 (2003).

[McK00] J. McKittrick, C. F. Bacalski and G. A. Hirata. *Characterization of Photoluminescent ($(Y_{1-x}Eu_x)_2O_3$) Thin Films Prepared by Metallorganic Chemical Vapor Deposition*. Journal of the American Ceramic Society **83** (5), 1241 (2000).

[McN97] A. D. McNaught and A. Wilkinson. *Compendium of Chemical Terminology*. In: International Union of Pure and Applied Chemistry (IUPAC) (editor), *http://www.iupac.org* (Blackwell Science, London, 1997).

[Met94] S. M. Metev and V. P. Veiko. *Laser-Assisted Microtechnology* (Springer-Verlag, Berlin, Heidelberg, 1994).

[Mio95] A. Miotello and R. Kelly. *Critical assessment of thermal models for laser sputtering at high fluences*. Applied Physics Letters **67** (24), 3535 (1995).

[Mix99] E. Mix. *Kristallzüchtung, Spektroskopie und Lasereigenschaften Yb-dotierter Sesquioxide*. Dissertation, Institut für Laser-Physik, Universität Hamburg (1999).

[Möl86] T. Möller, P. Gürtler and E. R. und G. Zimmerer. *The experimental station superlumi: A unique setup for time- and spectrally resolved luminescence under state selective excitation with synchrotron radiation*. Nuclear Instruments and Methods A **246**, 461 (1986).

[Moi97] B. Moine, C. Dujardin, H. Lautesse, C. Pedrini, C. Combes, A. Belski, P. Martin and J. Gesland. *Spectroscopic and scintillation properties of cerium-doped LuF_3 single crystal*. Materials Forum **239-241**, 245 (1997).

[Mor82] C. A. Morrison and R. P. Leavitt. *Spectroscopic properties of triply ionized lanthanides in transparent host crystals*. In: K. A. G. Jr and L. Eyring (editors), *Handbook on the physics and chemistry of rare earths*, volume 5, chapter 46, 461–692 (North-Holland, Amsterdam, 1982).

[Nak79] E. Nakazawa. *Charge transfer type Luminescence of Yb^{3+} ions in RPO_4 and R_2O_2S (R=Y, La, and Lu)*. Journal of Luminescence **18/19**, 272 (1979).

[Nod00] S. Noda, A. Chutinan and M. Imada. *Trapping and emission of photons by a single defect in a photonic bandgap structure*. Nature **407**, 608 (2000).

[Nol94] W. Nolting. *Statistische Physik*. In: *Grundkurs: Theoretische Physik*, volume 6 (Verlag Zimmermann-Neufang, Ulmen, 1994).

[Ofe62] G. S. Ofelt. *Intensities of Crystal Spectra of Rare-Earth Ions*. Journal of Chemical Physics **37** (3), 511 (1962).

[Ohm02] S. Ohmi, M. Takeda, H. Ishiwara and H. Iwai. *Characterization of Lu_2O_3 high-k thin films on Si(100)fabricated by e-beam deposition method*. In: *Proceedings of the Conference of the Institute of Scientific & Technical Communicators (ISTC)*, 251–261 (Peterborough, UK, 2002).

[Pal85] E. D. Palik. *Handbook of Optical Constants of Solids* (Academic Press, New York, 1985).

[Pea75] R. D. Peacock. *The Intensities of Lanthanide f↔f Transitions,* Bd. 22 (Springer-Verlag, Berlin, Heidelberg, New York, 1975).

[Pet81] K. Petermann. *Elektrische und optische Eigenschaften von epitaktischen ZnS-$CuGaS_2$-Hetrodioden*. Dissertation, Technische Universität Berlin (1981).

[Pet01] V. Peters. *Growth and Spectroscopy of Ytterbium-Doped Sesquioxides*. Dissertation, Institut für Laser-Physik, Universität Hamburg (2001).

[Pie01] L. Pieterson. *Charge transfer and $4f^n \leftrightarrow 4f^{n-1}5d$ luminescence of lanthanide ions*. Proefschrift, Faculteit Scheikunde, Universiteit Utrecht (2001).

[Pol97] A. Polman. *Erbium implanted thin film photonic materials*. Journal of Applied Physics **82** (1), 1 (1997).

[Pon02] O. Pons-Y-Moll, J. Perriere, E. Millon, R. M. Defourneau and D. Defourneau. *Structural and optical properties of rare-earth-doped Y_2O_3 waveguides grown by pulsed-laser deposition*. Journal of Applied Physics **92** (9), 4885 (2002).

[Pur46] E. Purcell, H. Torrey and R. Pound. *Resonance absorption by nuclear magnetic moments in a solid*. Physical Review **69**, 37 (1946).

[Qi02] Z. Qi, C. Shi, W. Zhang, W. Zhang and T. Hu. *Local structure and luminescence of nanocrystalline Y_2O_3:Eu*. Applied Physics Letters **81** (15), 2857 (2002).

[Rab03] M. Rabisch. *not published* (Fachbereich Physik, Universität Hamburg, 2003).

[Rao96] R. P. Rao. *Growth and characterization of Y_2O_3:Eu^{3+} phosphor films by sol-gel process*. Solid State Communications **99** (6), 439 (1996).

[Ras92] A. C. Rastogi and R. N. Sharma. *Structural and electrical characteristics of metal-insulator-semiconductor diodes based on Y_2O_3 dielectric thin films on silicon*. Journal of Applied Physics **71** (10), 5041 (1992).

[Ray63] D. K. Ray. *Investigations into the Origin of the Crystalline Electric Field Effects on Rare Earth Ions - II. Contributions from the Rare Earth Orbitals*. Proceedings of the Physical Society **82**, 47 (1963).

[Rea63] J. F. Ready. *Development of plume of material vaporized by giant-pulse laser*. Applied Physics Letters **3** (4), 11 (1963).

[Rot60] R. S. Roth and S. J. Schneider. *Phase Equilibria in Systems Involving the Rare-Earth Oxides. Part I. Polymorphism of the Oxides of the Trivalent Rare-Earth Ions*. Journal of Research of the National Bureau of Standards-A **64** (4), 309 (1960).

[Rus03] P. Russell. *Photonic crystal fibers*. Science **299** (5605), 358 (2003).

[Sae89] K. L. Saenger. *Time-resolved optical emission during laser ablation of Cu, CuO, and high-T_c superconductors: $Bi_{1.7}Sr_{1.3}Ca_2Cu_3O_x$ and $Y_1Ba_{1.7}Cu_{2.7}O_y$*. Journal of Apllied Physics **66** (9), 4435 (1989).

[Sae93a] K. Saenger. *Pulsed laser depostion (Part I) - A review of process characteristics and capabilities*. Processing of Advanced Materials **3**, 1 (1993).

[Sae93b] K. Saenger. *Pulsed laser depostion (Part II) - A review of process mechanisms*. Processing of Advanced Materials **3**, 63 (1993).

[Sah21] M. N. Saha. *Versuch einer Theorie der physikalischen Erscheinungen bei hohen Temperaturen mit Anwendungen auf die Astrophysik*. Zeitschrift für Physik **6**, 40 (1921).

[Sak01] K. Sakoda. *Optical Properties of Photonic Crystals* (Springer-Verlag, Berlin, Heidelberg, New York, 2001).

[Sam82] G. V. Samsonov. *The Oxide Handbook* (IFI / Plenum Press, New York, 1982).

[San85] H. Sankur and R. Hall. *Thin-film deposition by laser-assisted evaporation*. Applied Optics **24** (20), 3343 (1985).

[Sch98] H. L. Schläfer and G. Gliemann. *Einführung in die Ligandenfeldtheorie* (Akademische Verlagsgesellschaft, Frankfurt am Main, Germany, 1998).

[Seo02] S. Y. Seo, S. Lee, H. D. Park, N. Shin and K. S. Sohn. *Luminescence of pulsed laser deposited Gd_2O_3:Eu^{3+} thin film phosphors on quartz glass substrates*. Journal of Applied Physics **92** (9), 5248 (2002).

[Ser99] R. Serna, M. Jiménez de Castro, J. A. Chaos and C. N. Afonso. *The role of Er^{3+}-Er^{3+} separation on the luminescence of Er-doped Al_2O_3 films by pulsed laser deposition*. Applied Physics Letters **75** (26), 4073 (1999).

[Sha93] R. N. Sharma and A. C. Rastogi. *Compositional and electronic properties of chemical-vapor-deposited Y_2O_3 thin film-Si(1O0) interfaces*. Journal of Applied Physics **74** (14), 6691 (1993).

[Sie86] A. E. Siegman. *Lasers* (University Science Books, Mill Valley, California, 1986).

[Sin66] S. P. Sinha. *Complexes of the rare earths* (Pergamon Press, London, 1966).

[Sin90] R. K. Singh and J. Narayan. *Pulsed-laser evaporation technique for deposition of thin films: Physics and theoretical model*. Physical Review B **41** (13), 8843 (1990).

[Sin92] R. K. Singh, D. Bhattacharya, P. Tiwari, J. Narayan and C. B. Lee. *Improvement in the properties of high T_c films fabricated in situ by laser ablation of $YBa_2Cu_3O_7$-Ag targets*. Applied Physics Letters **60** (2), 2022 (1992).

[Ska92] G. Skandan, C. M. Foster, H. Frase, M. N. Ali, J. C. Parker and H. Hahn. *Phase characterization and stabilization due to grain size effects of nanostructured Y_2O_3*. Nanostructured Materials **1** (4), 313 (1992).

[Smi65] H. M. Smith and A. F. Turner. *Vacuum Deposited Thin Films Using a Ruby Laser*. Applied Optics **4** (1), 147 (1965).

[Stu96] B. C. Stuart, M. D. Feit, S. Herman, A. M. Rubenchik, B. W. Shore and M. D. Perry. *Nanosecond-to-femtosecond laser-induced breakdown in dielectrics*. Physical Review B **53** (4), 1749 (1996).

[Sun96] X. W. Sun, H. C. Huang, and H. S. Kwoka. *On the initial growth of indium tin oxide on glass*. Applied Physics Letters **68** (19), 2663 (1996).

[Sun99] C. Q. Sun. *The lattice contraction of nanometre-sized Sn and Bi particles produced by an electrohydrodynamic technique*. Journal of PhysicsC: Condensed Matter **11** (24), 4801 (1999).

[Sun01] C. Q. Sun, B. K. Tay, S. P. Lau, , X. W. Sun, X. T. Zeng, S. Li, H. L. Bai, H. Liu, Z. H. Liu, and E. Y. Jiang. *Bond contraction and lone pair interaction at nitride surfaces*. Journal of Applied Physics **90** (5), 2615 (2001).

[Tan98] Z. K. Tang, G. K. L. Wong, P. Yu, M. Kawasaki, A. Ohtomo, H. Koinuma and Y. Segawa. *Room-temperature ultraviolet laser emission from self-assembled ZnO microcrystallite thin films*. Applied Physics Letters **72** (25), 3270 (1998).

[Thu99] A. Thum-Jäger and K. Rohr. *Angular emission distributions of neutrals and ions in laser ablated particle beams*. Journal of Physics D: Applied Physics **32**, 2827 (1999).

[Tis99] D. V. Tishinin, P. D. Dapkus, A. E. Bond, I. Kim, C. K. Lin and J. O'Brien. *Vertical Resonant Couplers with Precise Coupling Efficiency Control Fabricated by Wafer Bonding*. IEEE Photonics Technology Letters **11** (8), 1003 (1999).

[Tom86] T. Tomiki, J. Tamashiro, Y. Tanahara, A. Yamada, H. Fukutani, T. Miyahara, H. Kato, S. Shin and M. Ishigame. *Optical Spectra of Y_2O_3 Single Crystals in VUV*. Journal of the Physical Society of Japan **55** (12), 4543 (1986).

[Top01] T. Topuria, P. Möck, N. D. Browning, L. V. Titova, M. Dobrowolska, S. Lee and J. K. Furdyna. *Z-contrast scanning transmission electron microscopy on self-assembled CdSe quantum dots in ZnSe and (Zn,Mn)Se matrices*. In: *Material Research Society Symposium Proceedings*, volume 642, J8.3.1–J8.3.6 (Material Research Society, 2001).

[Ugl77] A. A. Uglov and A. N. Kokora. *Thermophysical and hydrodynamic effects in laser-beam processing of materials*. Soviet Journal of Quantum Electronics **7**, 671 (1977).

[Vah03] K. J. Vahala. *Optical microcavities*. Nature **424**, 839 (2003).

[Van86] M. A. Van Hove, W. H. Weinberg and C. M. Chan. *Low energy electron diffraction : experiment, theory and surface structure determination* (Springer Verlag, Berlin, 1986).

[Var94] D. Varding. *Luminiszenzspektroskopische Untersuchung dynamischer Eigenschaften freier Exzitonen in festen Edelgasen Krypton und Xenon*. Dissertation, Fachbereich Physik, Universität Hamburg (1994).

[Veg21] L. Vegard. *Die Konstitution der Mischkristalle und die Raumfüllung der Atome*. Zeitschrift für Physik **5** (27), 17 (1921).

[Ven00] J. A. Venables. *Introduction to surfaced and thin film processes* (Cambridge University Press, Cambridge, 2000).

[Vin00] L. T. Vinh, V. Yam, Y. Zeng and D. Bouchier. *Nucleation and growth of self-assembled Ge/Si(001) quantum dots in single and stacked layers*. Thin Solid Films **380**, 2 (2000).

[Web82] M. J. Weber. *Lasers and Masers*. In: *CRC Handbook of Laser Science and Technology*, volume 1 (CRC Press Inc., Boca Raton, Florida, 1982).

[Wit03] R. Withnall, M. I. Martinez-Rubio, G. R. Fern, T. G. Ireland and J. Silver. *Photonic phophors based on cubic Y_2O_3: Tb^{3+} infilled into a synthetic opal lattice*. Journal of Optics A **5**, S81 (2003).

[Wyc86] R. W. G. Wyckoff. *Crystal Structures Vol.2, 2^{nd} edition* (Interscience Publishers, New York, 1986).

[Xu91] Y. Xu and W. C. Ching. *Self-consistent band structures, charge distributions, and optical-absorption spectra in MgO, Al2O3 and $MgAl_2O_4$*. Physical Review B **43**, 4461 (1991).

[Xu97] Y. Xu, Z. Gu and W. Y. Ching. *Electronic, structural, and optical properties of crystalline yttria*. Physical Review B **56** (23), 14993 (1997).

[Yab87] E. Yablonovitch. *Inhibited Spontaneous Emission in Solid-State Physics and Electronics*. Physical Review Letters **58** (20), 2059 (1987).

[Yar89] A. Yariv. *Quantum electronics* (John Wiley&Sons, New York, 1989).

[Zha98] S. Zhang and R. Xiao. *Yttrium oxide films prepared by pulsed laser deposition*. Journal of Applied Physics **83** (7), 3842 (1998).

[Zhe89] J. P. Zheng, Z. Q. Huang, D. T. Shaw and H. S. Kwok. *Generation of high-energy atomic beams in laser-superconducting traget interactions*. Applied Physics Letters **54** (3), 280 (1989).

[Zyc02] E. Zych. *Concentration dependence of energy transfer between Eu^{3+} ions occupying two symmetry sites in Lu_2O_3*. Journal of Physics: Condensed Matter **14**, 5637 (2002).

List of Publications

Publications in Journals

1. E. Heumann, S. Bär, H. Kretschmann, and G. Huber. *Diode pumped continuous wave green upconversion lasing of Er^{3+}:$LiLuF_4$ using multi pass pumping.* Optics Letters **27** (19), 1699 (2002).

2. S. Bär, G. Huber, J. Gonzalo, A. Perea, A. Climent and F. Paszti. *Europium-doped sesquioxide thin films grown on sapphire by PLD.* Materials Science and Engineering B **105** (1-3), 29 (2003).

International Conference Contributions

1. G. Huber, S. Bär, E. Heumann, S. Kück, H. Scheife. *Crystals for up-conversion lasers.* 2nd International Symposium on Laser, Scintillator and Nonlinear Optical Materials (Lyon, France, May 28 - 31, 2000), invited talk.

2. S. Bär, H. Scheife, E. Heumann, G. Huber. *Room-temperature continuous-wave Er^{3+}:$LiLuF_4$ upconversion laser at 552 nm.* Conference on Lasers and Electro-Optics / Europe (CLEO/Europe - IQEC) (Nice, France, September 10 - 15, 2000), talk CTuF3.

3. H. Scheife, S. Bär, P. Rogin, K. Petermann, G. Huber. *Preparation and lasing of a novel crystalline T-waveguide structure.* Conference on Lasers and Electro-Optics Europe (CLEO/Europe - IQEC) (Nice, France, September 10 - 15, 2000), talk CTuM7.

4. E. Heumann, S. Bär, H. Scheife, G. Huber. *Green upconversion lasing of Er^{3+}:$LiLuF_4$ using cavity external pump feedback.* Conference on Advanced Solid-State Lasers (Quebec, Canada, 2002), technical digest pp.

5. E. Heumann, S. Bär, H. Kretschmann, G. Huber, *Diode pumped cw green upconversion lasing of Er^{3+}:$LiLuF_4$ at room temperature under multi pass pumping*, Conference on Lasers and Electro-Optics (Long Beach, USA, 2002), technical digest CPDC7 (post deadline session).

6. E. Heumann, S. Bär, G. Huber. *Diode pumped continuous wave green upconversion laser at room temperature.* XIth Conference on Laser Optics (St. Petersburg, Russia, 2003).

7. S. Bär, G. Huber, J. Gonzalo, A. Perea, A. Climent, F. Paszti. *Rare-earth-doped sesquioxide thin films grown on sapphire by PLD.* Conference of the European Materials Research Society E-MRS (Strasbourg, France, 2003), poster presentation.

National Conference Contributions

1. S. Bär, H. Scheife. *Präparation und Laserbetrieb eines kristallinen T-Wellenleiters.* 12. Norddeutscher Lasertag (Hamburg, 2001), poster presentation.

2. S. Bär, E. Heumann, G. Huber. *Green upconversion lasing of Er^{3+}:$LiLuF_4$ using extra cavity pump feedback.* Verhandlungen der DPG, Frühjahrstagung FG Quantenoptik (Osnabrück 2002), oral presentation Q121.8.

3. L. Rabisch, P. Burmester, T. Ishii, S. Bär, Günter Huber. *Optical properties of Eu doped yttria thin films.* Verhandlungen der DPG, Frühjahrstagung FG Festkörper (Dresden, 2003), oral presentation DS23.8.

4. S. Bär, G. Huber, J. Gonzalo, A. Perea, A. Climent, F. Paszti, M. Munz. *Preparation and characterization of thin sesquioxide films grown on α-Al_2O_3 by PLD.* 14. Norddeutscher Lasertag (Braunschweig, 2003), poster presentation.

Meetings, Seminars, Summer Schools

1. Anwendungsorientiertes Woollam-Ellipsometrie-Seminar (Darmstadt, Germany, October 24-25, 2001).

2. 3rd International Wilhelm and Else Heraeus Summer School. *Photonic Crystals: Optical Materials for the 21st Century.* (Wittenberg, Germany, July 15-25, 2001).

3. S. Bär. *Green upconversion lasing of Er^{3+}:$LiLuF_4$: From Crystal Growth to Laser Experiments.* Seminar at the Instituto de Optica, CSIC (Madrid, Spain, 2003).

4. S. Bär. *Selten-Erd-dotierte Sesquioxidschichten auf Saphir.* GrK Seminar über Festkörperlaser, Institut für Laser-Physik (Hamburg, Germany, 2003).

5. S. Bär. *Upconversion-Laser und Selten-Erd-dotierte Sesquioxidschichten.* Seminar, Bundesanstalt für Materialforschung und -prüfung (Berlin, Germany, 2003).

6. S. Bär. *Characterization of thin sesquioxide films on α-Al_2O_3 fabricated by PLD.* Seminar, École Polytechnique Fédérale de Lausanne (Lausanne, Switzerland, 2003).

Acknowledgement

The work of the last three years in the "Solid-State Laser" group at the Institute of Laser-Physics would not have been possible without the support of many people.

First, I would like to thank my supervisor, Prof. Dr. Günter Huber, for the opportunity to carry out my PhD studies in his group and for the interesting work in a 'new' field of research.

I have to thank the entire group 'F' for the terrific working atmosphere, especially, the "Thin Film" team of the ILP Dr. Klaus Petermann, Dr. Hanno Scheife, Dr. Philipp Burmester, Lutz Rabisch, Yury Kuzminykh, and 'my' diploma student Stefan Ehlert (who supported me at my last experiments) for solving experimental problems and for the discussions on 'strange' spectra. Dr. Klaus Petermann, Dr. Hanno Scheife, and Dr. Stefan Kück I have to thank for proof-reading this thesis.

Thanks a lot to my former and actual office fellows Dr. Markus Henke, Dr. Christoph Czeranowski, Katja Rademaker, Lutz Rabisch, Karsten Scholle, and André Richter for the very good working atmosphere and having a lot of fun. There are not many problems related to LaTeX, but whenever one of them crossed my way Kai Lünstedt knows the answer ... Thanks! For the technical and logistical support I have to thank Günter Roschewski, Robert Fischer, Stefan Garbers, Friedjof Tellkamp, and Silke Frömmig.

Se lo agradezco muchísimo a los todos de Instituto de Óptica, Consejo Superior de Investigaciones Científicas (CSIC), Madrid (Spain). Especially, Javier Solís, who gave me the chance to work on PLD at the institute, my tutor José 'Pepe' Gonzalo, who tried to make the impossible possible, Ángel Perea for the XRD measurements, and the 'southern italian woman' Eva Mero for her help with the organizational stuff. Thanks to the rest of the group, Carmen, Rosalía, Emmanuel, Miguel, Jan, Oscar, Raúl, Amelia, Anna, and Marc. A big thanks goes to Dr. Jörn Bonse for uncounted, but fruitful discussions on the interaction of short-pulse lasers with different materials and the correct interpretation of AFM pictures, either at "Mamma Mia" or at "Burger King". Moreover, I have to thank Jörn not only for proof-reading this thesis but also for his GB-library of papers.

I also would like to thank

- ... Dr. Reiche of the Institute of Crystal Growth for tempering the first Y_2O_3 targets, which have been required urgently for the work in Madrid.
- ... Aurelio Climent Font and Ferenc Pászti from the Centro de Micro-Análisis de Materiales, Madrid (Spain),for the RBS measurements.
- ... Rainer Behn for additional XRD-measurements at the TU Hamburg-Harburg.

Acknowledgement

... Arne Bolz and Dr. Christian Kumpf for the SXRD measurements and their help in interpreting the data.
... Dr. Marco Kirm and Sebastian Vielhauer for the experiments at SuperLumi.
... Dr. Martin Munz of the BAM in Berlin for AFM measurements.
... Dieter Barlösius of the ILP for the preparation of the EBV-waveguides.
... Dr. Aurelian Crunteanu, Dr. Vasilis Apostolopoulos and Dr. Markus Pollnau from the EPF de Lausanne for the waveguide simulations and the waveguide experiments.
... Markus Schmidt for the photonic band gap simulations.
... Jennifer Grünewald for proof-reading this thesis.

Last but not least, I would like to thank my friends and my family, and especially Kerstin for all their support and help during the last years, which made many things much easier!

This work was funded by the Deutsche Forschungsgemeinschaft through the Graduiertenkolleg "Atome und lokalisierte Felder – Felder und lokalisierte Atome" no. 463. Additionally, this research has also been supported by a Marie Curie Fellowship (HPMT-GH-00-00064-06) of the European Community Programme (HPMT-CT-00-00064).

Index

alumina (α-form), 12
annealing, 86
atomic force microscopy (AFM), 69
avalanche ionization, 26

Bloch states, 102
Born-Oppenheimer approximation, 20
Bragg-diffraction-law, 50
bremsstrahlung, 32
    inverse, 32

central field approximation, 15
channeling (RBS), 66
charge transfer, 18
configurational coordinate model, 20
corundum, 12
crater formation, 30

defect modes, 101

Eggert–Saha-equation, 31
electron-phonon-coupling, 20
Erbium
    energy level scheme, 90
    IR fluorescence, 90
Europium, 22
    energy level scheme, 22
    fluorescence, 23
Ewald sphere, 51
excitation
    Eu:Lu_2O_3, 88
    Eu:Y_2O_3, 79
excitation, VUV
    Eu:Lu_2O_3, 89
    Eu:Y_2O_3, 80
    experimental setup (SuperLumi), 76

fluorescence
    Er:Sc_2O_3, 90
    Eu:Lu_2O_3, 88, 89
    Eu:Y_2O_3, 77, 79, 80
    experimental setup (Fluorolog), 75
Fluorolog, 75
fracto-emission, 30
Franck-Condon principle, 21
Frank-van-der-Merwe growth, 37
free-carrier absorption, 26

growth mechanisms
    island growth, 36
      of yttria (Y_2O_3) (AFM), 72
    layer-by-layer growth, 36
    layer-plus-island growth, 36
growth rate, 43

heteroepitaxy, 38
homoepitaxy, 38

interface effects, 82
inverse bremsstrahlung, 32
island growth, 37
    of yttria (Y_2O_3) (AFM), 72

Kramers degeneration, 16

lanthanide contraction, 14
Laporte selection rules, 17
laser fluence, 27
    threshold, 29
      experimental determination, 45
      of yttria (Y_2O_3), 47
laser-induced breakdown, 26
lattice mismatch, 38
    RE_2O_3−alumina, 39
lattice vector, reciprocal, 51, 59
layer-by-layer growth, 37
layer-plus-island growth, 37
ligand-field theory, 18

lutetiumoxide Lu_2O_3, 11

Mach number, 34
Maxwell equations, 94
Miller indices, 50
mode guidance condition equation, 95
multi-phonon relaxation, 21
multi-photon absorption, 26

nephelauxetic effect, 11, 14
numerical aperture (NA), 93

optical electronegativity, 19
optical penetration depth, 28

particulates, 30
photonic bandgap, 101
photonic crystal, 101
    Y_2O_3 waveguide, 103
plasma, 31
    angular distribution, 35
    expansion, 32
    in background gas, 33
polarization
    transverse electric (TE), 94
    transverse magnetic (TM), 94
propagation constant, 93
pulsed laser deposition (PLD), 25
    experimental setup, 42

quantum confinement, 84

rare-earth-ions, 14
reflectometry, 43
rocking curves, 52
roughness, RMS, 69
Russel-Saunders-coupling, 16
Rutherford backscattering (RBS), 65
    channeling, 66

sapphire, 12
scandiumoxide Sc_2O_3, 11
Scherrer equation, 51
selection rules, 17
    Laporte selection rules, 17
Sellmeier equations
    alumina, 96
    sesquioxides, 96
sesquioxides, 9
    lutetiumoxide Lu_2O_3, 11
    scandiumoxide Sc_2O_3, 11
    yttriumoxide Y_2O_3, 10
splashing-effect, 30
Stark splitting, 16
stoichiometry
    conservation of, 30
    experimental determination (RBS), 65
    of yttria (Y_2O_3) films, 68
Stokes shift, 21
Stranski-Krastanov growth, 37
stress
    compressive, 38
    tensile, 38
    thermal, 56
structure factor, 50
subplantation, 84
substrate heating, 44
substrates, 42
superheating, 29
SuperLumi, 76
surface coordinates, 58
surface effects, 83
surface morphology
    $YScO_3$, 73
    scandia, 73
    substrate, 70
    yttria, 70–72
surface X-ray diffraction (SXRD), 58
    surface coordinates, 58
symmetry
    centrosymmetric C_{3i}, 9
    non-centrosymmetric C_2, 9

target morphology, 29
target outgassing, 30
target preparation, 41
target–substrate distance, 41
texture, 50
thermal diffusion length, 27
thermal diffusivity, 27
Thomson scattering, 50
total internal reflection, 93

critical angle, 93
transitions
charge transfer, 18
interconfigural 4f-5d, 18
intraconfigural 4f-4f, 17
non-radiative, 21

Vegard's law, 39
Volmer-Weber growth, 37

waveguide, 93
asymmetric slab waveguide, 95
experiments, 97
preparation, 96
ridge waveguide, 99
simulation, 99

X-ray diffraction (XRD), 49
diffraction peaks of Y_2O_3, 115
setup, Bragg-Brentano, 52
surface X-ray diffraction, 58

Young's equation, 37
yttriumoxide Y_2O_3, 10